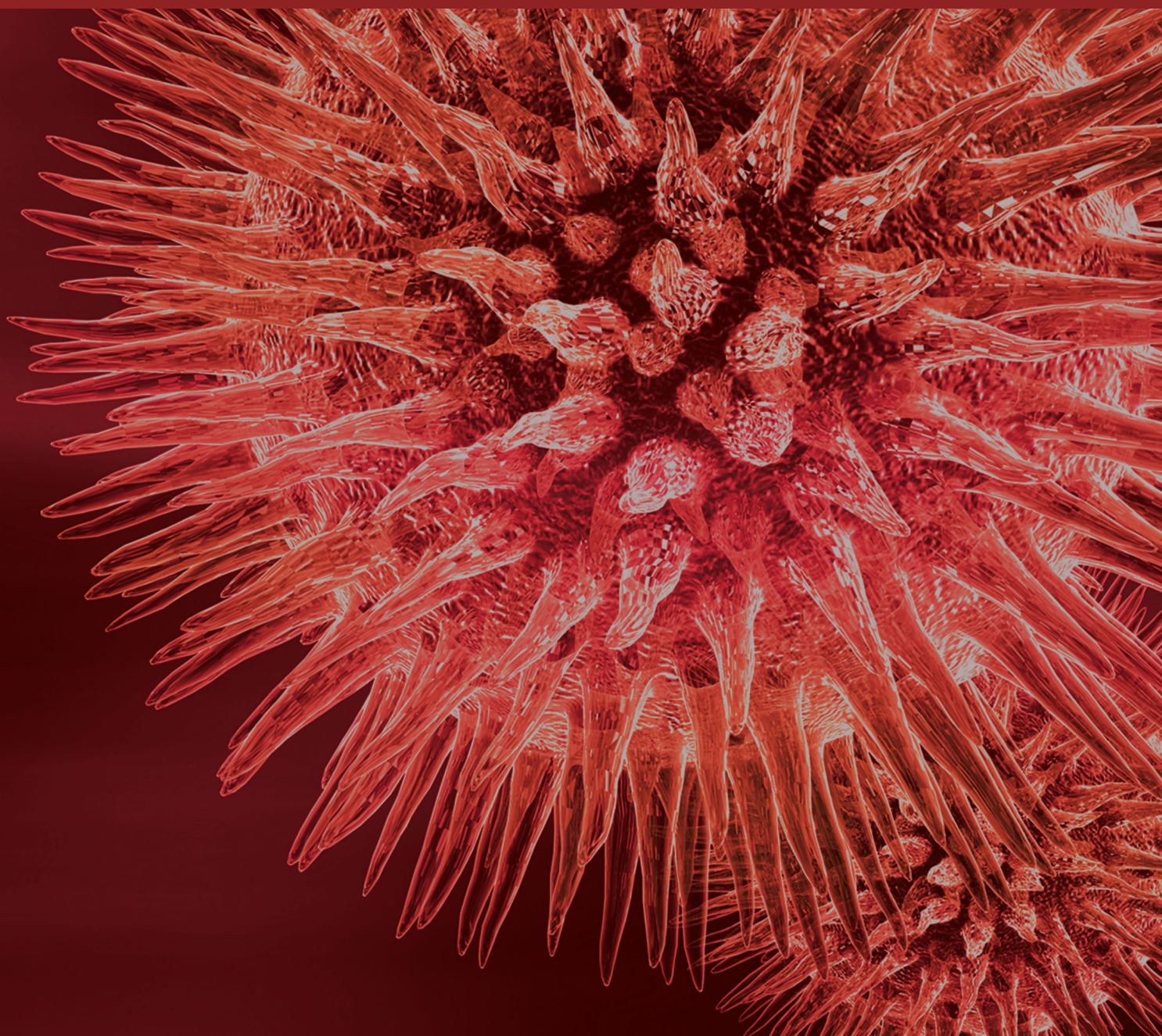


BioMed Research International

Bioengineering Materials in Dental Application

Lead Guest Editor: Wei J. Chang

Guest Editors: Abe Sinichi, Sinji Kamakura, Ren-Yeong Huang,
and Jung-Wei Chen





Bioengineering Materials in Dental Application

BioMed Research International

Bioengineering Materials in Dental Application

Lead Guest Editor: Wei J. Chang

Guest Editors: Abe Sinichi, Sinji Kamakura, Ren-Yeong Huang,
and Jung-Wei Chen



Copyright © 2017 Hindawi. All rights reserved.

This is a special issue published in “BioMed Research International.” All articles are open access articles distributed under the Creative Commons Attribution License, which permits unrestricted use, distribution, and reproduction in any medium, provided the original work is properly cited.

Contents

Bioengineering Materials in Dental Application

Wei-Jen Chang, Abe Shinichi, Shinji Kamakura, Ren-Yeong Huang, and Jung-Wei Chen
Volume 2017, Article ID 2135036, 2 pages

In Vitro Laser Treatment Platform Construction with Dental Implant Thread Surface on Bacterial Adhesion for Peri-Implantitis

Hsien-Nan Kuo, Hsiang-I Mei, Tung-Kuan Liu, Tse-Ying Liu, Lun-Jou Lo, and Chun-Li Lin
Volume 2017, Article ID 4732302, 7 pages

Influence of Deformation and Stress between Bone and Implant from Various Bite Forces by Numerical Simulation Analysis

Hsin-Chung Cheng, Boe-Yu Peng, May-Show Chen, Chiung-Fang Huang, Yi Lin, and Yung-Kang Shen
Volume 2017, Article ID 2827953, 7 pages

Surface Treatment on Physical Properties and Biocompatibility of Orthodontic Power Chains

H. C. Cheng, M. S. Chen, B. Y. Peng, W. T. Lin, Y. K. Shen, and Y. H. Wang
Volume 2017, Article ID 6343724, 9 pages

Collagen Sponge Functionalized with Chimeric Anti-BMP-2 Monoclonal Antibody Mediates Repair of Critical-Size Mandibular Continuity Defects in a Nonhuman Primate Model

Yilin Xie, Yingying Su, Seiko Min, Jianxia Tang, Bee Tin Goh, Leonardo Saigo, Sahar Ansari, Alireza Moshaverinia, Chunmei Zhang, Jinsong Wang, Yi Liu, Arash Khojasteh, Homayoun H. Zadeh, and Songlin Wang
Volume 2017, Article ID 8094152, 11 pages

Cytotoxicity and Antimicrobial Effects of a New Fast-Set MTA

Michelle Shin, Jung-Wei Chen, Chi-Yang Tsai, Raydolfo Aprecio, Wu Zhang, Ji Min Yochim, Naichia Teng, and Mahmoud Torabinejad
Volume 2017, Article ID 2071247, 6 pages

Developing Customized Dental Miniscrew Surgical Template from Thermoplastic Polymer Material Using Image Superimposition, CAD System, and 3D Printing

Yu-Tzu Wang, Jian-Hong Yu, Lun-Jou Lo, Pin-Hsin Hsu, and CHun-Li Lin
Volume 2017, Article ID 1906197, 8 pages

Fabrication of Novel Hydrogel with Berberine-Enriched Carboxymethylcellulose and Hyaluronic Acid as an Anti-Inflammatory Barrier Membrane

Yu-Chih Huang, Kuen-Yu Huang, Bing-Yuan Yang, Chun-Han Ko, and Haw-Ming Huang
Volume 2016, Article ID 3640182, 9 pages

UV Photofunctionalization Effect on Bone Graft in Critical One-Wall Defect around Implant: A Pilot Study in Beagle Dogs

Min-Young Kim, Hyunmin Choi, Jae-Hoon Lee, Jee-Hwan Kim, Han-Sung Jung, Jae-Hong Kim, Young-Bum Park, and Hong-Seok Moon
Volume 2016, Article ID 4385279, 9 pages

Bone Healing Improvements Using Hyaluronic Acid and Hydroxyapatite/Beta-Tricalcium Phosphate in Combination: An Animal Study

Yen-Lan Chang, Yi-June Lo, Sheng-Wei Feng, Yu-Chih Huang, Hsin-Yuan Tsai,
Che-Tong Lin, Kan-Hsin Fan, and Haw-Ming Huang
Volume 2016, Article ID 8301624, 8 pages

Cytotoxicity of Titanate-Calcium Complexes to MC3T3 Osteoblast-Like Cells

Yen-Wei Chen, Jeanie L. Drury, Joelle Moussi, Kathryn M. L. Taylor-Pashow, David T. Hobbs,
and John C. Wataha
Volume 2016, Article ID 7895182, 7 pages

Editorial

Bioengineering Materials in Dental Application

**Wei-Jen Chang,^{1,2} Abe Shinichi,³ Shinji Kamakura,⁴
Ren-Yeong Huang,⁵ and Jung-Wei Chen⁶**

¹*School of Dentistry, College of Oral Medicine, Taipei Medical University, Taipei, Taiwan*

²*Dental Department, Shuang-Ho Hospital, Taipei Medical University, Taipei, Taiwan*

³*Department of Anatomy, Tokyo Dental College, Tokyo, Japan*

⁴*Bone Regenerative Engineering Laboratory, Graduate School of Biomedical Engineering, Tohoku University, Sendai, Japan*

⁵*National Defense Medical Center, Taipei, Taiwan*

⁶*Department of Pediatric Dentistry, Loma Linda University School of Dentistry, Loma Linda, CA, USA*

Correspondence should be addressed to Wei-Jen Chang; cweijen1@tmu.edu.tw

Received 20 July 2017; Accepted 20 July 2017; Published 21 August 2017

Copyright © 2017 Wei-Jen Chang et al. This is an open access article distributed under the Creative Commons Attribution License, which permits unrestricted use, distribution, and reproduction in any medium, provided the original work is properly cited.

Bioengineering materials have been developed and applied in clinical therapy for rehabilitation of edentulous arches. The materials were also known with restoring the function and health in human beings. The concept for current bioengineering materials is based on a scaffold of tissue engineering triangle. Along with this evolution, bioengineering materials application is also accompanied with complications and failures.

This special issue aims to bring together state-of-the-art research contributions on the implants modification and applications to address the reduction of growing concerns after implant surgery. Potential topics of this special issue include UV photofunctionalization effect, mineral trioxide aggregate (MTA), antibody-mediated osseous regeneration (AMOR), computer-aided design (CAD) and 3D printing (3DP), bite force, inflammatory responses, bone healing, orthodontic power chains, and in vitro examination. After rigorous selection, 9 papers were elected.

In the paper “UV Photofunctionalization Effect on Bone Graft in Critical One-Wall Defect Around Implant: A Pilot Study in Beagle Dogs,” M.-Y. Kim et al. address UV photofunctionalization on the surface of implants that caused a large scale defects with bone graft but assists osseointegration and osteogenesis. UV-treated implant surface displayed enhancing osseointegration, such that UV treatment raised bone-to-implant contact being prone to new bone formation at the early stage, around 4 weeks.

In the paper “Cytotoxicity and Antimicrobial Effects of a New Fast-Set MTA,” M. Shin et al. propose the comparison

of biocompatibility and antimicrobial effectiveness between the new Fast-Set MTA (FS-MTA) and ProRoot MTA (RS-MTA). These two endodontic procedure materials were tested to measure antimicrobial effect against bacteria. There is no cytotoxicity or bacterial inhibition observed by FS-MTA, comparing to RS-MTA.

In the paper “Collagen Sponge Functionalized with Chimeric Anti-BMP-2 Monoclonal Antibody Mediates Repair of Critical-Size Mandibular Continuity Defects in a Nonhuman Primate Model,” Y. Xie et al. report a chimeric anti-BMP-2 mAb mediated AMOR in clinically relevant mandibular continuity defect models. Anti-bone BMP-2 mAbs have been identified as an efficacious repair of bone defects. Cone beam computed tomography (CBCT) imaging and histologic detection confirmed de novo bone formation to suggest bone injury may be indispensable for AMOR. Thus, anti-BMP-2 mAb grabbed endogenous BMPs that triggered bone repair.

In the paper “Developing Customized Dental Miniscrew Surgical Template from Thermoplastic Polymer Material Using Image Superimposition, CAD System, and 3D Printing,” Y.-T. Wang et al. study the inflammation or other discomfort symptoms that occurred on placed customized miniscrews after surgery. To fabricate an accurate customized surgical template for dental orthodontic miniscrews, they used the techniques that integration of CBCT and laser scan image superposition, CAD and 3DP, were applied to. The customized miniscrew template showed well-fitting adaption and stable holding power.

In the paper "Influence of Deformation and Stress between Bone and Implant from Various Bite Forces by Numerical Simulation Analysis," H.-C. Cheng et al. look at the influence of different bite forces that triggered deformation and stress on the bone and implant through 3D finite element (FE) methods. Near the implant neck in marginal bone is always accompanied with heavy stresses, revealing the physical force, including horizontal and vertical force, should be noted between implant and bone. Thus, to clinically maintain the structure and function of a bone and implant one should be aware of preserving.

In the paper "Fabrication of Novel Hydrogel with Berberine-Enriched Carboxymethylcellulose and Hyaluronic Acid as an Anti-Inflammatory Barrier Membrane," Y.-C. Huang et al. point out a novel method established to fight against inflammatory responses. It has been well known that antiadhesion barrier membrane refers to a critical biomaterial for tissue protection from complications after surgery. A new hydrogel membrane composed of berberine-enriched CMC papered from bark of the *P. amurensis* tree and HA (PE-CMC/HA) was fabricated in this study, named PE-CMC/HA, by mixing PE-CMC and HA as a base with the addition of polyvinyl alcohol to form a film. The result proved PE-CMC/HA membrane is a useful system for anti-inflammatory berberine release.

In the paper "Bone Healing Improvements Using Hyaluronic Acid and Hydroxyapatite/Beta-Tricalcium Phosphate in Combination: An Animal Study," Y.-L. Chang et al. present the use of HLA as an aqueous binder of hydroxyapatite/beta-tricalcium phosphate (HA- β TCP) particles that decrease the amount of bone graft needed and elevate simplicity of operation in clinical situations. In rabbit, the calvarial bone defects were healed by HA- β TCP powder with HLA. Therefore, HLA addition promoted osteoconduction and also improved handling characteristics in clinical situations.

In the paper "Surface Treatment on Physical Properties and Biocompatibility of Orthodontic Power Chains," H. C. Cheng et al. indicate the development of a surface treatment, nanoimprinting, for orthodontic power chains with alleviation of its shortcomings. After the surface treatment, the contact angle and the color adhesion of the orthodontic power chains became larger and less, respectively.

In the paper "Cytotoxicity of Titanate-Calcium Complexes to MC3T3 Osteoblast-Like Cells," Y.-W. Chen et al. illustrate that monosodium titanates (MST) and MST-calcium (MST-Ca(II)) complexes had a cytotoxicity in MC3T3 osteoblast-like cells. Currently, it is found that MST suppressed MC3T3 cell metabolic activity in a dose-dependent manner; however, the mechanism of how MST and MST-Ca(II) played significantly cytotoxic role with regard to MC3T3 remains unknown. Thus, using the complexes remain with uncertain potential risks.

Acknowledgments

The Guest Editorial Team would like to appreciate authors of all the papers submitted to this special issue. Due to the space limitations, a number of high quality contributions could not be accommodated. We hope that you will enjoy reading this

special issue that contributed to this motivating and fast-evolving field as much as we have done.

*Wei-Jen Chang
Abe Shinichi
Shinji Kamakura
Ren-Yeong Huang
Jung-Wei Chen*

Research Article

In Vitro Laser Treatment Platform Construction with Dental Implant Thread Surface on Bacterial Adhesion for Peri-Implantitis

Hsien-Nan Kuo,¹ Hsiang-I Mei,² Tung-Kuan Liu,¹ Tse-Ying Liu,² Lun-Jou Lo,³ and Chun-Li Lin²

¹Institute of Engineering Science and Technology, National Kaohsiung First University of Science and Technology, Kaohsiung, Taiwan

²Department of Biomedical Engineering, National Yang-Ming University, Taipei, Taiwan

³Department of Surgery, Chang Gung Memorial Hospital, Taoyuan, Taiwan

Correspondence should be addressed to Chun-Li Lin; cllin2@ym.edu.tw

Received 3 January 2017; Revised 9 February 2017; Accepted 7 June 2017; Published 16 July 2017

Academic Editor: Wei-Jen Chang

Copyright © 2017 Hsien-Nan Kuo et al. This is an open access article distributed under the Creative Commons Attribution License, which permits unrestricted use, distribution, and reproduction in any medium, provided the original work is properly cited.

This study constructs a standard in vitro laser treatment platform with dental implant thread surface on bacterial adhesion for peri-implantitis at different tooth positions. The standard clinical adult tooth jaw model was scanned to construct the digital model with 6 mm bone loss depth on behalf of serious peri-implantitis at the incisor, first premolar, and first molar. A cylindrical suite connected to the implant and each tooth root in the jaw model was designed as one experimental unit set to allow the suite to be replaced for individual bacterial adhesion. The digital peri-implantitis and suite models were exported to fulfill the physical model using ABS material in a 3D printer. A 3 mm diameter specimen implant on bacterial adhesion against *Escherichia coli* was performed for gram-negative bacteria. An Er:YAG laser, working with a chisel type glass tip, was moved from the buccal across the implant thread to the lingual for about 30 seconds per sample to verify the in vitro laser treatment platform. The result showed that the sterilization rate can reach 99.3% and the jaw model was not damaged after laser irradiation testing. This study concluded that using integrated image processing, reverse engineering, CAD system, and a 3D printer to construct a peri-implantitis model replacing the implant on bacterial adhesion and acceptable sterilization rate proved the feasibility of the proposed laser treatment platform.

1. Introduction

Dental implants have become a common treatment for missing teeth owing to the advantages in reconstructing the missing tooth form and function without having to prepare the adjacent teeth [1]. The successful dental implant concerns at the early stage are related to osseointegration at the implant-bone interface, while avoiding bone resorption over the long term. The dental implant success rate can reach 90% at the early stage [2]. However, there are still complications such as abutment screw fracture, soft tissue penetration, mucosal inflammation, implant loosening, and bone resorption in long-term treatment [3]. One reason for these complications is peri-implantitis, which is caused by dental calculus attaching to the implant surface leading

to periodontal immune reaction, subsequently causing periodontal inflammation and bone loss [4, 5]. The peri-implantitis is usually treated using conservative mechanical debridement, air abrasives, antiseptic treatment, laser, and so on. However, all of these methods have no consistent clinical standard [6]. Muthukuru et al. compared nonsurgical methods such as topical antibiotics, air abrasives, and Er:YAG (Erbium doped: Yttrium-Aluminum-Garnet) laser treatment and found that these three methods can all be remitted for peri-implantitis [6].

The Er:YAG laser was first proposed by Zharikov in 1974 [7]. It is a 2940 nm wave length laser with the closest connection to water among the existing lasers. It can be applied to both hard and soft tissues, cut and treated under water conditions. This dental laser has the highest potential

for peri-implantitis treatment. Many studies focused on periodontal diseases suggested that using the Er:YAG laser with the chisel type tip [8, 9] and the angle with tooth surface should be 20° – 40° to meet the cleaning dental calculus requirement, while avoiding hurting the cementum. It was also found that laser treatment efficiency is related to parameters such as power, treatment time, tip type, and tooth position. However, a smooth titanium plate is usually used as the test specimen to investigate the parameter influence in laser treatment in most current researches [10, 11]. The smooth titanium plate surface is quite different from the dental implant thread surface and the thread shape on the implant surface may have a covering or reflection effect to the laser light. The laser illumination angle limitation caused by the interference of nearby teeth and surrounding bone resorption can make the clinical situation different from in vitro metal plate experiments and bring doubt to the result. Unfortunately, until now there has been no in vitro laser experiment platform that considers different tooth positions with the levels of periodontal diseases using a real dental implant with threaded surface.

The bacteria description in Er:YAG laser treatment for peri-implantitis in the current literature is relatively scarce. It is now known that periodontal disease or peri-implantitis is caused by gram-negative bacteria and negative lipopolysaccharide body (LPS) produced by anaerobic bacteria [12–14]. Common periodontal bacteria include *Porphyromonas gingivalis*, *Prevotella intermedia*, *Prevotella denticola*; these periodontal bacteria can cause inflammation and immunity changes in periodontal tissues, inducing the osteophagocytic excitation for osseointegration failure and bone resorption [15, 16]. In 2016, Chen et al. used three kinds of intervention-plastic curettage, air-powder abrasive system, and Er:YAG laser to verify the sterilization effect on a titanium surface for dental implant *Escherichia coli* bacteria adhesion [17]. The results showed that the Er:YAG laser can kill bacteria effectively and does not hurt the implant surface.

This study constructed a standard in vitro laser treatment platform that complies with real clinical situations, including different teeth positions and levels of periodontal diseases. This platform permits laser tip treatment at different teeth positions with varying angles. The implant with bacterial adhesion was designed using an extraction suite that can replace the bacterial adhesion implant extraction. Er:YAG laser treatment for peri-implantitis was performed to verify the test platform and sterilization feasibility.

2. Materials and Methods

Peri-Implantitis Model

Figure 1 is the flowchart for the peri-implantitis in vitro testing model construction. The standard clinical adult tooth jaw model (PRO2002-UL-SP-FEM-28, Nissin Dental Products Inc., Japan) and three 11.5 mm length dental implants with diameters of 3 mm, 4 mm, and 5 mm, used for the incisor, premolar, and molar, respectively, were selected as the experimental samples (AnkerSB, Alliance Global Technology Co., Ltd., Taiwan). The i-CAT Dental CT (Imaging Sciences

International, PA, USA) were used to scan the tooth jaw model and dental implants. All DICOM CT cross section image data were processed on personal PC using commercially available image-processing software (Mimics® v. 10.01; Materialize Co., Leuven, Belgium) to identify the contours of the different materials. Those contours were extracted and converted into mathematical entities. A 3D digital tooth jaw model and three dental implant solid models were reconstructed in a CAD system (Creo Parametric 2.0, PTC Inc., Needham, MA, USA). Three implants with different diameters assembled in the relative middle incisor, premolar, and molar tooth jaw model positions and implant directions were referenced to the major axis angle of the near teeth.

According to the CIST (Cumulative Interceptive Supportive Therapy) peri-implantitis [18], mechanical debridement and surgical operation classification were needed when the bone loss depth was greater than 5 mm. Following this standard, 6 mm bone loss depth was defined in our model on behalf of serious peri-implantitis, which usually requires a flap in clinical surgery.

The periodontal pocket dimensions were defined as the maximum limitation with the root of the near teeth based on common alveolar bone loss appearance in X-ray images and were as 1.8 mm around the implant for the incisor, 2 mm in the upper part (occlusal direction), and 1.8 mm in the lower part (root direction) for the first premolar and 3 mm in the upper part (occlusal direction) and 2 mm in the lower part (root direction) for the first molar (Table 1). Structural solid models of these three periodontal pockets were constructed and edited in the CAD system.

A cylindrical suite connected to the implant and each tooth root in the jaw model was designed to permit the suite to be replaced for individual bacterial adhesion. The dental implant and the suite made one experimental unit set in which the bacterial culture can be performed (Figure 2). The digital peri-implantitis and suite models were exported as a stereolithographic (STL) file that can be loaded into a fused deposition modeling (FDM) 3D printer (3DP) with 0.254 mm slicing additive manufacturing (Dimension 1200es SST, Stratasys, Ltd., Minnesota, USA) to duplicate the ABS material (ABS-P430, Stratasys, Ltd., Minnesota, USA).

3. Bacterial Culture and Adhesion

The jaw model at the incisor was used to verify our platform feasibility in bacterial adhesion and laser sterilization experiments. Three samples were performed in both experiments. The bacterial adhesion to the specimens against *Escherichia coli* (ATCC®25922™ KWIK-STIK, Microbiologics, Inc., USA) was investigated as a model for gram-negative bacteria. Bacteria were cultured onto the solid medium (Agar base, Oxoid Ltd., Basingstoke, Hampshire, UK) and placed into an incubator (37°C) for 24 hours for agar cultivation (Figure 3(a)). Broth medium cultivation was then performed in a spectrophotometer (DU800, Beckman Coulter, Fullerton, CA, USA) operated in the wavelength 600 nm with read average time 0.5 sec (at three circulation) to measure its liquid OD (Optical Density) for quantized correction (Figure 3(b)).

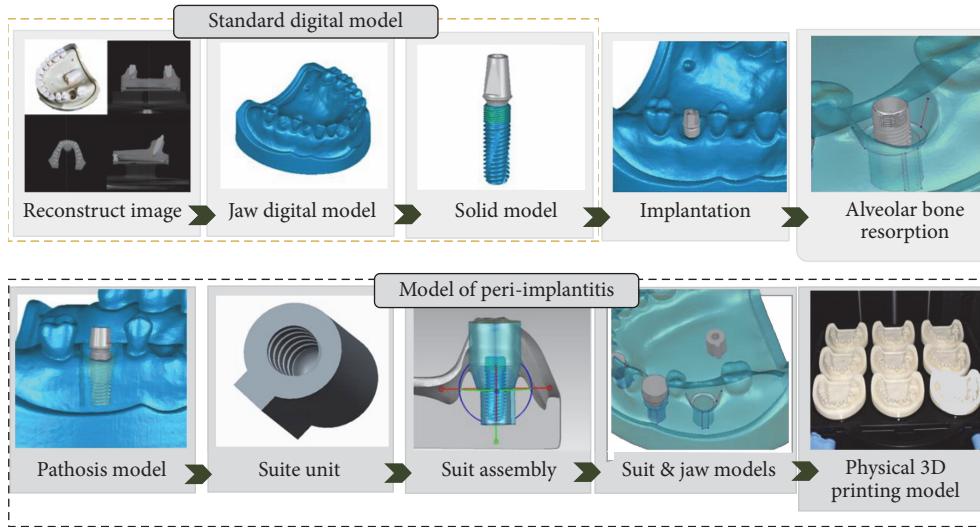


FIGURE 1: The flowchart for the peri-implantitis in vitro testing model construction.



FIGURE 2: The implant and the suite made one experiment unit set.

TABLE 1: Implant placed positions and definition of alveolar bone resorption (periodontal pocket dimensions) for incisor, premolar, and molar.

Position	Implant position and alveolar bone resorption			
	Height	Position	Angle	Alveolar resorption
Incisor				
Premolar				
Molar				

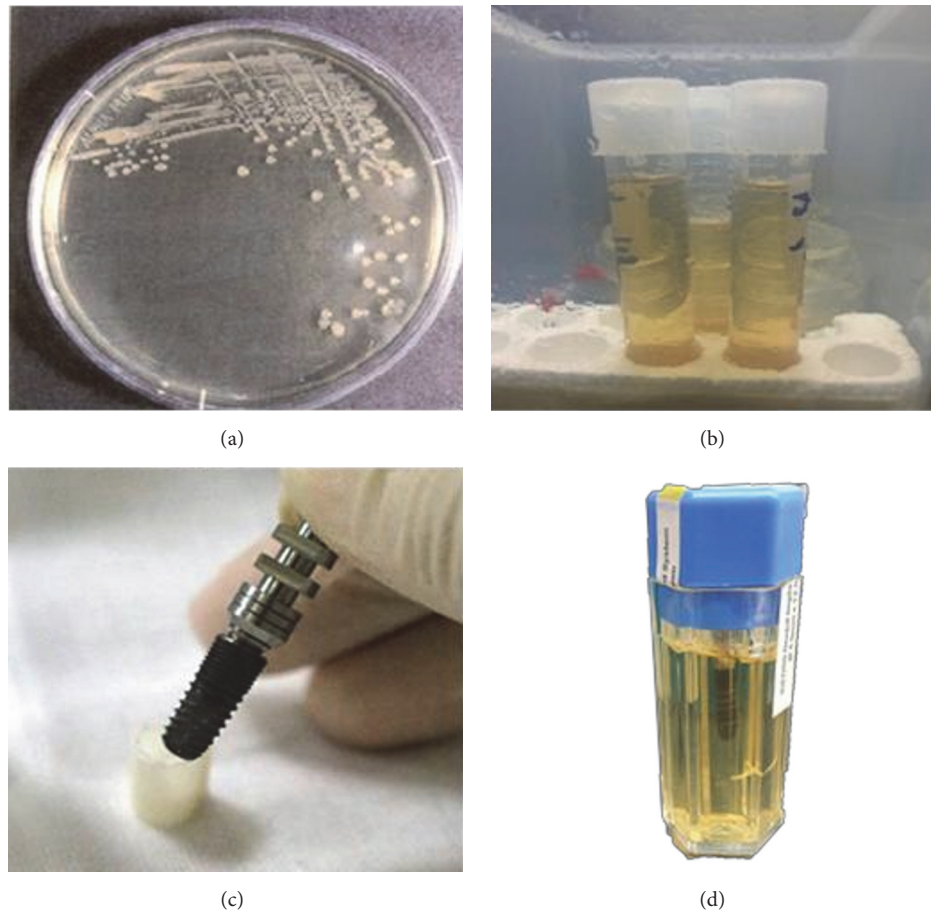


FIGURE 3: Bacterial culture. (a) Agar culture. (b) Broth culture. (c) Installed implant specimen. (d) Bacteria (*Escherichia coli*) culture with implant.

A 3 mm diameter implant and corresponding suite were used to fulfill a set for the bacterial adhesion experiment (Figure 3(c)). The set was placed into medium at 37°C temperature incubator for 24 hours (Figure 3(d)) and 2 ml medium added to centrifuge tubes. The liquid OD was measured with a spectrophotometer and diluted 10:1. Plate count was performed to test the adhesion effect after 5 minutes shaking using an ultra-sonicator.

Three dental set samples were assembled into the 3DP jaw model and irradiated with the Er:YAG laser (Er:YAG laser, LightMed Dental Technology Corp., Taiwan) working at 2940 nm with pulse energy at the tip*85 mJ/pulse. A periodontal hand piece was used with a chisel type glass tip (Figure 4). The application tip was moved from the buccal across the implant thread to the lingual and occlusal to the root directions for about 30 seconds per sample. The abutment was then removed and the implant with healing cap was disassembled to form the model set. The implant was placed into a centrifuge tube for the bacteria count (Figures 4(c) and 4(d)). The bacteria number was counted by plate count after 5 minutes shaking using an ultrasonicator (Elmasonic P, Elma Group Inc., Pforzheim, Germany) with frequency 37 KHZ at

21°C for continuity. The *T*-test method was performed to understand the variations between different groups.

4. Results

Figure 5(a) shows the peri-implantitis in vitro testing model with 3DP jaw ABS model with different teeth positions such as incisor, premolar, and molar. Different dental implants can be assembled and replaced in the 3DP jaw model based on the clinical requirement (Figure 5(b)).

The results indicated that gram-negative bacterium *Escherichia coli* can be cultured to find the calibration curve. The number of bacterial colonies was 10^7 when the OD value was 0.1. The bacteria adhered onto the implant successfully about 1.01% to 3.83% of the adhesion rate after 24 hours of culture owing to micropores on the implant surface (Table 2). The Er:YAG dental laser sterilization result showed that the sterilization rate can reach 99.3% (standard deviation is ± 1.03) (Table 3). Noncontact video measurement system (SVP-2010, ARCS Co., Ltd., Taichung, Taiwan) observations were performed in evaluating jaw model defects. The images were obtained using 37.5 times magnification with a color

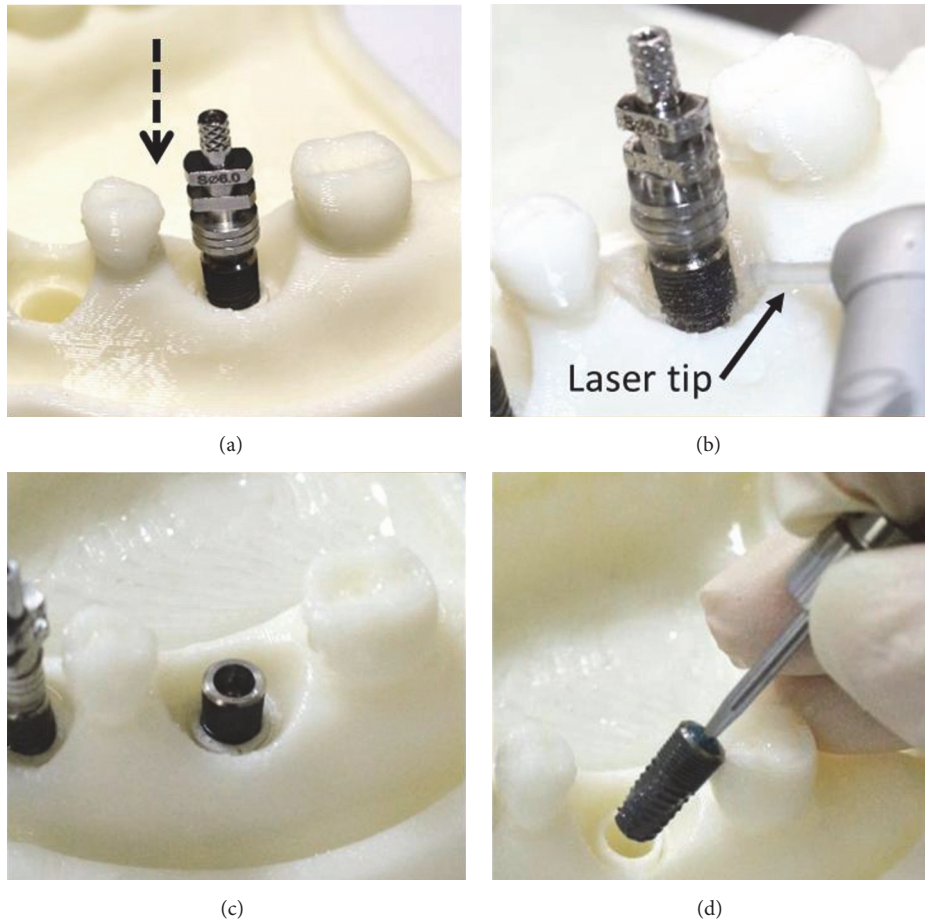


FIGURE 4: Laser experiment process. (a) Implantation model. (b) Laser treatment. (c) Removal of implant abutment. (d) Removal of implant.

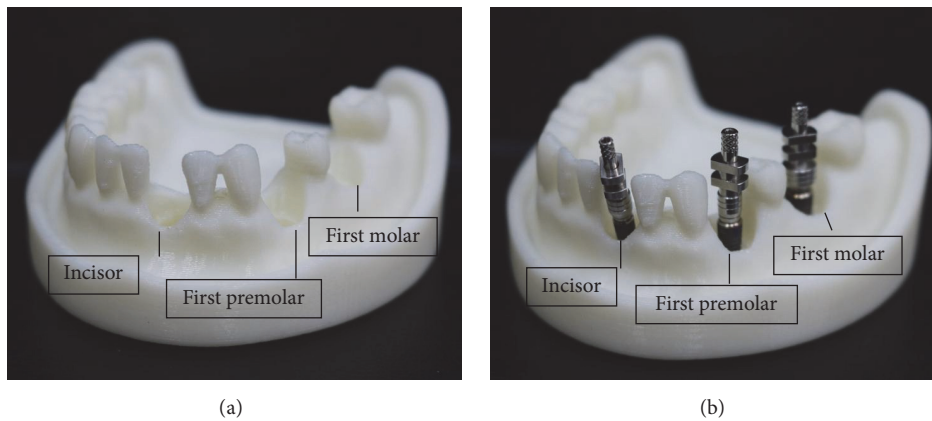


FIGURE 5: Physical ABS 3D printing model of peri-implantitis for (a) jaw tooth model; (b) jaw tooth and three implants.

CCD camera and transferred into an imaging program to evaluate whether the jaw model fractured/melted. No damage was found on the jaw model after laser irradiating testing.

5. Discussion

No standard model exists that represents all clinical situations because of the large variation in tooth, dental arch, and

TABLE 2: Dental implants on bacterial adhesion.

	Number of bacteria (N_b) (CFU/ml)	Bacterial adhesion (N_{ba}) (CFU/ml)	Adhesion percentage (N_{ap}) (%) $N_{ap} = \left[\frac{N_{ba}}{N_b} \right] \times 100\%$
1	2.799×10^7	3.5×10^5	1.25
2	2.235×10^7	8.6×10^5	3.83
3	2.388×10^7	2.4×10^5	1.01

TABLE 3: Dental laser sterilization.

	Number of bacteria (N_b) (CFU/ml)	Bacterial residual (N_{br}) (CFU/ml)	Sterilization rate (N_{sr}) (%) $N_{sr} = \left[\frac{N_b - N_{br}}{N_b} \right] \times 100\%$	Mean \pm SD
1	3.189×10^5	0	100	
2	2.84×10^6	3.3×10^3	99.8	99.3 ± 1.03
3	5.333×10^5	1×10^4	98.1	

alveolar bone anatomy and the different peri-implantitis periodontal pocket structures, bone absorption, degree of inflammation, and implant types found in individual patients. Therefore, many dental laser treatment parameters do not comply with the actual clinical status. The corresponding results from using a smooth disk titanium plate as the jaw model in the literature are quite different from the dental implant thread surface.

An adult tooth jaw model was selected as the standard model due to the shape of its teeth, and arch form and alveolar bone are similar to that in the common healthy adult. This artificial model is also a highly acceptable model for the dentist to practice with and study in the clinic. Although this jaw model was used to simulate the appearance of nearby tooth mesial and distal peri-implantitis and arch form sides, different levels of peri-implantitis at different teeth needed to be defined in detail and created in the standard digital jaw model. The bone loss depth and periodontal pocket were currently used to indicate the severity of peri-implantitis disease; axisymmetric funnel bone loss shape around the tooth was constructed based on X-ray images from clinical patients using reverse engineering and CAD system to mimic the peri-implantitis geometry. The digital peri-implantitis models combined with a novel designed suite can replace implant output to fulfill the final peri-implantitis physical model using ABS material and a 3D printer. The in vitro testing platform construction for peri-implantitis can be performed after bacterial adhesion onto the implant thread surface to irradiate for sterilization.

Although this artificial model cannot reproduce all peri-implantitis states it is relatively real and similar to clinical situations. The mesial/distal influence of nearby teeth and alveolar bone anatomy was considered in the laser system sight and route. A complicated implant thread surface was used instead of the previous smooth disk metal surface to receive radiation vertically. Bone loss depth quantification and different tooth positions can also provide better study parameters for clinical dentists.

Peri-implantitis is caused by gram-negative and anaerobic bacteria. Two major concerns were considered to use *Escherichia coli* as the target bacteria in our sterilization verification study. One was that the objective of this study was to construct a standard in vitro laser treatment platform including different teeth positions placed implant with bacterial adhesion and levels of periodontal diseases. The bacterial culture and adhesion procedures need easy control and stability on the implant. Another concern was peri-implantitis usually caused by gram-negative bacteria and negative lipopolysaccharide body (LPS) produced by anaerobic bacteria [12–14]. Nevertheless, *Escherichia coli* is easier to achieve than that of gram-positive strains with their comparably massive cell-wall-structure [17]. It was validated to adhere onto the implant surface in the literature and the requirement for anaerobic bacterial growth environment is strict and difficult to control [17]. Although the laser methods used by dentists differ due to habit, 98.9% sterilization rate was reached in our peri-implantitis model with a dead angle of nearby mesial/distal teeth under constant laser power. A better in vitro platform was constructed for future laser treatment time research or other parameters which is closer to actual clinical situations.

6. Conclusion

This study integrated image processing, reverse engineering, and CAD system to design a peri-implantitis model with different teeth positions in a jaw model. A physical peri-implantitis jaw model made using the ABS 3D printer and individual implant thread surface can be output for bacterial adhesion. The verification experiment used the Er:YAG laser for 30 seconds on the implant surface, reaching 98.9% sterilization rate. These results prove the feasibility of our platform and meet the clinical requirement.

Conflicts of Interest

The authors declare that they have no conflicts of interest.

Acknowledgments

This study is supported in part by BY-12-05-28-105 of the Southern Taiwan Science Park Bureau, Ministry of Science and Technology, Taiwan. The authors would like to acknowledge Alliance Global Technology Co., Ltd., Taiwan, for providing the implants for experimentation.

References

- [1] E.-S. Kim and S.-Y. Shin, "Influence of the implant abutment types and the dynamic loading on initial screw loosening," *Journal of Advanced Prosthodontics*, vol. 5, no. 1, pp. 21–28, 2013.
- [2] T. Albrektsson and N. Donos, "Implant survival and complications. The Third EAO consensus conference 2012," *Clinical Oral Implants Research*, vol. 23, supplement 6, pp. 63–65, 2012.
- [3] J. Lindhe and S. Nyman, "The effect of plaque control and surgical pocket elimination on the establishment and maintenance of periodontal health. A longitudinal study of periodontal therapy in cases of advanced disease," *Journal of Clinical Periodontology*, vol. 2, no. 2, pp. 67–79, 1975.
- [4] A. Mombelli and N. P. Lang, "Microbial aspects of implant dentistry," *Periodontology 2000*, vol. 4, no. 1, pp. 74–80, 1994.
- [5] A. Mombelli, M. A. C. van Oosten, E. Schürch Jr., and N. P. Lang, "The microbiota associated with successful or failing osseointegrated titanium implants," *Oral Microbiology and Immunology*, vol. 2, no. 4, pp. 145–151, 1987.
- [6] M. Muthukuru, A. Zainvi, E. O. Esplugues, and T. F. Flemmig, "Non-surgical therapy for the management of peri-implantitis: a systematic review," *Clinical Oral Implants Research*, vol. 23, supplement 6, pp. 77–83, 2012.
- [7] A. Mombelli and N. P. Lang, "Antimicrobial treatment of peri-implant infections," *Clinical Oral Implants Research*, vol. 3, no. 4, pp. 162–168, 1992.
- [8] F. Schwarz, A. Sculean, M. Berakdar, L. Szathmari, T. Georg, and J. Becker, "In vivo and in vitro effects of an Er:YAG laser, a GaAlAs diode laser, and scaling and root planing on periodontally diseased root surfaces: a comparative histologic study," *Lasers in Surgery and Medicine*, vol. 32, no. 5, pp. 359–366, 2003.
- [9] U. Keller, K. Stock, and R. Hibst, "Morphology of Er:YAG laser-treated root surfaces," in *Proceedings of the Medical Applications of Lasers in Dermatology, Ophthalmology, Dentistry and Endoscopy*, pp. 24–31, September 1997.
- [10] T. Matsuyama, A. Aoki, S. Oda, T. Yoneyama, and I. Ishikawa, "Effects of the Er:YAG laser irradiation on titanium implant materials and contaminated implant abutment surfaces," *Journal of Clinical Laser Medicine and Surgery*, vol. 21, no. 1, pp. 7–17, 2003.
- [11] M. Folwaczny, G. George, L. Thiele, A. Mehl, and R. Hickel, "Root surface roughness following Er:YAG laser irradiation at different radiation energies and working tip angulations," *Journal of Clinical Periodontology*, vol. 29, no. 7, pp. 598–603, 2002.
- [12] R. J. Genco, "Assessment of risk of periodontal disease," *Compendium (Newtown, Pa.) Supplement*, vol. 18, pp. S678–S683, quiz S714–7, 1994.
- [13] R. C. Page, "The role of inflammatory mediators in the pathogenesis of periodontal disease," *Journal of Periodontal Research*, vol. 26, no. 3, part 2, pp. 230–242, 1991.
- [14] M. A. Listgarten and C.-H. Lai, "Comparative microbiological characteristics of failing implants and periodontally diseased teeth," *Journal of Periodontology*, vol. 70, no. 4, pp. 431–437, 1999.
- [15] T. G. Wilson Jr and F. L. Higginbottom, "Periodontal Diseases and Dental Implants in Older Adults," *Journal of Esthetic and Restorative Dentistry*, vol. 10, no. 5, pp. 265–271, 1998.
- [16] M. HP, *Periodontal Microbiology. Periodontology: The Essentials*, New York Thieme, New York, NY, USA, 2004.
- [17] C.-J. Chen, S.-J. Ding, and C.-C. Chen, "Effects of surface conditions of titanium dental implants on bacterial adhesion," *Photomedicine and Laser Surgery*, vol. 34, no. 9, pp. 379–388, 2016.
- [18] N. D. Shumaker, "Periodontal and periimplant maintenance: a critical factor in long-term treatment success," *Compendium of Continuing Education in Dentistry*, vol. 30, no. 7, pp. 388–390, 2009, quiz 407, 418.

Research Article

Influence of Deformation and Stress between Bone and Implant from Various Bite Forces by Numerical Simulation Analysis

Hsin-Chung Cheng,^{1,2} Boe-Yu Peng,^{1,2} May-Show Chen,^{2,3} Chiung-Fang Huang,^{4,5} Yi Lin,⁶ and Yung-Kang Shen⁴

¹*School of Dentistry, College of Oral Medicine, Taipei Medical University, Taipei, Taiwan*

²*Department of Dentistry, Taipei Medical University Hospital, Taipei, Taiwan*

³*School of Oral Hygiene, College of Oral Medicine, Taipei Medical University, Taipei, Taiwan*

⁴*School of Dental Technology, College of Oral Medicine, Taipei Medical University, Taipei, Taiwan*

⁵*Division of Family Dentistry, Department of Dentistry, Taipei Medical University Hospital, Taipei, Taiwan*

⁶*Department of Business Administration, Takming University of Science and Technology, Taipei, Taiwan*

Correspondence should be addressed to Yung-Kang Shen; ykshen@tmu.edu.tw

Received 18 January 2017; Accepted 27 March 2017; Published 28 May 2017

Academic Editor: Ren-Yeong Huang

Copyright © 2017 Hsin-Chung Cheng et al. This is an open access article distributed under the Creative Commons Attribution License, which permits unrestricted use, distribution, and reproduction in any medium, provided the original work is properly cited.

Endosseous oral implant is applied for orthodontic anchorage in subjects with multiple tooth agenesis. Its effectiveness under orthodontic loading has been demonstrated clinically and experimentally. This study investigates the deformation and stress on the bone and implant for different bite forces by three-dimensional (3D) finite element (FE) methods. A numerical simulation of deformation and stress distributions around implants was used to estimate the survival life for implants. The model was applied to determine the pattern and distribution of deformations and stresses within the endosseous implant and on supporting tissues when the endosseous implant is used for orthodontic anchorage. A threaded implant was placed in an edentulous segment of a human mandible with cortical and cancellous bone. Analytical results demonstrate that maximum stresses were always located around the implant neck in marginal bone. The results also reveal that the stress for oblique force has the maximum value followed by the horizontal force; the vertical force causes the stress to have the minimum value between implant and bone. Thus, this area should be preserved clinically to maintain the structure and function of a bone implant.

1. Introduction

The lifetime of a buried implant is evaluated by two phases as masticatory forces are applied: the unloaded healing phase and functional phase. Implants may fail during either phase, typically for different reasons. Failure during the first phase happens within a short time after implant placement and is associated primarily with inflammation [1]. Failure during the second phase takes place after implant loading and is associated mainly with direction of a load incorrectly oriented along the long axis of an implant [2, 3]. Implant size affects the area of possible retention in bone; factors such as occlusion, masticatory force, number of implants, and implant position within prosthesis affect forces acting on bone adjacent to implants [4]. Kashi et al. [5] showed

that maximum stresses happened at the location of the first screw hole (closest to the condyle) of an implant. The highest microstrain was observed in bone adjacent to the first screw hole.

An applied mechanical force generates stress and strain in bone, deforming its structural arrangement. Van Oosterwyck et al. [6] showed that a dehiscence can happen when a narrow alveolar bone ridge is served with an oral implant. The presence of buccal and/or lingual dehiscence leads to a marked increase in marginal bone strain at the implant's mesial and distal sides. Faegh and Muftu [7] revealed that the highest continuous interfacial stresses exist in the region where an implant collar engages the cortical region and near the implant apex in the subcortical region. Detolla et al. [8] took advantage of computer-aided design (CAD) and FEA

to evaluate stresses on implant surfaces and in surrounding bone. Menicucci et al. [9], who used two-dimensional (2D) and three-dimensional (3D) finite element analysis (FEA) to determine peri-implant stress occurring during tooth loading, revealed that the static load was more harmful for peri-implant bone than transitional load. Tada et al. [10] applied three-dimensional finite element analysis to evaluate the effect of implant type and length. The results demonstrated that cancellous bone of higher rather than lower density might ensure a better biomechanical environment of implant. Geng et al. [11] reviewed the application of FEA in dental implant studies. Based on clinical observations, some dentists have declared that marginal bone loss around the implant neck is approximately 0.5–1 mm or as high as 1.5 mm during the first year after implant loading. Subsequently, the loss rate of bone is considered either stable or significantly reduced (bone loss of approximately 0.1 mm), or resort of the bone crest continues and the implant is ultimately lost. These findings are in accordance with those gained 3D mathematical models of dental implants under nonaxisymmetrical loading, demonstrating that maximum stress happened around the implant neck.

This study compared the effect of various bite forces (vertical force, horizontal force, and oblique force) on deformation and stress distributions around the implant. The vertical force is the normal chewing ability (masticatory force). The horizontal force means the molar force when human being is sleeping. The oblique force is as the human being eats the irregular food (special masticatory force). Thus, single cylindrical dental implant placed vertically into the molar region of the mandible was modeled using 3D graphics. Deformation and stress distribution in the bone socket after loading by bite force in different directions was computed by FEA.

2. Numerical Method

A computer tomography (CT) scanner of dentistry (i-CAT 3D; Imaging Sciences International, Inc., USA) was applied to scan a patient's mandible. The patient was a 35-year-old male recruited from Taipei Medical University Hospital, Taiwan. Mill and Amira V3.1.1 software program was taken advantage of to integrate the dental CT scan and 3D model. Finally, this study employs the Solidworks software to get the STL file of the 3D model. This model can be applied as the initial model for numerical simulation using ANSYS software. Figure 1 shows the process of this schedule. Finite element analysis is commonly applied for deformation and stress analysis of nonrigid bodies. The area of interest, the model (an implant and part of a mandible list in Figure 2), is divided into element meshes. The material properties of implant system bone are shown in Table 1. Figure 3 shows the model of implant system and cancellous bone. The physical properties of each element are fixed. Boundary conditions, restrictions to physical properties stemming from the physical behavior of the patient, are used for outer model elements. Deformation or stress, for example, was determined within each element in the model. In this study, FEA was used to analyze deformations and stresses created by different bite forces around cylindrical dental implants. Dimensions of the reference implant were

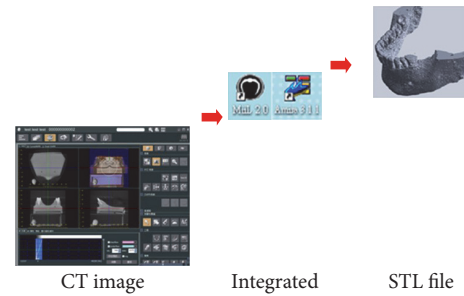


FIGURE 1: 3D model creation for numerical simulation.

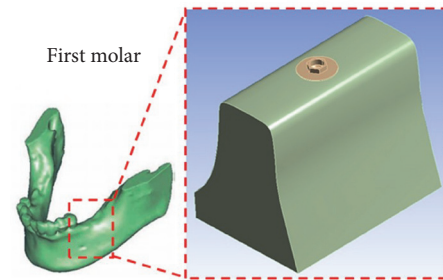


FIGURE 2: Mandible model for numerical simulation.

selected based on those of the implant most frequently used in Taiwan (data were obtained from implant distributors).

The mesial and distal borders of the end of the modeled mandible section were restricted, such that displacement of nodes in all directions was zero. The whole bone was supposed as a homogenous and isotropic material with the characteristics of cancellous bone. This was realized as spongy bone that changed its structure after successful implant placement and the implant interface changes into increasing similar to cortical bone. The tooth is zirconia material. The most frequently used implants in Taiwan are 4.5 mm in diameter, 0.7 mm in pitch, and 8 mm in length. Relying on implant size, the models consisted of 27855 elements and 47646 nodes (Figure 4).

Geometric three-dimensional models of the implant and molar region of the mandible and material properties (previously mentioned) of bone were simplified to decrease computing time and memory consumption. The authors suppose these geometric modifications do not influence computational accuracy in terms of deformation and stress distributions. The simplifications applied in this study did not affect analytical results, because all models had undergone the same simplification. Model simplification has a basis; important factors are taken into account; so the differences with the real results are not.

To yield the 3D model, pre- and postprocessor ANSYS computer-aided engineering (CAE) in FEA software (ANSYS V12) was applied. This pre- and postprocessor offers a parametric definition of geometry and the FE mesh (ANSYS, V12).

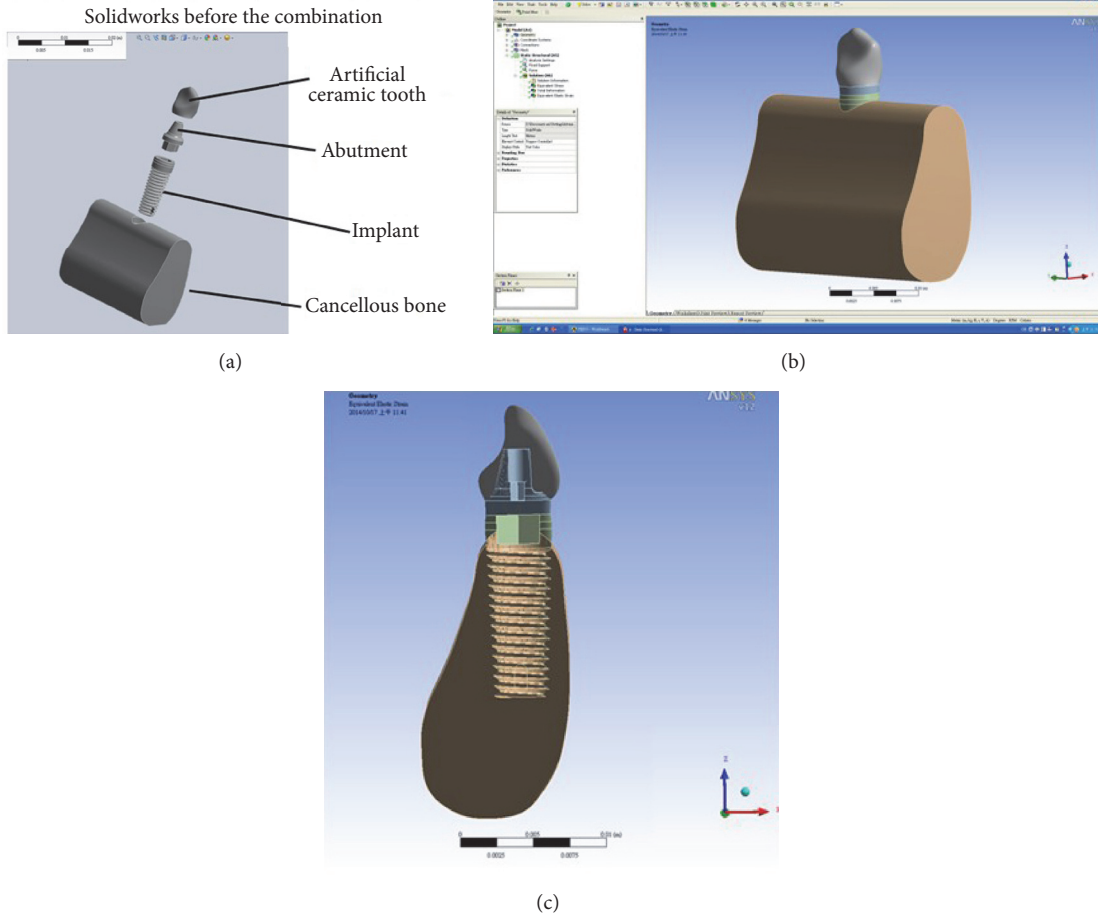


FIGURE 3: Implant system: (a) part, (b) assembly, and (c) cross section.

TABLE 1: Material properties of implant system.

	Tooth (zirconia)	Abutment (titanium)	Implant (titanium)	Cancellous bone
Young's modules (Pa)	2×10^{11}	9.6×10^{10}	9.6×10^{10}	1.37×10^9
Poisson's ratio	0.3	0.3	0.3	0.3

Loading of implants in three dimensions with various bite forces (masticatory force (vertical force), molar force (horizontal force), and special masticatory force (oblique force)) (Figure 5), the values of the bite forces used are 500 N, 1000 N, 1500 N, 2000 N, and 2500 N. The special masticatory force in different angles (30°, 45°, and 60°) is used relative to the occlusal plane. This 3D loading acted on the center of the upper surface of the tooth. Force magnitudes, as well as the acting point, were chosen based on previous work at Taipei Medical University Hospital. Assuming that the implant binds to the bone, the interfacial condition is bonded [12]. Pre- and postprocessing were conducted on a personal computer (PC). The CPU of PC had an Intel type (Core 2 Q8200) and 3.5 GB RAM. Computation time for each simplified single-size implant was approximately one and half hours. All computations were fulfilled for the 3D models.

The authors had done the test of element quality; element quality is mostly close to 1. So the results are credible. The deformation and stress (Pa) at the implant-bone interface were computed using FEA software.

3. Results and Discussion

Figure 6 shows the deformation distributions of various masticatory forces (500 N–1000 N). Figures 6(a) and 6(b) show that the maximum deformation value occurs on the top of the tooth. Deformation value decreases as the deformation position goes to the bottom of implant. Figures 6(c) and 6(d) indicate that the maximum deformation value occurs on the top of the tooth. Deformation value decreases as the deformation position goes to the implant abutment. The deformation distribution of implant presents the symmetry

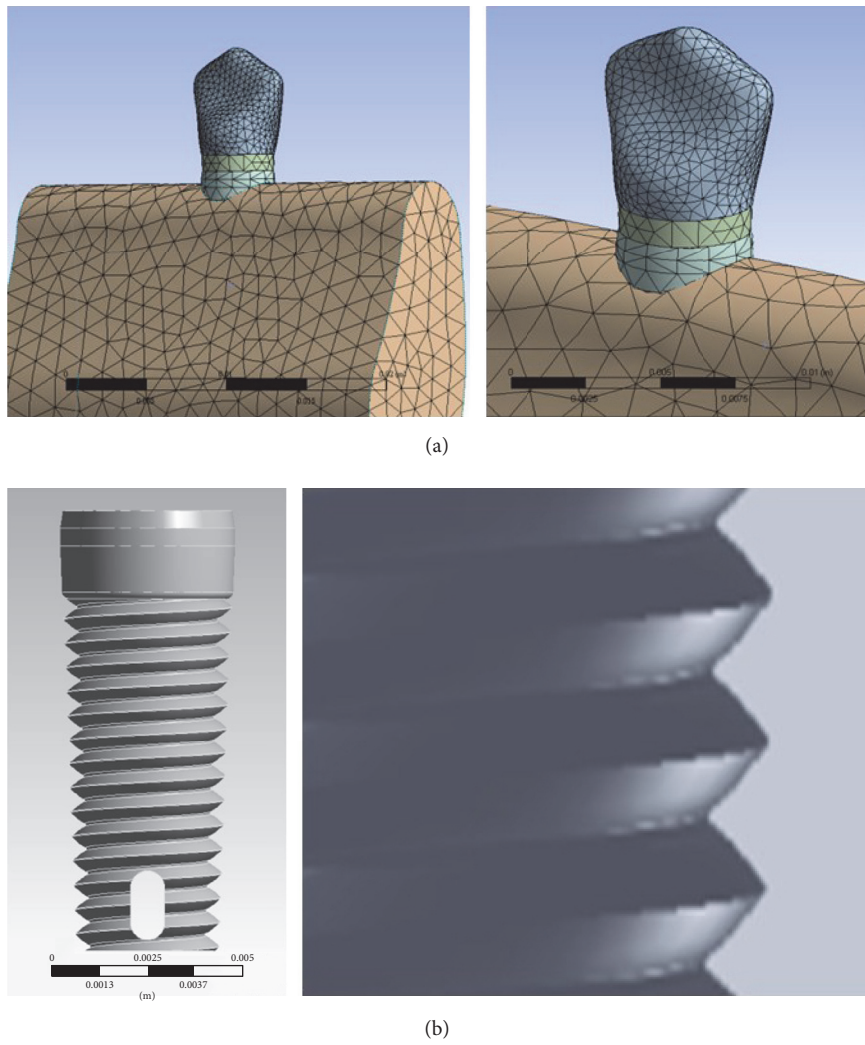


FIGURE 4: Mesh and screw type of implant system: (a) mesh and (b) screw type (diameter = 4.5 mm, pitch = 0.7 mm).

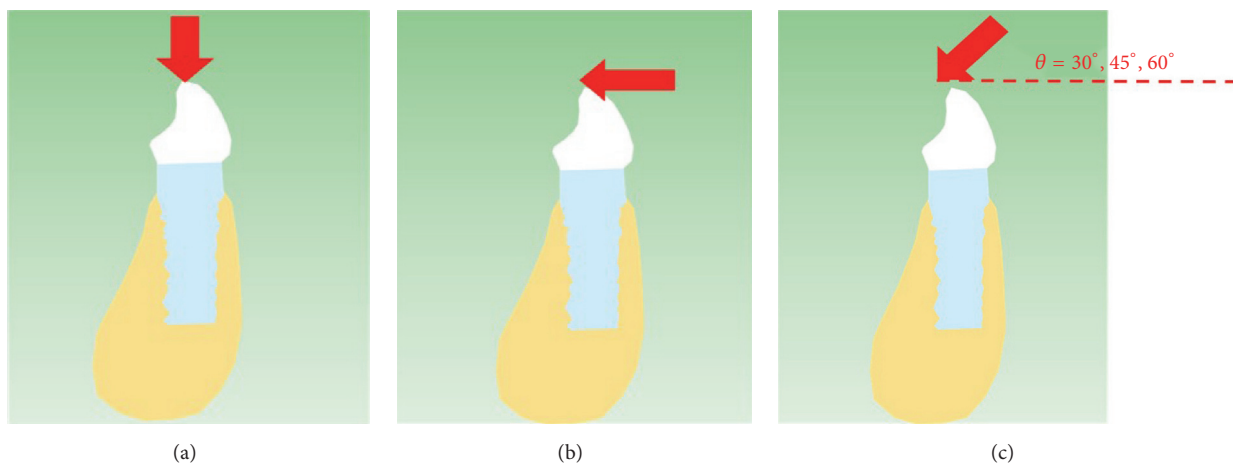


FIGURE 5: Various bite forces: (a) vertical force, (b) horizontal force, and (c) oblique force.

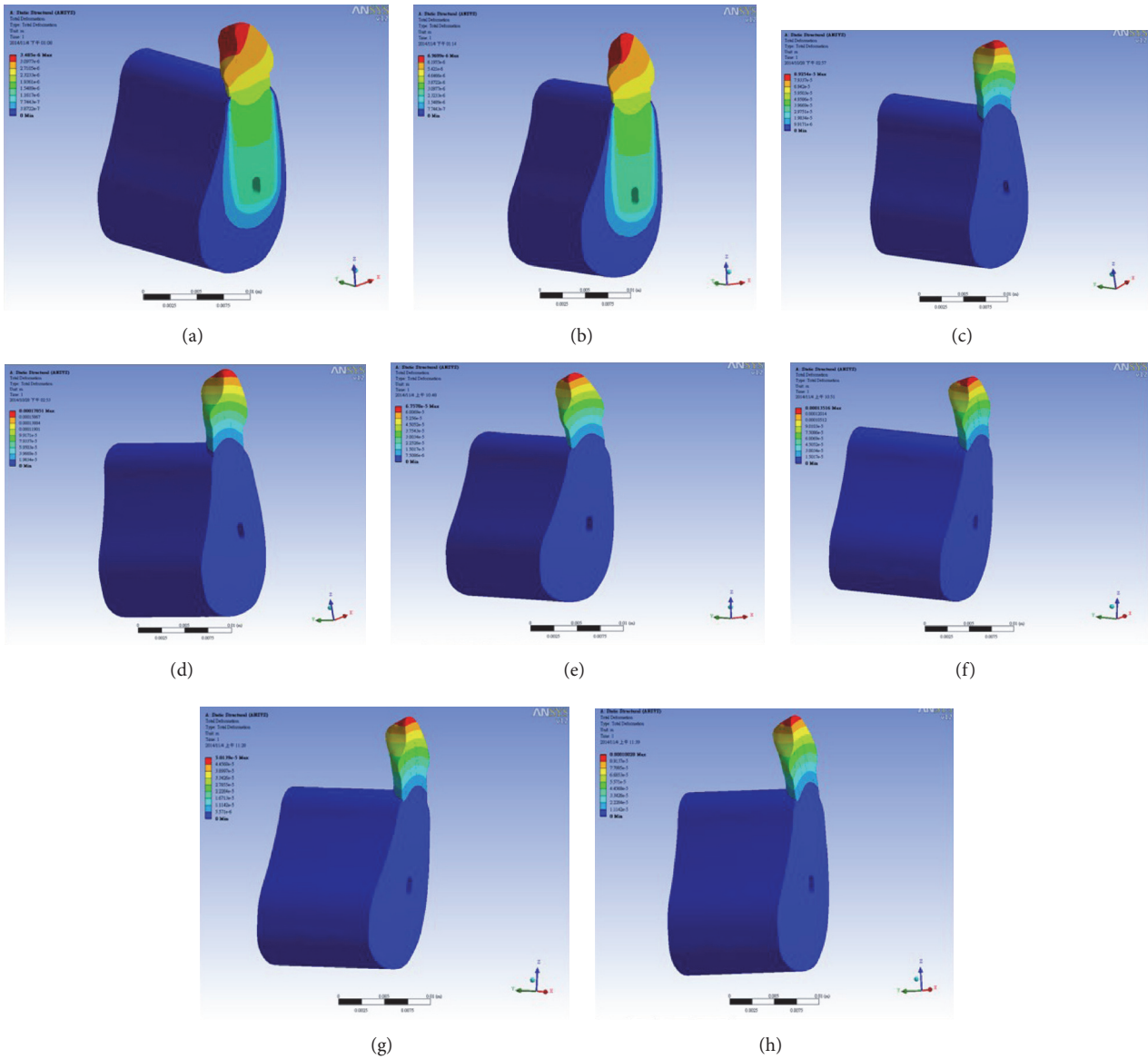


FIGURE 6: Deformation distributions for various forces: (a) 500 N, vertical force; (b) 1000 N, vertical force; (c) 500 N, horizontal force; (d) 1000 N, horizontal force; (e) 500 N, oblique force (45°); (f) 1000 N, oblique force (45°); (g) 500 N, oblique force (60°); (h) 1000 N, oblique force (60°).

by means of the central axis of the tooth. The deformation distribution of implant system by horizontal force has the difference among it by vertical force. Figures 6(e) and 6(f) reveal that the maximum deformation value takes place on the top of the tooth. Deformation value decreases as the deformation position goes to the implant abutment. The deformation distribution by oblique force (45°) shows the symmetry by means of the central axis of the tooth. The deformation distribution of implant system by vertical force demonstrates the oblique shape on the tooth. Figures 6(g) and 6(h) show that the maximum deformation value occurs on the top of the tooth. Deformation value decreases as the deformation position goes to the implant abutment. The deformation distribution of implant by oblique force (60°) presents the symmetry by means of the central axis of the

tooth. The deformation distribution of implant system by oblique force (60°) has the difference among it by vertical force. Figure 7 shows the stress distributions of various masticatory forces (500 N–1000 N). A study goal was to identify the exact location of the implant abutment. Analytical results for Figures 7(a) and 7(b) demonstrate that maximum stress was on the neck of the implant abutment. Additionally, the neck of the implant abutment was the weak point. Analytical results for Figures 7(c) and 7(d) demonstrate that maximum stress was on the neck of the implant abutment. Additionally, the neck of the implant abutment was the weak point. The stress distribution of the implant system decreases with the central axis of the implant. The stress distribution of implant system also presents decrease from neck of implant abutment to the top of the tooth. Analytical results for

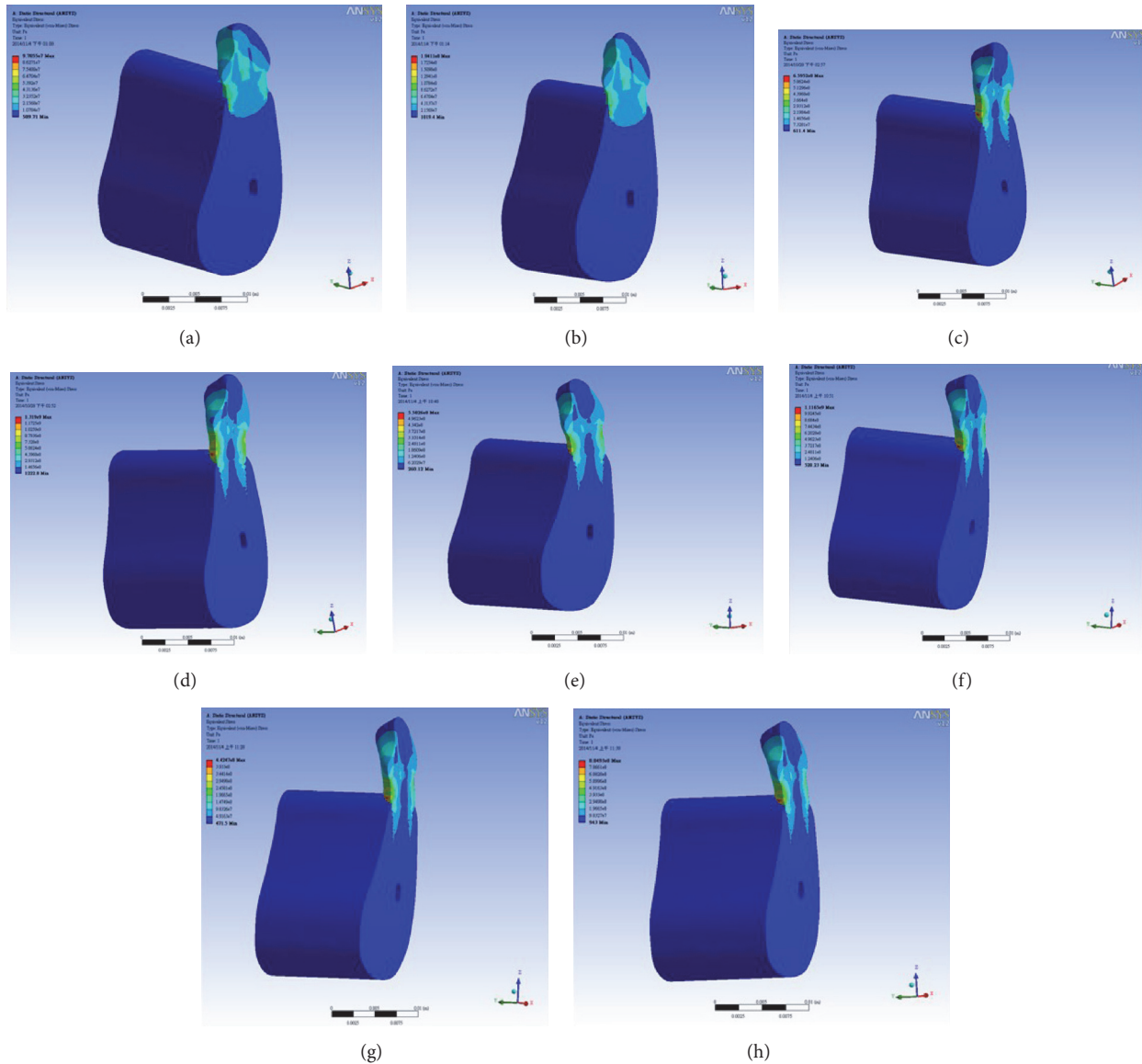


FIGURE 7: Stress distributions for various forces: (a) 500 N, vertical force; (b) 1000 N, vertical force; (c) 500 N, horizontal force; (d) 1000 N, horizontal force; (e) 500 N, oblique force (45°); (f) 1000 N, oblique force (45°); (g) 500 N, oblique force (60°); (h) 1000 N, oblique force (60°).

Figures 7(e) and 7(f) demonstrate that maximum stress was on the neck of the implant abutment. Additionally, the neck of the implant abutment was the weak point. The stress distribution of the implant system decreases with the central axis of the implant. The stress distribution of implant system also presents decrease from neck of implant abutment to the top of the tooth. Analytical results for Figures 7(g) and 7(h) indicate that maximum stress was on the abutment. A study goal was to identify the exact location of the implant abutment. Analytical results demonstrate that maximum stress was on the neck of the implant abutment. Additionally, the neck of the implant abutment was the weak point. The stress distribution of the implant system decreases with the central axis of the implant. The stress distribution of implant system also presents decrease from neck of implant abutment to the top of the tooth.

Figure 8(a) reveals the maximum deformation of implant system on different bite forces (various values). The deformation of the implant system has the maximum value by horizontal force; then it is by oblique force 30° , 45° , and 60° , and it by vertical force earns the minimum value. The maximum value of deformation increases as the bite force increases. Figure 8(b) reveals the maximum stress of implant system on different bite forces (various values). The maximum stress value of the implant system occurs by horizontal force; then it is by oblique force 30° , 45° , and 60° ; and stress by vertical force earns the minimum value. The reason is that horizontal force can generate a larger moment than other loading on the neck of the implant abutment. Vertical force acts directly on the abutment of implant. This phenomenon gets smaller moment on the implant abutment. The maximum value of stress increases as the bite force increases.

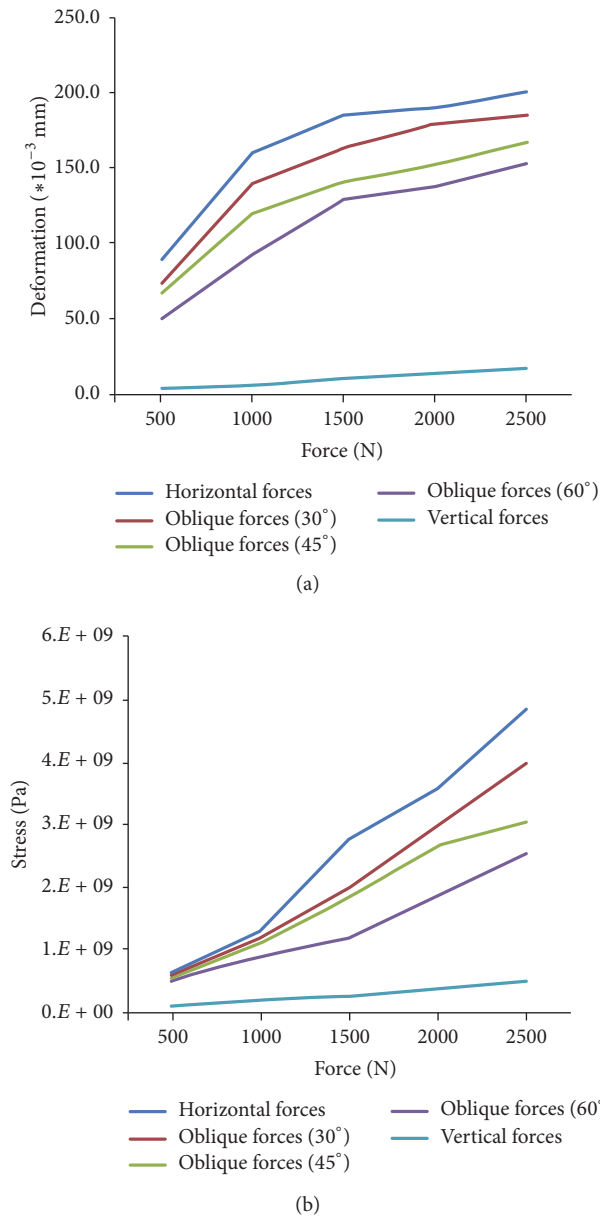


FIGURE 8: Maximum deformation and stress value on various bite forces: (a) deformation and (b) stress.

4. Conclusions

The deformation of the implant system has the maximum value by horizontal force, then it is by oblique force 30°, 45°, and 60°; and it by vertical force gets the minimum value. The maximum stress value of the implant system occurs by horizontal force; then it is by oblique force 30°, 45°, and 60° and stress by vertical force gets the minimum value. The deformation and stress distribution by molar force (horizontal force) show the maximum value for dental implant system. The molar force for the patient is key factor after dental implantation clinic. The results also show that the distribution of deformation and stress increases as the bite force increases. This study shows the neck of the implant

system is the weak point as the bite forces come from the human being.

Conflicts of Interest

The authors declare that they have no conflicts of interest.

References

- [1] A. Sethi, T. Kaus, and P. Scohor, "The use of angulated abutments in implant dentistry: five year clinical results of an ongoing prospective study," *International Journal of Oral and Maxillofacial Implants*, vol. 15, no. 6, pp. 801–810, 2000.
- [2] I. Akpınar, F. Demirel, L. Parnas, and S. Sahin, "A comparison of stress and strain distribution characteristics of two different rigid implant designs for distal-extension fixed prostheses," *Quintessence International*, vol. 27, no. 1, pp. 11–17, 1996.
- [3] H. W. Anselm Wiskott and U. C. Belser, "Lack of integration of smooth titanium surfaces: a working hypothesis based on strains generated in the surrounding bone," *Clinical Oral Implants Research*, vol. 10, no. 6, pp. 429–444, 1999.
- [4] D. R. Carter, M. C. Van der Meulen, and G. S. Beaupre, "Mechanical factors in bone growth and development," *Bone*, vol. 18, no. 1, supplement 1, pp. S5–S10, 1996.
- [5] A. Kashi, A. R. Chowdhury, and S. Saha, "Finite element analysis of a TMJ implant," *Journal of Dental Research*, vol. 89, no. 3, pp. 241–245, 2010.
- [6] H. Van Oosterwyck, J. Duyck, J. Vander Sloten, G. Van Der Perre, and I. Naert, "Peri-implant bone tissue strains in cases of dehiscence: a finite element study," *Clinical Oral Implants Research*, vol. 13, no. 3, pp. 327–333, 2002.
- [7] S. Faegh and S. Muftu, "Load transfer along the bone-dental implant interface," *Journal of Biomechanics*, vol. 43, no. 9, pp. 1761–1770, 2010.
- [8] D. H. Detolla, S. Andreana, A. Patra, R. Buhite, and B. Comella, "Role of the finite element model in dental implants," *The Journal of Oral Implantology*, vol. 26, no. 2, pp. 77–81, 2000.
- [9] G. Menicucci, A. Mossolov, M. Mozzati, M. Lorenzetti, and G. Preti, "Tooth-implant connection: some biomechanical aspects based on finite element analyses," *Clinical Oral Implants Research*, vol. 13, no. 3, pp. 334–341, 2002.
- [10] S. Tada, R. Stegaroiu, E. Kitamura, O. Miyakawa, and H. Kusakari, "Influence of implant design and bone quality on stress/strain distribution in bone around implants: a 3-dimensional finite element analysis," *International Journal of Oral and Maxillofacial Implants*, vol. 18, pp. 357–368, 2003.
- [11] J. P. Geng, K. B. Tan, and G. R. Liu, "Application of finite element analysis in implant dentistry: a review of the literature," *The Journal of Prosthetic Dentistry*, vol. 85, pp. 585–598, 2001.
- [12] W. Xu, J. H. Wang, J. Geng, and H. M. Huang, "Application of commercial FEA software," in *Application of the Finite Element Method in Implant Density*, pp. 92–126, Springer, 2008.

Research Article

Surface Treatment on Physical Properties and Biocompatibility of Orthodontic Power Chains

H. C. Cheng,^{1,2} M. S. Chen,^{2,3} B. Y. Peng,^{1,2} W. T. Lin,¹ Y. K. Shen,⁴ and Y. H. Wang⁵

¹*School of Dentistry, College of Oral Medicine, Taipei Medical University, Taipei, Taiwan*

²*Department of Dentistry, Taipei Medical University Hospital, Taipei, Taiwan*

³*School of Oral Hygiene, College of Oral Medicine, Taipei Medical University, Taipei, Taiwan*

⁴*School of Dental Technology, College of Oral Medicine, Taipei Medical University, Taipei, Taiwan*

⁵*Department of Mechanical Engineering, National Taiwan University of Science and Technology, Taipei, Taiwan*

Correspondence should be addressed to Y. K. Shen; ykshen@tmu.edu.tw

Received 13 January 2017; Accepted 19 February 2017; Published 30 April 2017

Academic Editor: Ren-Yeong Huang

Copyright © 2017 H. C. Cheng et al. This is an open access article distributed under the Creative Commons Attribution License, which permits unrestricted use, distribution, and reproduction in any medium, provided the original work is properly cited.

The conventional orthodontic power chain, often composed of polymer materials, has drawbacks such as a reduction of elasticity owing to water absorption as well as surface discoloration and staining resulting from food or beverages consumed by the patient. The goal of this study was to develop a surface treatment (nanoimprinting) for orthodontic power chains and to alleviate their shortcomings. A concave template (anodic alumina) was manufactured by anodization process using pure aluminum substrate by employing the nanoimprinting process. Convex nanopillars were fabricated on the surface of orthodontic power chains, resulting in surface treatment. Distinct parameters of the nanoimprinting process (e.g., imprinting temperature, imprinting pressure, imprinting time, and demolding temperature) were used to fabricate nanopillars on the surface of orthodontic power chains. The results of this study showed that the contact angle of the power chains became larger after surface treatment. In addition, the power chains changed from hydrophilic to hydrophobic. The power chain before surface treatment without water absorption had a water absorption rate of approximately 4%, whereas a modified chain had a water absorption rate of approximately 2%–4%. Furthermore, the color adhesion of the orthodontic power chains after surface modification was less than that before surface modification.

1. Introduction

Orthodontic power chains have been widely used in clinical orthodontic treatment since the 1960s [1] and are the most commonly used instrument for moving teeth. They are primarily composed of polyesters or polyethers formed through the polymerization of rubbers with multiple molecular structures connected by a series of urethane bonds [–(NH)–(CO)–O–] [2]. In clinical orthodontic treatment, the highly flexible nature of orthodontic power chains facilitates closing extraction spaces and adjusting the gear shaft angle [3]. Orthodontic power chains have many clinical advantages. Specifically, they are economic, are both easy to use and easy to adjust to the patient's needs, and provide light, continuous, and powerful assistance in appropriate tooth movement. However, because of the natural instability of the rubber, they are susceptible to the effects of changes in their surrounding

environment. Therefore, the shape and size of orthodontic force affect the efficiency of orthodontic treatment.

The impact strength of orthodontic power chains is affected by intrinsic factors such as the material composition, production methods, and external morphology [4, 5] and external environmental factors such as temperature, ambient pH, and moisture absorption levels. These factors all require correction of the power chains so that they can maintain strength and provide permanent deformation. In particular, because the oral cavity environment is extremely humid and prone to dramatic changes in temperature, it is difficult for corrective rubber chains to provide a continuous and stable force, preventing orthodontists from accurately measuring the force exerted on the teeth and in turn causing the number of patients returning to the clinic to increase [6]. Because water molecules are plasticizers, they weaken the interaction between molecules, resulting in chemical degradation [7].

Immersing a rubber chain in water for 7 days revealed that ester and ether molecules were leached because hydrolysis destroyed the backbone of the molecular chains [8].

Anodic aluminum oxide (AAO) films were fabricated through anodization of pure aluminum (Al) in suitable electrolytic solutions. These AAO films were manufactured with many nanopores, and the pore diameter and cell size, measured as the distance between the centers of two neighboring pores, were controlled by applying a pore-widening treatment, in which pores were etched chemically [9, 10]. Many researchers have achieved patterning using a nanoporous AAO membrane as a mask on injection molding or imprinting, using cycloolefin copolymer (COC) and polyvinyl chloride (PVC) as molded materials. The contact angles of smooth surfaces of COC and PVC were about 89° – 90° . The contact angles of microbumps and nanopillars (COC) were 120° – 140° . The surface of COC material on which the nanostructures were superimposed on the microstructures appeared hydrophobic [11]. Anodization yielded porous metallic membranes on nanoimprinting. Tapered holes were manufactured through repeated anodization by a pore-widening method. A polymer surface was then achieved by filling the tapered holes. This polymer with this unique surface geometry had antireflective properties [12].

Many microplastic imprinting processes can be applied to micropatterns including microdispensing combined with a hot imprinting process [13], UV molding [14], hybrid extrusion rolling imprinting [15], gas-assisted imprinting [16], and microelectrical discharge machining combined with a hot imprinting process [17, 18]. The nanoimprinting process has attracted attention from fabricating because it is applied to mass-produce nanostructure products at low costs and high production rates.

The target of this study was to identify an effective and rapid mass-production method on the surface treatment of orthodontic power chains. In this study, a concave, nanoporous AAO film was adopted as a template for nanoimprinting to fabricate on an orthodontic power chain with a convex nanopillar. The objective of this study was to improve the surface properties and reduce water absorption and color stains on the orthodontic power chain.

2. Experimental

2.1. AAO Template Fabrication. An AAO template (concave) with localized conical pores was fabricated through repeated anodization and pore-widening method, among which the two anodization procedures were alternated. Each anodization step was kept short to fabricate cones with low aspect ratios (cone height eliminated by base diameter of cone). A conical AAO template with a low aspect ratio was to manufacture some functional nanomaterials. This template can be applied in electrochemical deposition, sol-gel dipping, or an evaporation process. The low aspect ratio of pores causes simple material deposition. The materials tend to be deposited at the pore's top, such that the pore's bottom is not filled. This problem is exacerbated as the pore's aspect ratio increases. A 99.99% pure aluminum film ($100 \times 20 \times 10 \text{ mm}^3$; Wako Pure Chemical Industry, Ltd., Taiwan)

was electrochemically polished in a solution of 60% HClO_4 and 95% $\text{C}_2\text{H}_5\text{OH}$ at a ratio of 1:4. This film was cleaned by ethanol and pure water and then took advantage of manufacturing the conical AAO template. The film and a carbon electrode acted as the anode and cathode, respectively. The aluminum was anodized at 60 V in a 0.3 M oxalic acid solution at 20°C . To manufacture the AAO template, anodization for 1 h was used to produce a hexagonally ordered pore array. The AAO template was dissolved in a solution of 1.5 wt% chromic acid and 6 vol% phosphoric acid. To manufacture conical pores in this template, anodization and pore-widening treatments were alternated. The template was then anodized employing the same solution and voltage to fabricate uniformly sized pores. The pores were then widened through chemical etching, and the template was once again anodized under the same anodization operating conditions. At this time, the pores formed the taper; the interior of each pore comprised a two-step structure. To obtain the desired inverted conical structure, each step was fulfilled twice in the anodization and pore-widening process. Each anodization step was conducted at temperature of 9°C and voltage of 60 V in the same solution. The anodization time was 25 seconds in the first step and 20 seconds in each subsequent step. During the pore-widening treatment, the specimen was dipped in a 5 vol% phosphoric acid solution at 30°C for 12 minutes. The experimental results showed that the mean diameter of the nanoholes of the AAO was 200 nm at a voltage of 60 V for anodized oxidation.

2.2. Scanning Electron Microscopy and Atomic Force Microscopy for AAO. The specimen morphology was viewed by the way of field emission scanning electron microscopy (SEM) (JSM-6700F; JOEL, Japan). Cross sections of the AAO templates were intended by bending the aluminum until the template fractured. The AAO specimen was coated with platinum through sputtering prior to observations. The detailed morphology of specimen was observed utilizing atomic force microscopy (AFM) (Nanosurf Mobile S; Swiss). Prior to replication, the AAO template self-assembled to comprise an antiadhesive monolayer (1H, 1H, 2H, and 2H-perfluorodecyltrichlorosilane) through vapor phase deposition and minimize the surface energy of AAO template, the latter of which is required for easy demolding of the power chain from the AAO template.

2.3. Nanoimprinting on Power Chains. After the AAO template was fabricated, a nanoimprinting machine (NIL-3.0 Imprinter; Obduct AB, Sweden) fulfilled imprinting. Figure 1 indicates the process from AAO template fabrication to nanopillar fabrication of power chain. Elastomeric power chains (3M Alastik Chain, Dyna-link elastomeric chain) were applied as molded materials during nanoimprinting (Figure 2). The 3M Alastik chain was transparent and the Dyna-link chain was gray. A differential scanning calorimeter (DSC, DSC 400, Perkin Elmer) was applied to measure the glass transition temperatures of the elastomeric power chains. The results revealed that the glass transition temperature was 162.78°C for the 3M Alastik chain and 164.95°C for the Dyna-link chain (Figure 3). These results facilitated setting

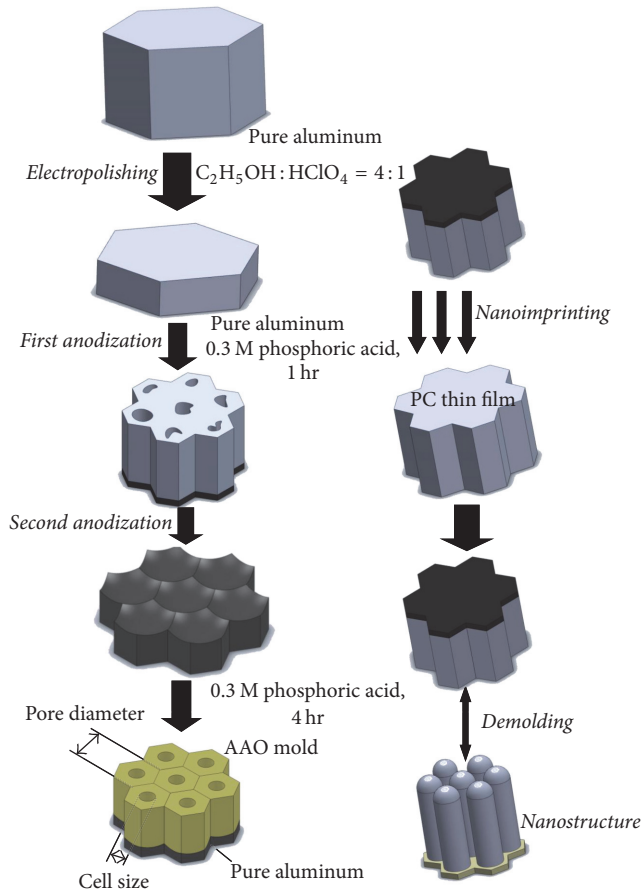


FIGURE 1: Complete process for AAO template fabrication and nanoimprinting.

TABLE 1: Levels of processing parameters for nanoimprinting.

Condition	Parameter			
	Imprinting temp. (°C)	Demolding temp. (°C)	Imprinting time (s)	Imprinting press. (bar)
A	155	50	180	50
B	160	50	180	50
C	165	50	180	50
D	170	50	180	50

the parameters on the nanoimprinting process, namely, the imprinting temperature, pressure, time, and demolding temperature (Table 1).

2.4. Surface Properties of Power Chains. A contact angle meter (DGD-DI; Digidrop Ltd., France) was applied to measure the contact angle of the orthodontic power chains before and after surface treatment. Each specimen was measured at 5 points. Deionized (DI) water in 0.5 μL drops was administered on the sample surface. Subject to a drop in solid/gas/liquid 3-state stability, computer-controlled photography (25/s) was applied to capture images and convert the image files. Measured contact angle data were obtained and plotted in charts. Water absorption necessitates correction

of power chains. Consequently, the performance of the nanoimprinted power chains after absorption correction was measured. The power chains were corrected using a vacuum oven at 60°C and immersed in water for three days. The power chains were then weighed (W_{dry}) and placed in 37 ± 2°C DI water for one day. Finally, they were removed and weighed (W_{wet}) to calculate the absorption rate

$$\text{Moisture} = \frac{(W_{wet} - W_{dry})}{W_{dry}} \times 100\% \quad (1)$$

The degree of staining was observed on this study. Experiments proceeded as follows:

- (1) The sample was placed in a vacuum oven at 60°C and immersed in water for three days.
- (2) The sample was then placed in 37°C test liquid (e.g., red ink, soy sauce).
- (3) After two days, the sample was washed with distilled water for one minute, and a digital camera was used to take pictures to visually compare staining and each imprinting parameter of five samples.

2.5. Statistics. In this study, measured data were subjected to statistical analysis. For any given experiment, each data point represented the mean ± standard deviation (SD) of six individual experiments. The *t*-test was used to determine significance between groups in the contact angle. Statistical significance was revealed by **p* < 0.05, ***p* < 0.01.

3. Results and Discussion

3.1. Nanoholes of AAO. Figure 4 reveals the nanoholes in the AAO template observed by SEM and AFM. The mean diameter of the nanoholes in the AAO was 200 nm. The nanoholes in the sample were of 24,000 nm depth. The results showed that the shape of the nanoholes was favorable for anodization and demonstrated that the nanoholes had a high aspect ratio of 120. According to SEM observation, the power chain had a smooth surface with no distinct structure (Figure 5).

3.2. Nanostructure of the Power Chains. Figure 6 shows the nanostructure, containing convex nanopillars, of orthodontic power chains by applying the AAO template in nanoimprinting. Nanoimprinting fabricated favorable nanopillar shapes (Figure 6). The effects of nanoimprinting parameters on the surface properties of the different orthodontic power chains with and without nanopillars are discussed as follows. The power chain surface properties formed under processing condition A (an imprinting temperature of 155°C, an imprinting pressure of 50 bar, an imprinting time of 180 s, and a demolding temperature of 50°C) were observed using SEM at 5000-fold magnification. The fibrous nanostructures generated had incomplete forms, with their surfaces being homogeneous, their fibrous structures mixed, and the columnar nanopillars produced not evenly distributed (Figure 6(a)). Under 8000-fold magnification, then the rod fibers were more clearly observed, being shorter than those



FIGURE 2: Orthodontic power chains. (a) 3M Alastik chain, (b) Dyna-link chain.

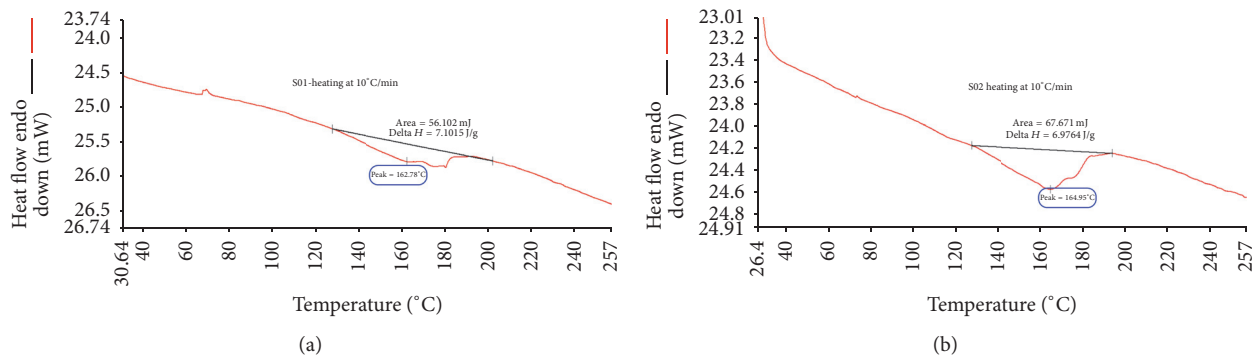


FIGURE 3: Glass transition temperatures of different power chains. (a) 3M Alastik chain, (b) Dyna-link chain.

observed under condition A and of different heights and shapes, with longer nanorods sticking to each other at their tops. The surface properties of power chain formed under processing condition B (an imprinting temperature of 160°C, an imprinting pressure of 50 bar, an imprinting time of 180 s, and a demolding temperature of 50°C), applied in the manufacturing process, were observed by SEM at 5000-fold magnification. The formation of more completely uniform nanopillar columns was found, with the embossing height being higher than that for condition A. In addition, although a few of the top beam nanopillar columns adhered to each other, they still maintained a basic columnar structure and did not agglomerate into a sheet (Figure 6(b)).

3.3. Influence of Nanoimprinting Conditions on Nanostructure of Power Chain. According to observation under 8000-fold magnification and measurement of the nanopillar column diameter and height, this group of processing parameters yielded the most complete three-dimensional nanopillar column structures. The contact angles of the hydrophobic

optimal set of parameter settings are used under the same condition; therefore, we applied it to measure the proportion of nanopillar columns with a diameter of approximately 440.43 nm, a height of approximately 7.88 μm , and a diameter-to-height ratio of 1:17.89. A high diameter-to-height ratio results in a nanopillar column with a Van der Waals force vulnerable to the impact caused by columns adhering to each other, thus reducing the surface modification effectiveness (Figure 6(b)). The surface properties of power chain under processing condition C (an imprinting temperature of 165°C, an imprinting pressure of 50 bar, an imprinting time of 180 s, and a demolding temperature of 50°C) were observed by SEM at 5000-fold magnification. Elongated nanopillar columns were found. The results found that the nanofiber columns were gradually sticky into flakes, losing the original three-dimensional columnar appearance. It is found that the contact angle value decreases under this process parameter (Figure 6(c)). The same set of parameters was still clearly observed by SEM at 8000-fold magnification, but the fibers became more slender, increasing the diameter

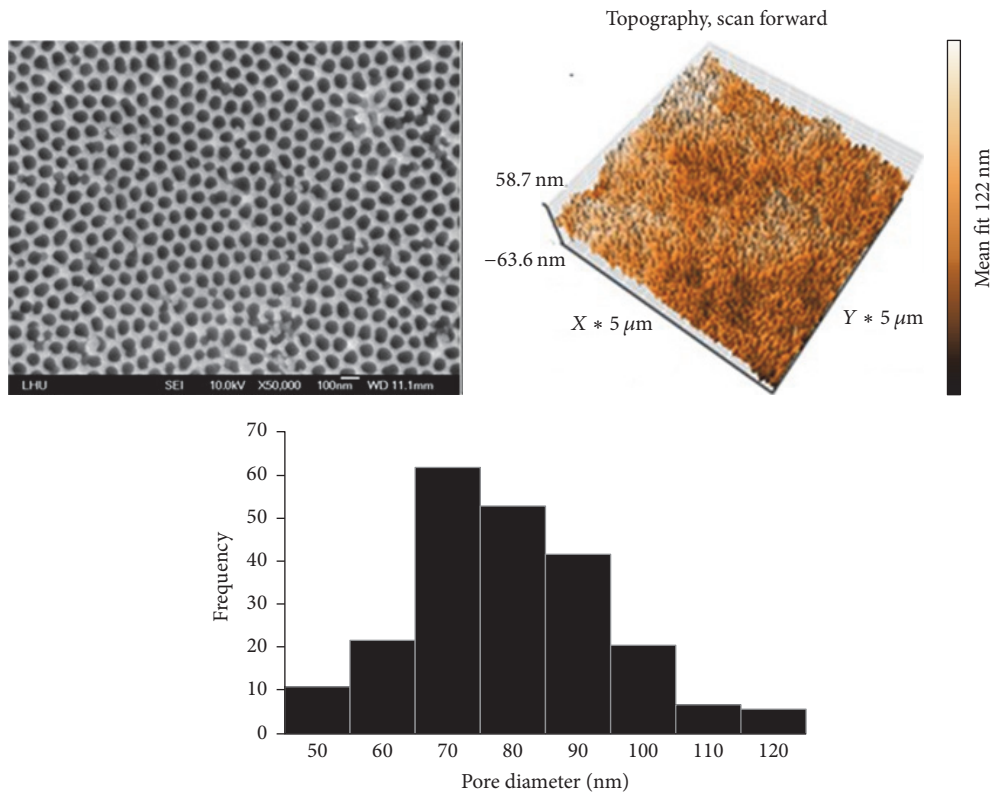


FIGURE 4: SEM images and surface roughness of the AAO ($\Phi = 100 \text{ nm}$, $R_a = 10.83 \text{ nm}$).

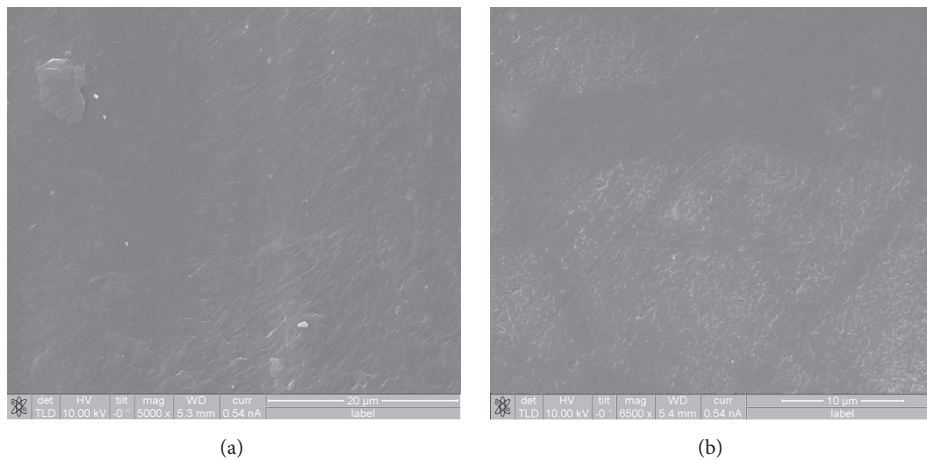
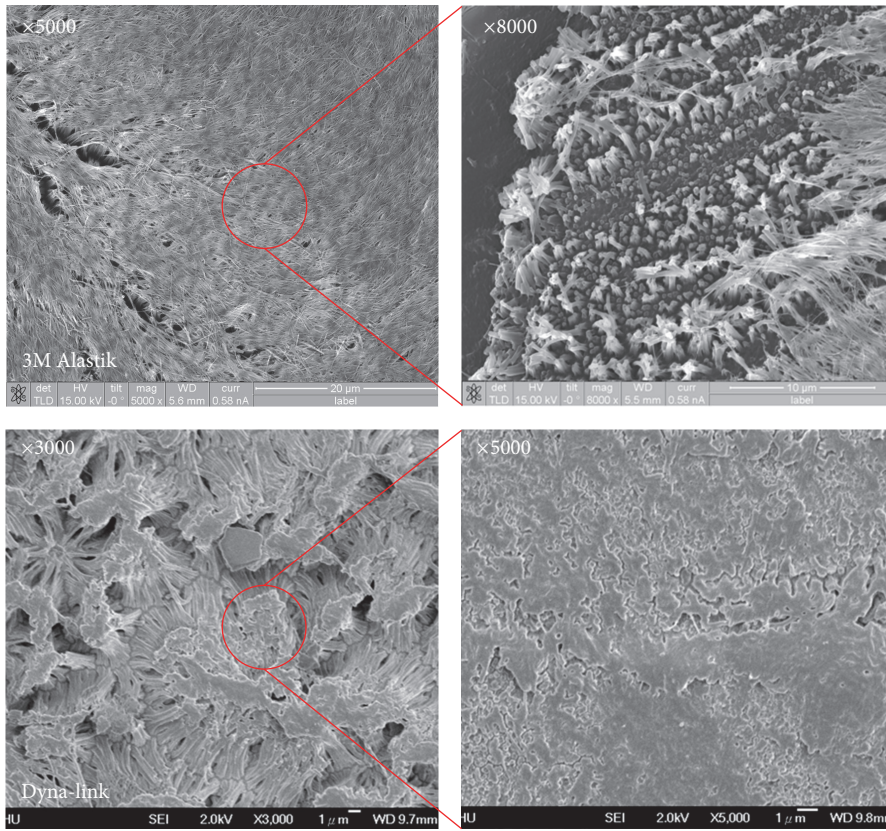


FIGURE 5: SEM images of different molded orthodontic power chains before nanoimprinting. (a) 3M Alastik chain, (b) Dyna-link chain.

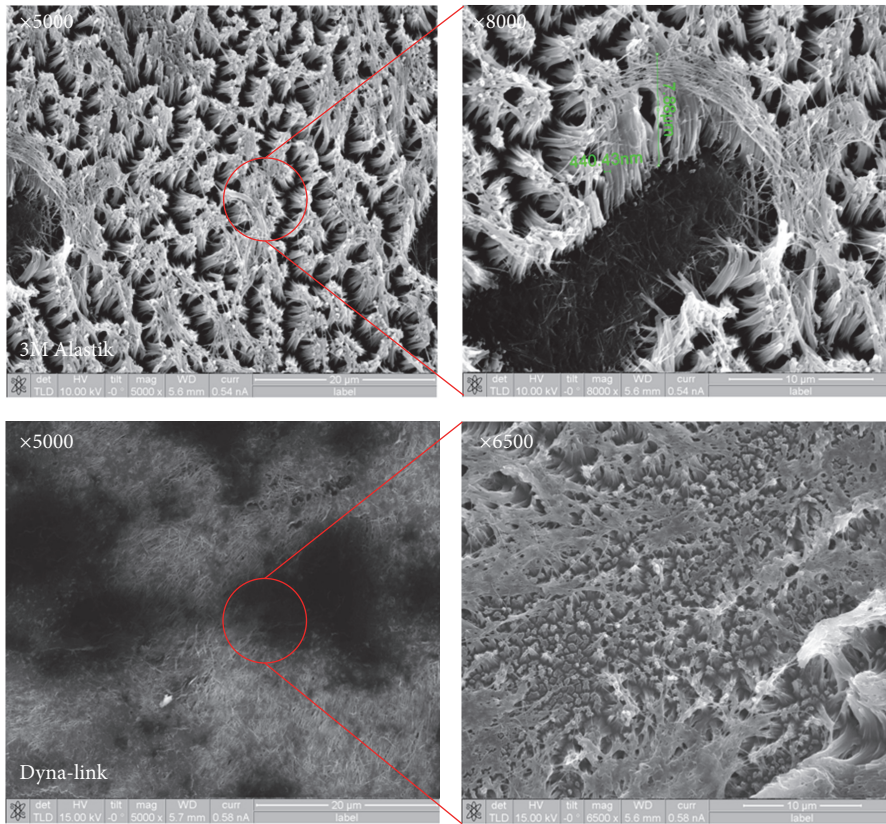
and height differences, and adhered to one another. The middle portion of vacancies was presumably caused by ejection defects (Figures 6(c) and 6(d)). According to SEM observation, stripping parameter settings have a substantial impact on results. As the temperature gradually exceeds the glass transition temperature of the sample, nanometer fiber columns easily agglomerate into a sheet. Improper stripping is likely to cause the entire film nanostructure to stall and the sample surface to become uneven, affecting the results of surface modification. The proposed technique provides effective demolding of the AAO template from the power

chain through the use of an antiadhesive monolayer coated on the AAO template.

3.4. Surface Properties of Power Chains. Figure 7 shows the contact angles of orthodontic power chains with and without nanopillar. The contact angles of power chains without surface modification were 67.4° (3M Alastik) and 66.2° (Dyna-link); these appear hydrophilic. Processing condition A entailed an imprinting temperature of 155°C ; an imprinting pressure of 50 bar; an imprinting time of 180 s; and a demolding temperature of 50°C ; the mean contact angles were



(a)



(b)

FIGURE 6: Continued.

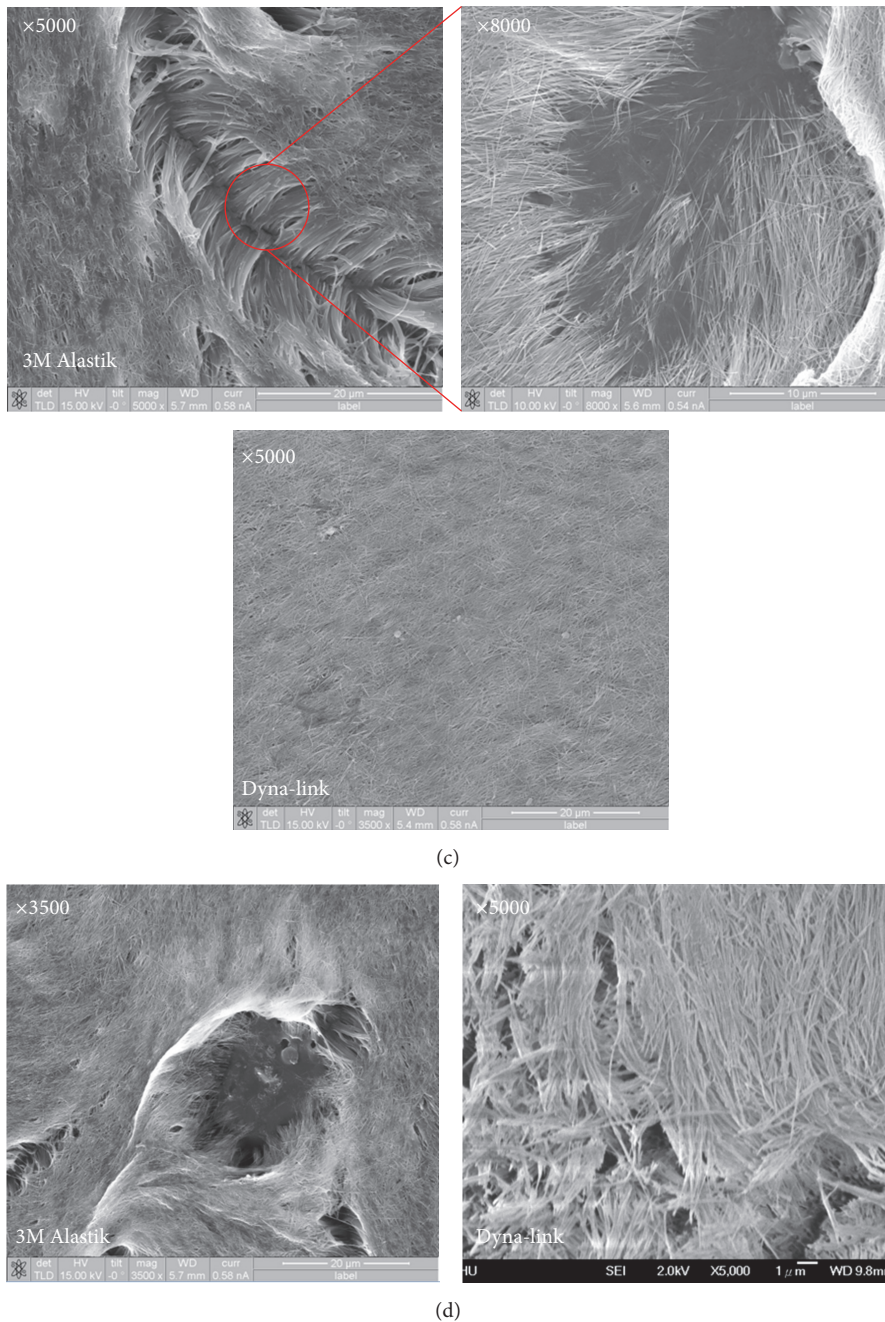


FIGURE 6: SEM images of nanopyllars of different molded orthodontic power chains for nanoimprinting using the AAO template. (a) Nanoimprinting with processing condition A. (b) Nanoimprinting with processing condition B. (c) Nanoimprinting with processing condition C. (d) Nanoimprinting with processing condition D.

77.36° (3M Alastik) and 80.13° (Dyna-link), indicating that the chains were hydrophilic. Processing condition B entailed an imprinting temperature of 160°C; an imprinting pressure of 50 bar; an imprinting time of 180 s; and a demolding temperature of 50°C; the mean contact angles were 101.69° (3M Alastik) and 92.83° (Dyna-link), indicating that the chains were hydrophobic. Processing condition C entailed an imprinting temperature of 165°C; an imprinting pressure

of 50 bar; an imprinting time of 180 s; and a demolding temperature of 50°C; the mean contact angles were 92.98° (3M Alastik) and 106.1° (Dyna-link), indicating that the chains were hydrophobic. Processing condition D comprised an imprinting temperature of 170°C; an imprinting pressure of 50 bar; an imprinting time of 180 s; and a demolding temperature of 50°C; the mean contact angles were 86.36° (3M Alastik) and 88.9° (Dyna-link), indicating that the chains

TABLE 2: Absorption rates of orthodontic power chains before and after surface treatment (3M Alastik/Dyna-link).

	Weight before absorbing water (g)	Weight after absorbing water (g)	Weight difference (g)	Water absorption rate (%)
No surface modification	0.005/0.004	0.0052/0.0042	0.0002/0.0002	4%/5%
A	0.0054/0.004	0.0056/0.0042	0.0002/0.0002	3.7%/5%
B	0.0051/0.0034	0.0052/0.0036	0.0001/0.0002	2%/4.4%
C	0.0047/0.0047	0.0049/0.0048	0.0002/0.0001	4.2%/2.1%
D	0.0049/0.0044	0.0051/0.0048	0.0002/0.0004	4%/5.5%

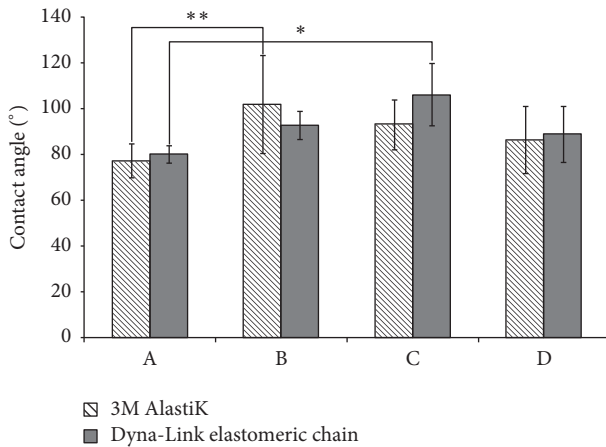


FIGURE 7: Contact angles of orthodontic power chains before and after surface treatment (values are the mean \pm SD of six experiments ($n = 6$), * $p < 0.05$, ** $p < 0.01$).

were hydrophilic. The contact angles indicate the statistically significant difference among processing conditions A and B for 3M Alastik power chain. The results also reveal the statistically significant difference between processing conditions A and C for Dyna-link power chain. Table 2 lists the absorbance rates of different orthodontic power chains after nanoimprinting. The weights of power chains were 0.005 g (3M Alastik) and 0.004 g (Dyna-link) before the nanoimprinting process without water absorption and were 0.0052 g (3M Alastik) and 0.0042 g (Dyna-link) before the nanoimprinting process with water absorption. The water absorption rates were 4% (3M Alastik) and 5% (Dyna-link). The weights of the power chains were 0.0054 g (3M Alastik) and 0.004 g (Dyna-link) under processing condition A without water absorption and 0.0056 g (3M Alastik) and 0.0042 g (Dyna-link) under the same processing condition with water absorption. The water absorption rates were 3.7% (3M Alastik) and 5% (Dyna-link). The power chain weights were 0.0051 g (3M Alastik) and 0.0034 g (Dyna-link) under processing condition B without water absorption and 0.0052 g (3M Alastik) and 0.0036 g (Dyna-link) under the same processing condition with water absorption. The water absorption rates were 2% (3M Alastik) and 4.4% (Dyna-link). The weights of the power chains were 0.0047 g (3M Alastik) and 0.0047 g (Dyna-link) without water absorption under processing condition C and 0.0049 g (3M Alastik) and

0.0048 g (Dyna-link) with water absorption under the same processing condition. The absorption rates were 4.2% (3M Alastik) and 2.1% (Dyna-link). The weights of the power chains were 0.0049 g (3M Alastik) and 0.0044 g (Dyna-link) without water absorption under processing condition D and 0.0051 g (3M Alastik) and 0.0048 g (Dyna-link) with water absorption under the same processing condition. The absorption rates were 4% (3M Alastik) and 5.5% (Dyna-link).

3.5. Dyeing Tests of Power Chains. Figure 8 indicates the results of dyeing tests for orthodontic power chains (Figure 8). Because the Dyna-link elastomeric chain was gray and would not properly exhibit staining test results, we used only the 3M Alastik power chain for the dye tests. The specimens were dipped in red ink dye for 48 hours and are ranked from lowest to highest according to the staining depth, as determined by the naked eye, as follows: $B < C < D = A$. Differences among the other 4 groups are difficult to compare, but the naked eye falls on the color depth of the C and D specimens. The staining test results were generally in line with the contact angle measurements; however, accurate results regarding the color effect can be obtained by using a prolonged staining time and relevant computer equipment for further analysis.

4. Conclusions

In this study, an AAO template was applied as a mold insert for fabricating the nanostructures on orthodontic power chains by nanoimprinting. Experimental results revealed that the contact angle of the orthodontic power chains increased from approximately 80° to 130° . In addition, the surface property of power chain changed from hydrophilic to hydrophobic, and its absorption rate decreased after surface modification. In this investigation, nanopillars formed on the orthodontic power chains, and the power chain surface was modified using a high-speed mass-production process.

Conflicts of Interest

The authors declare that they have no conflicts of interest.

Authors' Contributions

H. C. Cheng contributed to the study conception, data analysis, and interpretation and critically revised the manuscript; W. T. Lin contributed to the analysis of the physical properties

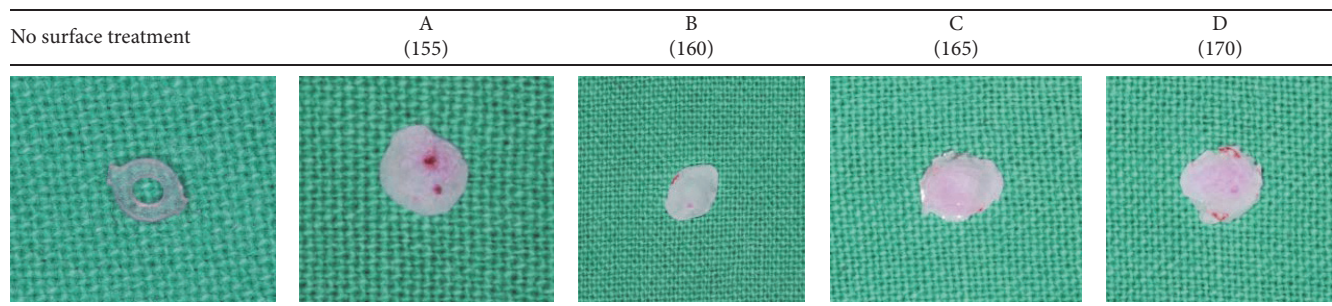


FIGURE 8: Dyeing test for orthodontic power chain (3M Alastik chain).

of the orthodontic power chains after nanoimprinting; Y. K. Shen contributed to data acquisition, analysis, and interpretation and drafted the manuscript; M. S. Chen and B. Y. Peng contributed to AAO fabrication and the nanoimprinting process on the orthodontic power chains. All authors provided final approval and agree to be accountable for all aspects of the work.

Acknowledgments

The authors thank the National Science Council, Taiwan, for financially supporting this research under Contract no. NSC 102-2314-B-038-016.

References

- [1] D. L. Baty, D. J. Storie, and J. A. von Fraunhofer, "Synthetic elastomeric chains: a literature review," *American Journal of Orthodontics and Dentofacial Orthopedics*, vol. 105, no. 6, pp. 536–542, 1994.
- [2] F. W. Billmeyer Jr., "Thermosetting resins," in *Textbook of Polymer Science*, John Wiley & Sons, New York, NY, USA, 3rd edition, 1984.
- [3] Y.-C. Park, Y.-J. Choi, N.-C. Choi, and J.-S. Lee, "Esthetic segmental retraction of maxillary anterior teeth with a palatal appliance and orthodontic mini-implants," *American Journal of Orthodontics and Dentofacial Orthopedics*, vol. 131, no. 4, pp. 537–544, 2007.
- [4] J. P. Ferriter, C. E. Meyers Jr., and L. Lorton, "The effect of hydrogen ion concentration on the force-degradation rate of orthodontic polyurethane chain elastics," *American Journal of Orthodontics and Dentofacial Orthopedics*, vol. 98, no. 5, pp. 404–410, 1990.
- [5] T. Eliades, G. Eliades, and D. C. Watts, "Structural conformation of in vitro and in vivo aged orthodontic elastomeric modules," *The European Journal of Orthodontics*, vol. 21, no. 6, pp. 649–658, 1999.
- [6] D. G. Brooks and H. G. Hershey, "Effects of heat and time on stretched plastic orthodontic modules," *Journal of Dental Research*, vol. 55, p. 363, 1976.
- [7] E. F. Huguet, K. S. Patrick, and L. J. Nunez, "Observations on the elastic behavior of a synthetic orthodontic elastomer," *Journal of Dental Research*, vol. 69, no. 2, pp. 496–501, 1990.
- [8] C. S. Schollenberger and F. D. Stewart, "Thermoplastic polyurethane hydrolysis stability," *Journal of Elastomers and Plastics*, vol. 3, no. 1, pp. 28–56, 1971.
- [9] J. H. Yuan, F. Y. He, D. C. Sun, and X. H. Xia, "A simple method for preparation of through-hole porous anodic alumina membrane," *Chemistry of Materials*, vol. 16, no. 10, pp. 1841–1844, 2004.
- [10] X. Wang and G. R. Han, "Fabrication and characterization of anodic aluminum oxide template," *Microelectronic Engineering*, vol. 66, no. 1–4, pp. 166–170, 2003.
- [11] H.-K. Koponen, I. Saarikoski, T. Korhonen et al., "Modification of cycloolefin copolymer and poly(vinyl chloride) surfaces by superimposition of nano- and microstructures," *Applied Surface Science*, vol. 253, no. 12, pp. 5208–5213, 2007.
- [12] H. Masuda, "Highly ordered nanohole arrays in anodic porous alumina," in *Ordered Porous Nanostructures and Applications*, vol. 9 of *Nanostructure Science and Technology*, pp. 37–55, Springer, Berlin, Germany, 2005.
- [13] H.-C. Cheng, C.-H. Wang, C.-F. Huang et al., "Micro fabrication of microlens arrays by micro dispensing," *Polymers for Advanced Technologies*, vol. 21, no. 9, pp. 632–639, 2010.
- [14] S.-M. Kim and S. Kang, "Replication qualities and optical properties of UV-moulded microlens arrays," *Journal of Physics D: Applied Physics*, vol. 36, no. 20, pp. 2451–2456, 2003.
- [15] L.-T. Jiang, T.-C. Huang, C.-R. Chiu, C.-Y. Chang, and S.-Y. Yang, "Fabrication of plastic microlens arrays using hybrid extrusion rolling embossing with a metallic cylinder mold fabricated using dry film resist," *Optics Express*, vol. 15, no. 19, pp. 12088–12094, 2007.
- [16] T.-C. Huang, B.-D. Chan, J.-K. Ciou, and S.-Y. Yang, "Fabrication of microlens arrays using a CO₂-assisted embossing technique," *Journal of Micromechanics and Microengineering*, vol. 19, no. 1, Article ID 015018, 2009.
- [17] M.-S. Huang, Y.-C. Chiang, S.-C. Lin et al., "Fabrication of microfluidic chip using micro-hot embossing with micro electrical discharge machining mold," *Polymers for Advanced Technologies*, vol. 23, no. 1, pp. 57–64, 2012.
- [18] C.-F. Huang, H.-C. Cheng, Y. Lin, C.-W. Wu, and Y.-K. Shen, "Study on cellular behaviors on different nanostructures by nanoporous alumina template," *International Journal of Precision Engineering and Manufacturing*, vol. 15, no. 4, pp. 689–693, 2014.

Research Article

Collagen Sponge Functionalized with Chimeric Anti-BMP-2 Monoclonal Antibody Mediates Repair of Critical-Size Mandibular Continuity Defects in a Nonhuman Primate Model

Yilin Xie,^{1,2} Yingying Su,¹ Seiko Min,³ Jianxia Tang,⁴ Bee Tin Goh,⁵
Leonardo Saigo,⁵ Sahar Ansari,⁶ Alireza Moshaverinia,⁷ Chunmei Zhang,¹ Jinsong Wang,^{1,8}
Yi Liu,² Arash Khojasteh,⁹ Homayoun H. Zadeh,³ and Songlin Wang^{1,8}

¹Molecular Laboratory for Gene Therapy and Tooth Regeneration, Beijing Key Laboratory of Tooth Regeneration and Function Reconstruction, Capital Medical University School of Stomatology, Tian Tan Xi Li No. 4, Beijing 100050, China

²Laboratory of Tissue Regeneration and Immunology and Department of Periodontics, Beijing Key Laboratory of Tooth Regeneration and Function Reconstruction, Capital Medical University School of Stomatology, Tian Tan Xi Li No. 4, Beijing 100050, China

³Laboratory for Immunoregulation and Tissue Engineering (LITE), Ostrow School of Dentistry, University of Southern California, Los Angeles, CA, USA

⁴Department of Oral and Maxillofacial Surgery, Xiangya Stomatological Hospital, Central South University, Changsha, Hunan, China

⁵Department of Oral & Maxillofacial Surgery, National Dental Centre, Singapore

⁶Division of Growth and Development, School of Dentistry, University of California, Los Angeles, CA, USA

⁷Division of Advanced Prosthodontics, School of Dentistry, University of California, Los Angeles, CA, USA

⁸Department of Biochemistry and Molecular Biology, Capital Medical University School of Basic Medical Sciences, You An Men Wai Xi Tou Tiao No. 10, Beijing 100069, China

⁹Department of Tissue Engineering, School of Advanced Technologies in Medicine, Shahid Beheshti University of Medical Sciences, Tehran, Iran

Correspondence should be addressed to Homayoun H. Zadeh; zadeh@usc.edu

Received 24 October 2016; Revised 5 January 2017; Accepted 19 January 2017; Published 16 March 2017

Academic Editor: Matthew B. Wheeler

Copyright © 2017 Yilin Xie et al. This is an open access article distributed under the Creative Commons Attribution License, which permits unrestricted use, distribution, and reproduction in any medium, provided the original work is properly cited.

Antibody-mediated osseous regeneration (AMOR) has been introduced by our research group as a tissue engineering approach to capture of endogenous growth factors through the application of specific monoclonal antibodies (mAbs) immobilized on a scaffold. Specifically, anti-Bone Morphogenetic Protein- (BMP-) 2 mAbs have been demonstrated to be efficacious in mediating bone repair in a number of bone defects. The present study sought to investigate the application of AMOR for repair of mandibular continuity defect in nonhuman primates. Critical-sized mandibular continuity defects were created in *Macaca fascicularis* locally implanted with absorbable collagen sponges (ACS) functionalized with chimeric anti-BMP-2 mAb or isotype control mAb. 2D and 3D analysis of cone beam computed tomography (CBCT) imaging demonstrated increased bone density and volume observed within mandibular continuity defects implanted with collagen scaffolds functionalized with anti-BMP-2 mAb, compared with isotype-matched control mAb. Both CBCT imaging and histologic examination demonstrated de novo bone formation that was in direct apposition to the margins of the resected bone. It is hypothesized that bone injury may be necessary for AMOR. This is evidenced by de novo bone formation adjacent to resected bone margins, which may be the source of endogenous BMPs captured by anti-BMP-2 mAb, in turn mediating bone repair.

1. Introduction

Loss of mandibular bone due to congenital anomalies, trauma, infection, or tumor resection surgeries is a challenging clinical problem for reconstruction. Current methods for repair or regeneration include autologous bone grafting, allogenic bone grafting, and tissue engineering [1–3]. For several decades, the most widely used procedures to promote healing of bone fractures and large defects utilized autologous or allogenic bone grafts [1]. However, the use of these materials has a number of drawbacks including potential host reaction, limited donor tissue availability, donor-site morbidity, and potential disease transmission from allografts [4]. An alternative to bone grafts is bone tissue engineering. Tissue engineering entails the application of progenitor cells and/or growth factors delivered to the treatment site on an acellular scaffold. It is well known that bone tissue engineering is partially regulated by the host local microenvironment, including the presence of signaling molecules and host immune cells [5–7]. Bone Morphogenetic Proteins (BMPs) are potential osteoinductive growth factors that play a critical role in bone regeneration and repair [8]. It is well known that exogenous administration of recombinant human (rh) BMP-2 can initiate a healing cascade that mediates bone regeneration through the TGF- β /BMP signaling pathway [8]. Owing to their substantial osteogenic properties, the US Food and Drug Administration (FDA) had approved rhBMP-2 and rhBMP-7 for clinical use [9, 10]. However, application of exogenous growth factors also has a number of drawbacks, including serious adverse effects which are occasionally fatal; moreover, recombinant growth factors have reduced biological activity, requiring high concentrations to be used in vivo and therefore are associated with high costs [5, 11–13]. These shortcomings have driven the quest for the development of alternative strategies. Our research group has introduced an alternative bone tissue engineering approach termed antibody-mediated osseous regeneration (AMOR). We have identified specific monoclonal antibody (mAb) clones directed against BMP-2 that have the ability to capture endogenous BMP-2 ligands and present them to progenitor cells, mediating in vivo tissue repair [14]. Ansari et al. reported that AMOR can be regulated through BMP signaling pathway [15]. In addition, it was confirmed that anti-BMP-2 mAb can trap and tether endogenous BMP-2 ligands for the directed osteodifferentiation of mesenchymal stem cells through in vitro and in vivo studies [16]. In previous studies, murine and chimeric anti-BMP-2 mAb has been used in mice, rat, and rabbit models and confirmed to be effective in promoting bone repair and regeneration through calvaria defect models [17–20]. However, there has been a need for more clinically relevant animal models. Specifically, more relevant animal models for craniofacial reconstructive surgeries are desired. Before a novel approach like this one can be introduced into a clinical trial, preclinical studies should be available in larger animal models that more closely mimic challenging human clinical skeletal defects. Therefore, in the present study, we investigated the ability of chimeric anti-BMP-2 mAb to mediate repair of a critical-size mandibular continuity defect in a nonhuman primate model.

2. Materials and Methods

2.1. Animals. All animal experiments were performed in accordance with a protocol approved by the Institutional Animal Care and Use Committee (IACUC) of the Capital Medical University, Beijing, China. Six adult male crab-eating macaques (*Macaca fascicularis*) aged 8–12 and weighing between 4.0 and 5.0 kg were included in this study. Three animals were assigned to experimental (AMOR) and 3 to control (isotype-matched mAb) groups. Before surgery, the animals were housed in individual cages with water and fed ad libitum.

2.2. Antibody. The hybridoma clone of a murine anti-BMP-2 mAb was expanded and used in order to generate chimeric anti-BMP-2 mAb according to procedures described by Ansari et al. [15]. Based on previous dose-response data, 25 μ g/mL was selected as the optimal dose of chimeric anti-BMP-2 mAb for all experiments [15, 18].

2.3. Scaffold Biomaterials. Chimeric anti-BMP-2 mAb (25 μ g/mL) and isotype control mAb (25 μ g/mL) were adsorbed on type 1 absorbable collagen sponge (ACS; CollaCote; Integra, Plainsboro, NJ, USA) as previously described [17]. Briefly, ACS was saturated in diluted mAb for one hour at room temperature prior to in vivo implantation.

2.4. Mandibular Defect Model. Six animals were randomly assigned into experimental or control groups. The three animals in the control group received ACS immobilized with isotype-matched control mAb and the three experimental animals received ACS immobilized with chimeric anti-BMP-2 mAb in their defects. Animals were sedated with subcutaneous injection of 5 mg/kg of ketamine (Jiangsu Hengrui Medicine Co., Ltd, Lianyungang, China). Anesthesia was achieved by veterinarian staff with IV Propofol (8 mg/kg; Diprivan, Astra Zeneca, London, England). Endotracheal intubation was performed using an oral-tracheal tube with a diameter of 3.5 mm (Sheridan™, Teleflex Medical, NC, USA). The anesthesia was maintained by IV Propofol (2.5 mg/kg) per 30~45 min. Local anesthesia was achieved by intramucosal injection of lidocaine with 1:100,000 epinephrine (Astra Zeneca, London, England) [21, 22]. Hair over the right mandibular region was shaved. The animals were swabbed periorally with 1% Cetrimide followed by 0.05% chlorhexidine gluconate solution. All surgical sites were washed with 0.12% chlorhexidine gluconate solution. In each animal, a 4 cm submandibular incision was made at 1 cm below the inferior border of the mandible, after which the platysma was identified and cut, taking care not to damage the mandibular branch of the facial nerve. The facial artery and vein were then identified, tied off, and ligated. The masseter muscle was then identified and dissected to reach the periosteal layer. The periosteum was incised and elevated to expose the mandible to the region of the first molar anteriorly and halfway up the ascending ramus posteriorly. Preoperative CBCT images were taken in order to aid with planning the segmental osteotomies (Figure 1(a)). Reconstruction plates

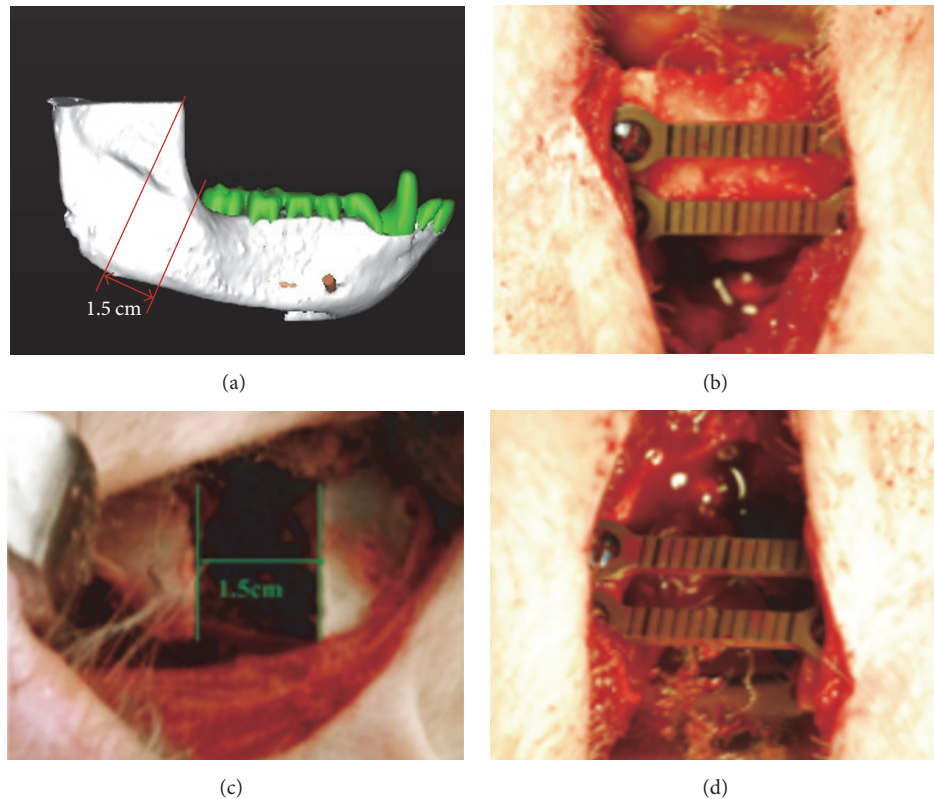


FIGURE 1: Representative clinical and 3D-rendered imaging volume of mandibular continuity defects. Preoperative CBCT images (a) were used to aid in planning of the segmental osteotomy, as well as in comparison with postsurgical images. Clinical view, showing the surgically exposed posterior mandible, where the reconstruction plates were provisionally attached to the mandible (b). This step defined the position of the titanium screws and reconstruction plates relative to the planned osteotomy to aid in orienting the segmented ends following resection back in correct position. Resected segmental osteotomy, creating a 1.5 cm continuity defect (c). Repositioned mandibular segments fixated with titanium reconstruction plates (d).

were provisionally attached to the mandible over the region planned for resection, prior to osteotomy (Figure 1(b)). This step defined the position of the titanium screws and reconstruction plates relative to the planned osteotomy to help with orienting the segmented ends, following resection back in correct position. A 1.5 cm wide segmental osteotomy of the mandible was performed on the right angle of mandible, using a rotary fissure bur under copious irrigation (Figure 1(c)). The mandibular segments were reoriented using the positions of the predrilled titanium screws as a guide. The segments were fixated with 2 titanium reconstruction plates using two titanium screws per plate (Figure 1(d)). ACS scaffold (4.0 cm × 2.0 cm × 3.0 mm), which was preincubated with anti-BMP-2 or isotype-matched control mAb, was placed within experimental or control transected defect sites, respectively. Since the scaffolds were spongy in consistency, once incubated with 100 μ L of anti-BMP-2 or isotype control mAb, they easily adapted to the confines of the defects. The incision was approximated primarily in layers using polyglactin sutures (Vicryl™, Ethicon Inc, Somerville, NJ, USA). The skin was covered with 3% tetracycline hydrochloride antibiotic ointment. Postoperative care

included analgesia by IM injection of Carprofen (2 mg/kg; Harbin Pharmaceutical Group, Co., Ltd, Harbin, China) for 3 days postoperatively. Animals were maintained on a soft diet for 2 weeks postoperatively. Oral hygiene measure consisted of spraying the teeth of animals with 0.2% chlorhexidine gluconate mouthwash (Etouch, Shandong, China) once a day.

2.5. Cone Beam Computed Tomography (CBCT) Image Analysis. Live animals were imaged with CBCT scanner (Kodak Medical Solutions Molecular Imaging, Knoxville, TN) with 60 μ m voxel size at 60 kV and 110 mA at three time points (preoperatively, as well as at 6 and 12 weeks postoperatively). The data were acquired in Digital Imaging and Communications in Medicine (DICOM) format. For two-dimensional analysis, DICOM files were imported into Simplant Pro 16.0 Software (Dentsply Implants, Waltham, MA, USA) for 2D and 3D image reconstruction and density analysis. The minimum threshold used for reconstruction of 3D volumes was set at 400 Hounsfield units (HU), based on the lowest density observed within control and experimental specimens. This threshold was used for all pre- and postoperative images at all time points. Pre- and postoperative (6 and 12 weeks after

surgery) CBCT images were examined for 2D quantitative analysis of de novo bone formation by density measurements within sections taken in axial planes. For analysis of axial images, 3 sections were taken at equal distances from the superior-most through inferior-most boundaries of the defects. The density measurements were performed, using rectangle density measurement tool in Simplant software in each of the sections, and the density was recorded in HU. Titanium plates were excluded from analysis of density.

3D image analysis was performed as previously described [22]. Briefly, DICOM files were imported into Mimics software (Materialise, Leuven, Belgium) to construct 3D volumes. The reconstructions of scanned images were thresholded to remove any soft tissue and cartilage, leaving only mineralized tissues, and sectioned to isolate the defect site. The 3D reconstructed volumes were exported in Stereolithography (STL) file format and imported into reverse engineering software (Geomagic Studio® v12.0 software, 3D SYSTEMS, Cary, NC, USA). Since file sizes were very large, slowing down analysis, once volumes were reconstructed, images were then trimmed in order to facilitate manipulations. Landmarks to define the boundaries of surgical defects were selected as 15 mm, based on titanium plates used as reference. The volumes present within confines of defects at 6 and 12 week postsurgical time points were quantified and expressed in mm³.

2.6. Histology and Histomorphometry. Twelve weeks after surgical procedure, the animals were euthanized. The specimens were fixed with 4% (v/v) paraformaldehyde for 24 hours at room temperature. Samples were then decalcified in ethylene diamine tetraacetic acid (EDTA) for 60 days. The samples were dehydrated in a graded ethanol series (70%, 95%, and 100%) and embedded in paraffin. The specimens were then serially sectioned (10 µm), deparaffinized, hydrated, and stained with Hematoxylin and Eosin (H&E). The stained sections were viewed under microscope (Olympus, Tokyo, Japan) at various magnifications and digital images were acquired. Quantitative histomorphometry was performed, using NIH Image J software (U.S. National Institutes of Health, Bethesda, Maryland, USA). Images taken at 40x were used for histomorphometry. Standardized nomenclature was used for defining various components of tissues within each viewed field [23]. Newly formed bone volume (BV) is defined as regions containing osteocytes within lacunae, the proportion of which was calculated relative to that of total tissue volume (TV).

2.7. Statistical Analysis of Data. Quantitative data were presented as mean ± standard deviation (SD). Comparisons between two groups were performed using two-tailed unpaired Student's *t*-tests. Differences were considered statistically significant at a *P* value < 0.05.

3. Results

3.1. Clinical Outcomes. All animals healed uneventfully without any adverse biologic complications. All surgical sites showed minimal inflammation and no signs of infection. Animals were euthanized at 12 weeks postsurgically.

3.2. Analysis of Mineralized Tissue Formation by CBCT. To investigate the ability of the mAb to repair large critical-size craniofacial defects, 15 mm continuity defects were surgically created in the posterior mandible and the two segments were rigidly fixated with titanium reconstruction plates (Figure 1). The 15 mm defect was filled with collagen scaffold functionalized with chimeric anti-BMP-2 mAb or isotype-matched control mAb. The areas were allowed to heal for 12 weeks. To investigate the kinetics of bone healing, serial CBCT imaging was conducted preoperatively as well as 6 and 12 weeks postoperatively. The CBCT images (Figure 2) were subjected to 2D and 3D quantitative analysis to determine the degree of bone healing within experimental and control defects at the two postoperative time points. The 2D CBCT images were examined in three discrete planes, that is, coronal, axial, and sagittal. Moreover, three different zones within each of the axial planes (superior, middle, and inferior) (Figure 2) were analyzed. Regions of interest were defined within coronal (anterior, middle, and posterior) and sagittal (anterior, middle, and posterior) planes (Supplemental Figure 1 in Supplementary Material available online at <https://doi.org/10.1155/2017/8094152>). The bone density within those defined regions is reported in Supplemental Table 1.

Results demonstrated that mandibular defects implanted with isotype-matched control mAb immobilized on collagen scaffold exhibited very low density with negative HU at 6 and 12 weeks postoperatively (Figure 3). In contrast, mandibular defects implanted with chimeric anti-BMP-2 mAb immobilized on collagen scaffold exhibited significantly higher density consistent with formation of mineralized tissue after 6 weeks, which increased by 12 weeks (Figure 3). Qualitative examination of 2D and 3D reconstructed images illustrated that new bone formation was observed at the margins of the defect adjacent to resected parent bone.

Next, 3D volumetric measurement was performed for tissues formed within surgical defects at 6 and 12 weeks postoperatively (Figure 4(a)). Results revealed increasing bone volume from 6 to 12 weeks in both experimentally treated or control-treated defects. At both 6 and 12 weeks, there was significantly more mineralized tissue volume, within defects treated with chimeric anti-BMP-2 mAb (Figure 4(b)).

3.3. Histologic and Histomorphometric Analysis. To examine the nature of biologic healing at the cellular level, qualitative histological examination was performed on the treated mandibles at 12 weeks postoperatively (Figure 5). Histological evaluation revealed the presence of mature lamellar bone containing osteocytes within lacunae within newly ossified tissues in defects implanted with ACS functionalized with anti-BMP-2 mAb (Figures 5(a)–5(e)). On the other hand, defects implanted with ACS and isotype-matched control mAb were occupied primarily by connective tissue (Figures 5(f)–5(j)). Similar to imaging data, histomicrographs illustrated that new bone formation was observed in direct apposition to the margins of old bone. There was no evidence of local inflammatory infiltration in either group. Quantitative histomorphometric analysis revealed greater percentage of

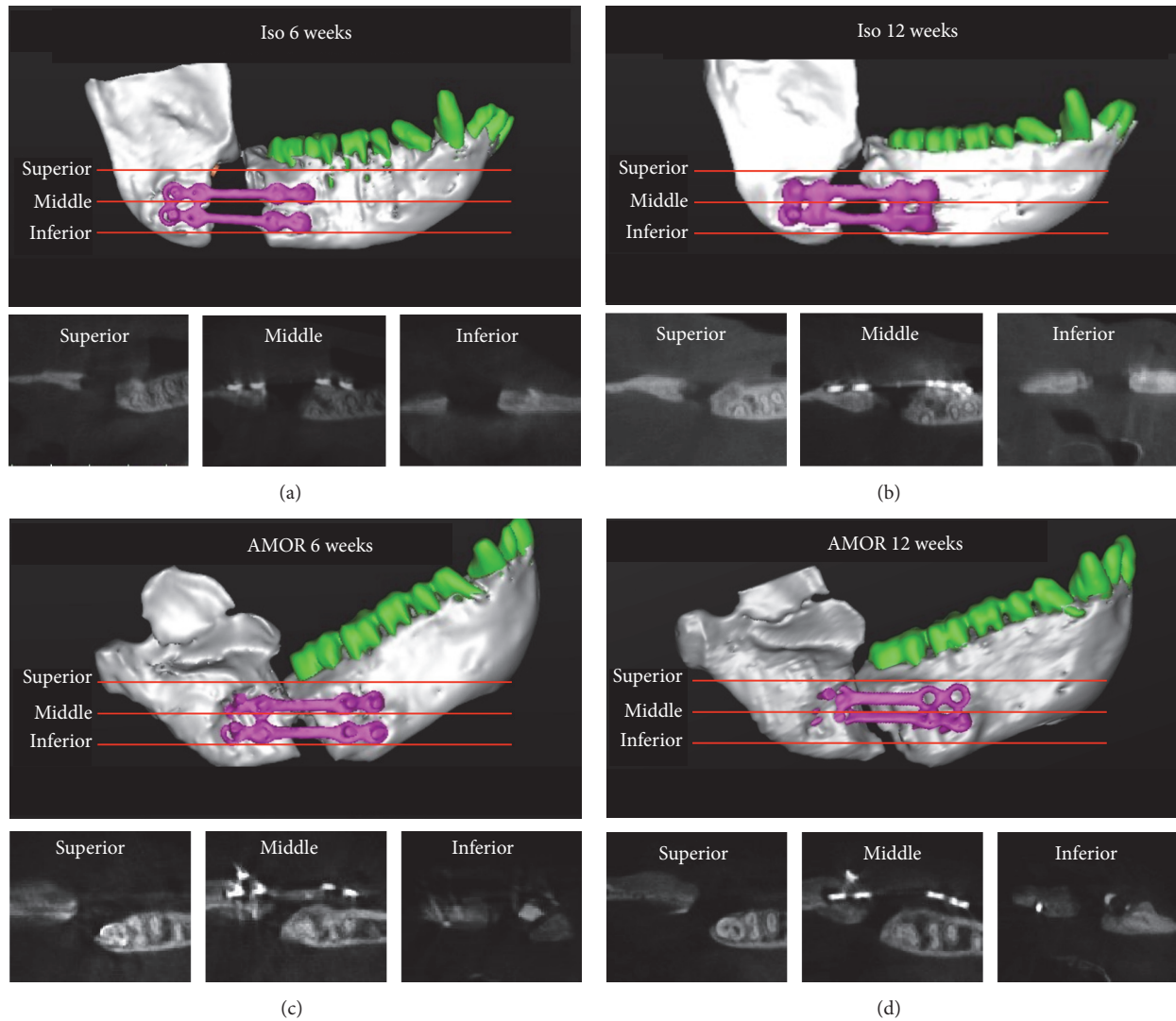


FIGURE 2: Representative 2D and 3D reconstructed CBCT images of mandibular continuity defects of experimental and control groups at 6 and 12 weeks postsurgically. 3D reconstructed CBCT images illustrate the landmarks used for axial plane sections for 2D image analysis. Accordingly, axial sections were obtained at equal distances from the superior region of the mandibular defects, above titanium plates (superior plane), as well as at middle (middle plane) and inferior regions (inferior plane) of the mandible. Representative 2D and 3D reconstructed images of defects treated with isotype-matched control mAb (a, b) or chimeric anti-BMP-2 mAb (c, d) at 6 (a, c) and 12 (b, d) time points are illustrated.

BV/TV within defects implanted with ACS functionalized with anti-BMP-2 mAb compared with isotype-matched control mAb (Figure 5(k)).

4. Discussion

Autogenous bone grafting has long been regarded as the gold standard for bone augmentation. However, there are many disadvantages associated with this treatment modality such as infection, hematoma, morbidity, and increased surgical expense. The use of allografts, xenografts, and synthetic biomaterials has enabled clinicians to avoid some of the disadvantages of autografts; however, application of these

types of materials is still limited. As an alternative treatment option, involving application of rhBMP-2 has been widely used for bone regenerative procedures, providing a promising alternative therapeutic option to autologous bone grafting. However, there are several disadvantages associated with the application of rhBMP-2. Recent studies from our research group have demonstrated a tissue engineering strategy involving immobilization of anti-BMP-2 mAb on various scaffolds implanted into surgical defect sites [14, 15, 17–20]. AMOR has been validated in calvarial defects of rats and rabbits [14, 15, 17–20]. In order to advance this translational project toward our ultimate goal of clinical trial, the present investigation sought to utilize a clinically relevant defect in an animal model that is phylogenetically closer to human. In

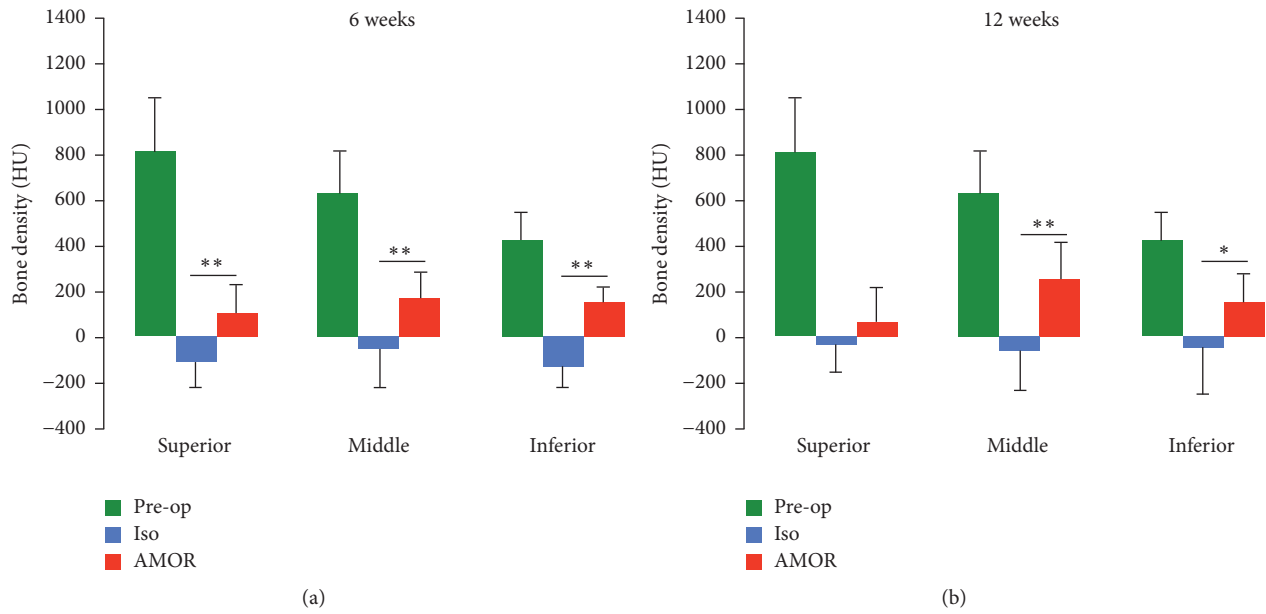


FIGURE 3: Quantitative analysis of bone density within axial images of CBCTs taken presurgically and at 6 (a) and 12 (b) weeks postsurgically. Bone density was measured within axial sections of CBCT images obtained from superior, middle, and inferior regions, according to the landmarks illustrated in Figure 2. The mean density of experimental mandibular area at preoperative time point is presented for comparison. Significantly higher bone density was observed within defects treated with chimeric anti-BMP-2 mAb compared to isotype-matched control mAb (* $P < 0.05$, ** $P < 0.01$).

the present study, critical-size continuity mandibular defects were generated in a nonhuman primate model. This is a clinically relevant animal model, mimicking many conditions where craniofacial bones are resected due to neoplastic, traumatic, or inflammatory lesions. Using this animal model, which is closely associated with human, we demonstrated the capacity of collagen scaffold functionalized with anti-BMP-2 mAb to mediate de novo bone formation within mandibular continuity defects. These data confirmed and extended our previous studies, demonstrating the efficacy of AMOR in rodents and rabbits [17–20].

Before a tissue engineering approach can be critically examined in a clinical trial, confirming the findings in a large animal model that closely mimics the clinical condition being studied is required [24, 25]. Our results provide further evidence in support of AMOR as a translational approach. Its efficacy and reproducibility have been demonstrated in a number of animals with different defect models [14–20].

The present experimental model is the largest defect which we have utilized to investigate the mechanism of AMOR. The present model has provided significant insights into the mechanism of osteogenesis within these defect sites. Firstly, the fact that application of anti-BMP-2 mAbs that were generated in a murine host against human BMP-2 antigen led to repair of large critical-size defects in monkeys suggests that this antibody is capable of capturing endogenous monkey BMP ligands. This may be attributed to the high degree of homology between human and monkey BMP molecules [26]. Secondly, two possible mechanisms may be suggested for osteogenesis through AMOR: (1) osteoconduction, that is, bone formation by direct opposition

on parent bone, and (2) de novo bone formation, which is bone repair without existing bone template. The present experiment showed bone repair was initiated and propagated at the margins of surgical defects. It may be hypothesized that the concentrations of endogenous BMPs are greatest at host bone that is responsible for this pattern of bone formation.

Over the past three decades, monoclonal antibody therapy has become one of the fastest growing areas of biopharmaceutical applications. The reason for the increasing popularity of therapeutic mAbs is their safety profile, high degree of specificity, diversity, and relatively low cost. The majority of current therapeutic mAbs are utilized for targeted therapy in three main areas, namely, cancer, immunity, and inflammation [27]. To date, the primary route of antibody administration is systemic administration, which may cause “infusion reaction” [27]. In the present study, anti-BMP-2 mAb was delivered using a collagen scaffold and implanted locally into the defect sites to mediate de novo bone formation. We have previously demonstrated that the locally implanted anti-BMP-2 mAb is slowly released, though it persists for at least 8 weeks [15, 19]. There were no side effects or adverse events detected in the current study. This is consistent with previous studies conducted in other animal models [17–20], suggesting the safety of local administration of anti-BMP-2 mAbs.

It has been demonstrated that BMPs in solution are quickly cleared from the body, which may explain why high doses of exogenous rhBMPs are needed for tissue regeneration [16]. The high dose of rhBMP currently approved by the FDA (1.5 mg/mL) is several orders of magnitude above physiological levels. Significant complications have

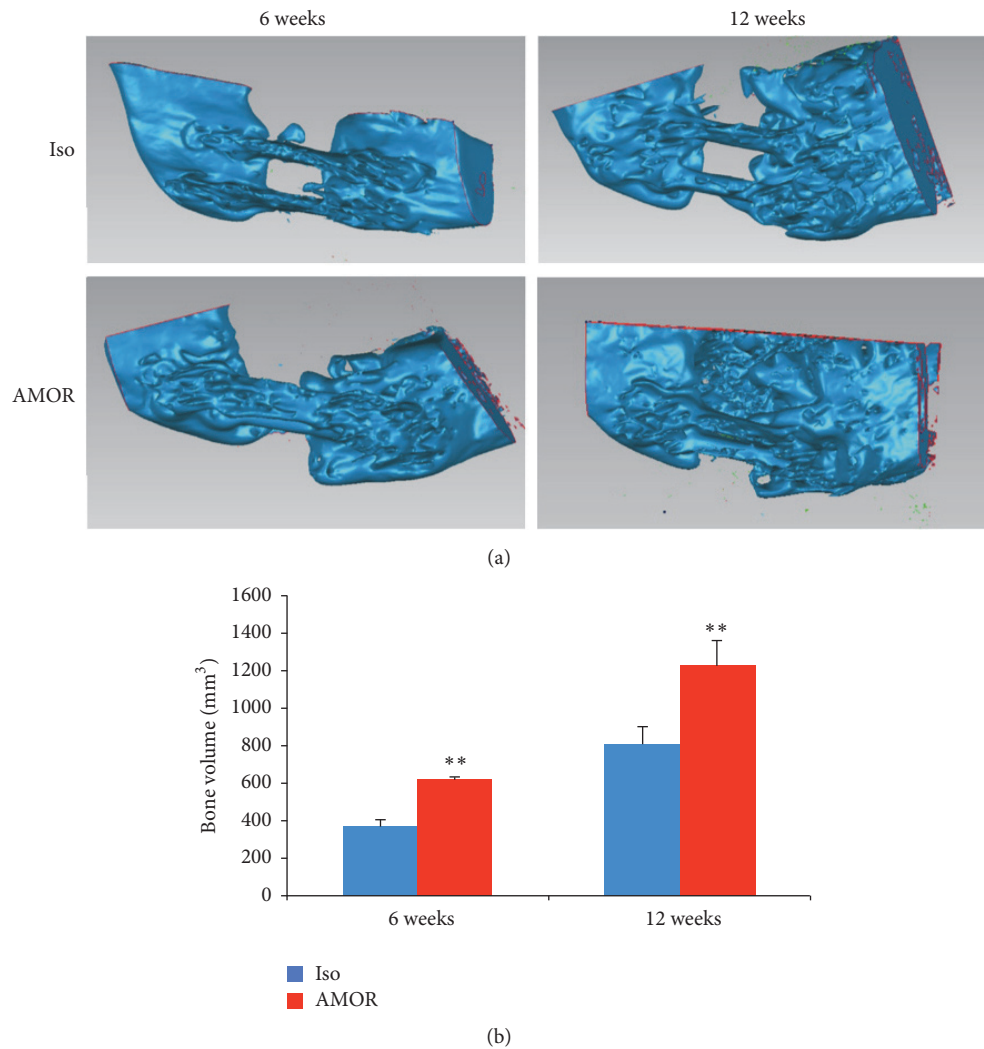


FIGURE 4: 3D analysis of bone volume within surgical defect. Mandibular continuity defects were treated with chimeric anti-BMP-2 mAb compared to isotype-matched control mAb. CBCT images taken at 6 and 12 weeks postsurgically and the volume of bone within the defect sites at two time points was quantified (a). Quantitative analysis of bone volume (mm³) within defects treated with chimeric anti-BMP-2 mAb or isotype-matched control mAb (b). Significantly higher bone volume was detected within defects treated with chimeric anti-BMP-2 mAb compared to isotype-matched control mAb at both time points (** $P < 0.01$).

been reported following rhBMP-2 administration, perhaps due to the superphysiologic concentration [28]. In the present study, we used ACS as the scaffold for immobilizing anti-BMP-2 mAb and observed significant de novo bone formation in large critical-size mandibular continuity defects. The contrasts between the application of exogenous growth factors and in situ trapping of endogenous growth factors by specific monoclonal antibodies are multifold:

- (1) Spatial and temporal availability of growth factors is linked to the biological process of wound healing. In normal biological wound healing, growth factors need to be present at the appropriate concentration in the local microenvironment at the appropriate time. In some circumstances, the availability of growth factors at an inappropriate time can have the opposite of the intended effect.

- (2) Endogenous growth factors have higher biological activity than their recombinant counterparts, presumably due to differences in posttranslational modification of endogenous growth factors.
- (3) Antibodies have excellent safety profiles, particularly when delivered locally as in AMOR.

In AMOR, the availability of growth factors is orchestrated by endogenous expression of those growth factors, expressed at the appropriate stage in the cascade of events during wound healing. AMOR merely amplifies the effects of the growth factors by facilitating their local accumulation via specific mAbs.

Since antibody therapy has been associated with some potential adverse reactions [29], it was important to address this issue. We carefully examined our histologic sections of mandible for presence of any signs of adverse reaction such

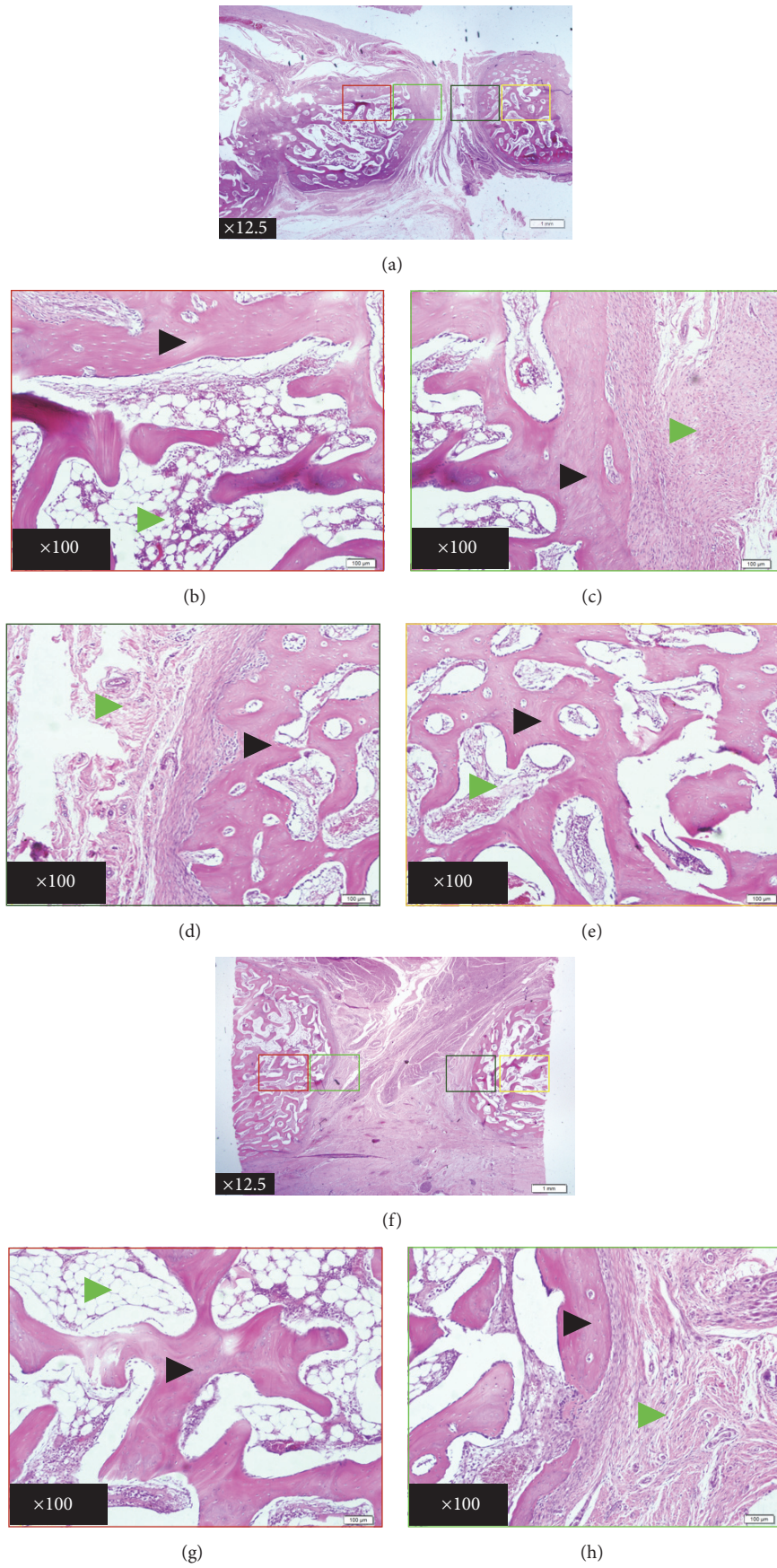


FIGURE 5: Continued.

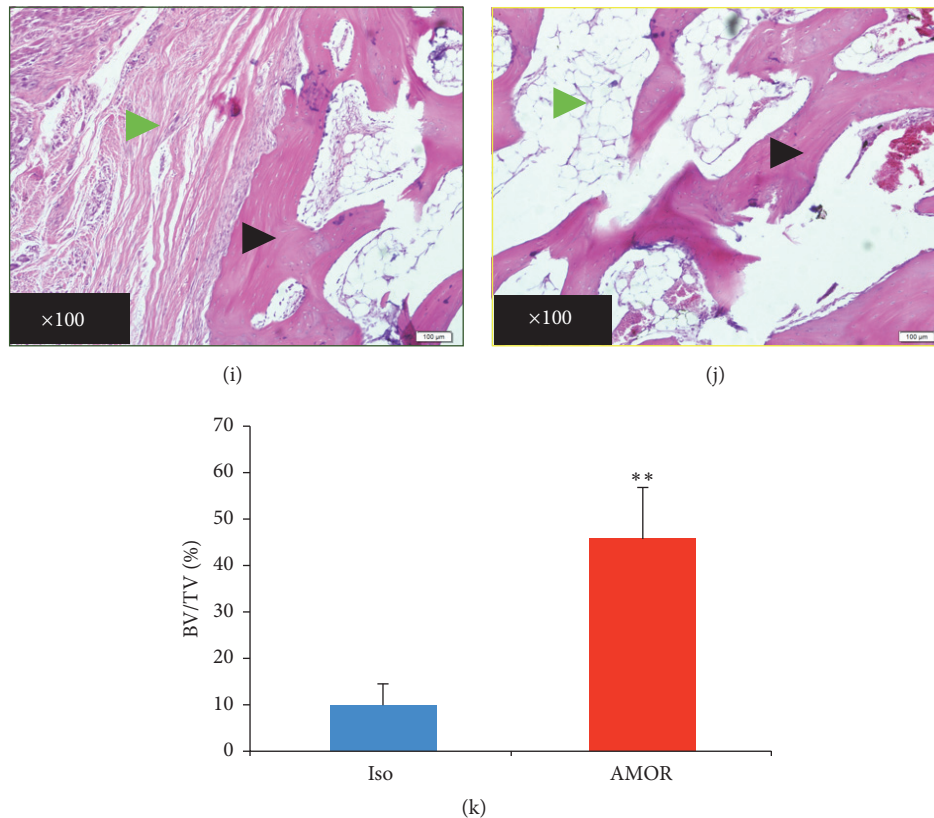


FIGURE 5: Histologic and histomorphometric analysis of treated mandibular defects. Histomicrographs of H&E stained sections obtained from axial planes taken at the midpoint between superior and inferior boundaries of mandibular defects (a–j). Mandibular segmental osteotomy defects were treated with chimeric anti-BMP-2 mAb (a–e) or isotype-matched control mAb (f–j) immobilized on absorbable collagen sponge scaffold. Histological evaluation 12 weeks after surgery revealed the presence of mature lamellar bone in the newly ossified tissue of experimental defect treated with chimeric anti-BMP-2 mAb (a–e), whereas isotype-matched control mAb (f–j) was primarily filled with connective tissue. There was no evidence of inflammatory infiltration in either group. Black and green arrowheads represent osteoid bone or all other tissues (referred to as void), respectively. Quantitative histomorphometric analysis of new bone formation (k) confirmed higher degree of bone formation within defects treated with chimeric anti-BMP-2 mAb compared with isotype-matched control mAb (** $P < 0.01$).

as exuberant inflammatory infiltrate and we did not observe significant inflammatory infiltrate in experimental or control sites. This is most likely due to the fact that the volume of diluted mAb solution (150 μ L) at 25 μ g/mL concentration used for incubation with the scaffolds entails maximum of 3.75 μ g of mAb administered. This dose is far lower than those used for typical therapeutic mAbs that are clinically administered. Moreover, since AMOR entails applying mAbs, which are immobilized on solid scaffold, the potential for adverse reaction is likely lower than most therapeutic mAbs which are systemically administered.

In view of the many complications and limitations reported for the current gold standard of bone repair (e.g., autogenous grafting) and the newer technology of recombinant growth factor therapy, there is currently a need for safe and effective alternatives for the treatment of significant skeletal defects. AMOR presents a viable alternative strategy and merits further investigation. Although chimeric antibodies are currently approved by the US FDA for clinical use, most of the therapeutic antibodies currently in use are

humanized or fully human. Humanized antibodies are generated by transfer of the complementarity determining region (CDR) of the antibody from another species onto a human Ab. Therefore, before clinical studies can be conducted on AMOR, humanized antibodies have to be generated. Currently, generation of humanized anti-BMP-2 mAbs which are suitable for clinical testing is in the planning stages.

5. Conclusion

In the present study, chimeric anti-BMP-2 mAb immobilized on ACS scaffold promoted de novo bone formation efficiently, as confirmed by a novel clinically relevant mandibular continuity defect in a nonhuman primate model. Altogether, our data demonstrate the efficacy of chimeric anti-BMP-2 mAb for bone tissue engineering applications. The strategy proposed herein has a multitude of potential clinical applications in the repair of skeletal defects due to congenital, traumatic, neoplastic, or inflammatory processes.

Disclosure

Portions of the data in this manuscript were presented in poster format at the 56th EXCIDA in conjunction with the 1st FDI Persian Regional and the 34th ICOI World Congress.

Competing Interests

The authors declare no potential conflict of interests with respect to the authorship and/or publication of this article.

Authors' Contributions

Yilin Xie and Yingying Su contributed equally. Bee Tin Goh, Leonardo Saigo, Yilin Xie, and Jianxia Tang performed the animal experiments. Yilin Xie and Yingying Su contributed to acquisition of histologic data, analysis of data, and drafting the manuscript. Chunmei Zhang and Jinsong Wang participated in analysis and interpretation of results. Seiko Min performed 2D image analysis. Yi Liu participated in interpretation of the results, was involved in drafting the manuscript, and reviewed it critically. Sahar Ansari, Alireza Moshaverinia, and Homayoun H. Zadeh developed and tested chimeric mAb and were involved in the design of experiments, interpretation of data, and writing the manuscript. Arash Khojasteh, Homayoun H. Zadeh, and Songlin Wang designed the experiments and reviewed the manuscript critically.

Acknowledgments

This work was partly supported by a grant from the National Natural Science Foundation of China (NSFC81222011, 81470751 to Yi Liu) and Beijing Municipality Government grants (Beijing Scholar Program, PXM 2013_014226_000055, PXM2015_014226_000116, PXM2015_014226_000055, PXM2015_014226_000052, PXM2014_014226_000048, PXM2014_014226_000013, PXM2014_014226_000053, Z121100005212004, PXM 2013_014226_000021, PXM 2013_014226_07_000080, and TJSHG201310025005 to Songlin Wang). Thorough editorial review by Dr. Bridget Samuels, Senior Editor at Center for Craniofacial Molecular Biology, Herman Ostrow School of Dentistry of USC, is acknowledged.

References

- [1] P. V. Giannoudis, H. Dinopoulos, and E. Tsiridis, "Bone substitutes: an update," *Injury*, vol. 36, pp. S20–S27, 2005.
- [2] E. Monaco, M. Bionaz, S. J. Hollister, and M. B. Wheeler, "Strategies for regeneration of the bone using porcine adult adipose-derived mesenchymal stem cells," *Theriogenology*, vol. 75, no. 8, pp. 1381–1399, 2011.
- [3] V. M. Betz, O. B. Betz, M. B. Harris, M. S. Vrahas, and C. H. Evans, "Bone tissue engineering and repair by gene therapy," *Frontiers in Bioscience*, vol. 13, no. 3, pp. 833–841, 2008.
- [4] W. G. De Long Jr., T. A. Einhorn, K. Koval et al., "Bone grafts and bone graft substitutes in orthopaedic trauma surgery. A critical analysis," *The Journal of Bone & Joint Surgery—American Volume*, vol. 89, no. 3, pp. 649–658, 2007.
- [5] M. Chin, T. Ng, W. K. Tom, and M. Carstens, "Repair of alveolar clefts with recombinant human bone morphogenetic protein (rhBMP-2) in patients with clefts," *Journal of Craniofacial Surgery*, vol. 16, no. 5, pp. 778–789, 2005.
- [6] I. Kratchmarova, B. Blagoev, M. Haack-Sorensen, M. Kassem, and M. Mann, "Cell signalling: mechanism of divergent growth factor effects in mesenchymal stem cell differentiation," *Science*, vol. 308, no. 5727, pp. 1472–1477, 2005.
- [7] J. Czyz and A. M. Wobus, "Embryonic stem cell differentiation: the role of extracellular factors," *Differentiation*, vol. 68, no. 4-5, pp. 167–174, 2001.
- [8] E. H. J. Groeneveld and E. H. Burger, "Bone morphogenetic proteins in human bone regeneration," *European Journal of Endocrinology*, vol. 142, no. 1, pp. 9–21, 2000.
- [9] W. K. Hsu and J. C. Wang, "The use of bone morphogenetic protein in spine fusion," *Spine Journal*, vol. 8, no. 3, pp. 419–425, 2008.
- [10] A. L. Jones, R. W. Bucholz, M. J. Bosse et al., "Recombinant human BMP-2 and allograft compared with autogenous bone graft for reconstruction of diaphyseal tibial fractures with cortical defects. A randomized, controlled trial," *The Journal of Bone & Joint Surgery—American Volume*, vol. 88, no. 7, pp. 1431–1441, 2006.
- [11] S. N. Khan and J. M. Lane, "The use of recombinant human bone morphogenetic protein-2 (rhBMP-2) in orthopaedic applications," *Expert Opinion on Biological Therapy*, vol. 4, no. 5, pp. 741–748, 2004.
- [12] W. Zhu, B. A. Rawlins, O. Boachie-Adjei et al., "Combined bone morphogenetic protein-2 and -7 gene transfer enhances osteoblastic differentiation and spine fusion in a rodent model," *Journal of Bone and Mineral Research*, vol. 19, no. 12, pp. 2021–2032, 2004.
- [13] U. M. E. Wikesjö, G. Polimeni, and M. Qahash, "Tissue engineering with recombinant human bone morphogenetic protein-2 for alveolar augmentation and oral implant osseointegration: experimental observations and clinical perspectives," *Clinical Implant Dentistry and Related Research*, vol. 7, no. 2, pp. 112–119, 2005.
- [14] S. Ansari, M. Freire, M. G. Choi et al., "Effects of the orientation of anti-BMP2 monoclonal antibody immobilized on scaffold in antibody-mediated osseous regeneration," *Journal of Biomaterials Applications*, vol. 30, no. 5, pp. 558–567, 2015.
- [15] S. Ansari, A. Moshaverinia, S. H. Pi, A. Han, A. I. Abdelhamid, and H. H. Zadeh, "Functionalization of scaffolds with chimeric anti-BMP-2 monoclonal antibodies for osseous regeneration," *Biomaterials*, vol. 34, no. 38, pp. 10191–10198, 2013.
- [16] A. Moshaverinia, S. Ansari, C. Chen et al., "Co-encapsulation of anti-BMP2 monoclonal antibody and mesenchymal stem cells in alginate microspheres for bone tissue engineering," *Biomaterials*, vol. 34, no. 28, pp. 6572–6579, 2013.
- [17] M. O. Freire, H.-K. You, J.-K. Kook, J.-H. Choi, and H. H. Zadeh, "Antibody-mediated osseous regeneration: a novel strategy for bioengineering bone by immobilized anti-bone morphogenetic protein-2 antibodies," *Tissue Engineering Part A*, vol. 17, no. 23-24, pp. 2911–2918, 2011.
- [18] M. O. Freire, H. K. Kim, J.-K. Kook, A. Nguyen, and H. H. Zadeh, "Antibody-mediated osseous regeneration: the early events in the healing response," *Tissue Engineering Part A*, vol. 19, no. 9-10, pp. 1165–1174, 2013.
- [19] S. Ansari, M. O. Freire, E.-K. Pang, A. I. Abdelhamid, M. Almohaimeed, and H. H. Zadeh, "Immobilization of murine

- anti-BMP-2 monoclonal antibody on various biomaterials for bone tissue engineering,” *BioMed Research International*, vol. 2014, Article ID 940860, 10 pages, 2014.
- [20] M. Freire, J.-H. Choi, A. Nguyen et al., “Application of AMOR in craniofacial rabbit bone bioengineering,” *BioMed Research International*, vol. 2015, Article ID 628769, 7 pages, 2015.
- [21] S. Min, Y. Liu, J. Tang et al., “Alveolar ridge dimensional changes following ridge preservation procedure with novel devices: part 1—CBCT linear analysis in non-human primate model,” *Clinical Oral Implants Research*, vol. 27, no. 1, pp. 97–105, 2016.
- [22] M. Omran, S. Min, A. Abdelhamid, Y. Liu, and H. H. Zadeh, “Alveolar ridge dimensional changes following ridge preservation procedure: part-2—CBCT 3D analysis in non-human primate model,” *Clinical Oral Implants Research*, vol. 27, pp. 859–866, 2016.
- [23] D. W. Dempster, J. E. Compston, M. K. Drezner et al., “Standardized nomenclature, symbols, and units for bone histomorphometry: a 2012 update of the report of the ASBMR Histomorphometry Nomenclature Committee,” *Journal of Bone and Mineral Research*, vol. 28, no. 1, pp. 2–17, 2013.
- [24] G. F. Muschler, V. P. Raut, T. E. Patterson, J. C. Wenke, and J. O. Hollinger, “The design and use of animal models for translational research in bone tissue engineering and regenerative medicine,” *Tissue Engineering. Part B: Reviews*, vol. 16, no. 1, pp. 123–145, 2010.
- [25] J. Harding, R. M. Roberts, and O. Mirochnitchenko, “Large animal models for stem cell therapy,” *Stem Cell Research and Therapy*, vol. 4, no. 2, article no. 23, 2013.
- [26] K. L. Abrams, J. Xu, C. Nativelle-Serpentini, S. Dabirshahsahebi, and M. B. Rogers, “An evolutionary and molecular analysis of Bmp2 expression,” *The Journal of Biological Chemistry*, vol. 279, no. 16, pp. 15916–15928, 2004.
- [27] J. M. Reichert, C. J. Rosensweig, L. B. Faden, and M. C. Dewitz, “Monoclonal antibody successes in the clinic,” *Nature Biotechnology*, vol. 23, no. 9, pp. 1073–1078, 2005.
- [28] E. J. Carragee, E. L. Hurwitz, and B. K. Weiner, “A critical review of recombinant human bone morphogenetic protein-2 trials in spinal surgery: emerging safety concerns and lessons learned,” *Spine Journal*, vol. 11, no. 6, pp. 471–491, 2011.
- [29] R. W. Schroff, K. A. Foon, S. M. Beatty, R. K. Oldham, and A. C. Morgan Jr., “Human anti-murine immunoglobulin responses in patients receiving monoclonal antibody therapy,” *Cancer Research*, vol. 45, no. 2, pp. 879–885, 1985.

Research Article

Cytotoxicity and Antimicrobial Effects of a New Fast-Set MTA

Michelle Shin,¹ Jung-Wei Chen,¹ Chi-Yang Tsai,² Raydolfo Aprecio,³ Wu Zhang,⁴
Ji Min Yochim,¹ Naichia Teng,^{2,5} and Mahmoud Torabinejad⁶

¹Department of Pediatric Dentistry, School of Dentistry, Loma Linda University, Loma Linda, CA 92350, USA

²School of Dentistry, College of Oral Medicine, Taipei Medical University, 250 Wu-Hsing Street, Taipei, Taiwan

³Biomechanics Research Laboratory, Center for Dental Research, Orthodontics and Dentofacial Orthopedics, Loma Linda University, Loma Linda, CA 92350, USA

⁴Dental Education Services, School of Dentistry, Loma Linda University, Loma Linda, CA 92350, USA

⁵Division of Oral Rehabilitation and Center of Pediatric Dentistry, Department of Dentistry, Taipei Medical University Hospital, 252 Wu-Hsing Street, Taipei, Taiwan

⁶Department of Endodontics, School of Dentistry, Loma Linda University, Loma Linda, CA 92350, USA

Correspondence should be addressed to Naichia Teng; tengnaichia@hotmail.com

Received 6 October 2016; Revised 2 January 2017; Accepted 11 January 2017; Published 20 February 2017

Academic Editor: Satoshi Imazato

Copyright © 2017 Michelle Shin et al. This is an open access article distributed under the Creative Commons Attribution License, which permits unrestricted use, distribution, and reproduction in any medium, provided the original work is properly cited.

Purpose. To compare the biocompatibility and antimicrobial effectiveness of the new Fast-Set MTA (FS-MTA) with ProRoot MTA (RS-MTA). **Methods.** The agar overlay method with neutral red dye was used. L929 mouse fibroblast cells were cultured. The liquid and oil extracts and solid test material were placed on the agar overlay, four samples for each material. Phenol was used as the positive control and cottonseed oil and MEM extracts were used as negative controls. Cytotoxicity was examined by measuring the zones of decolorization and evaluating cell lysis under an inverted microscope using the established criteria after 24 and 48 hours. The antimicrobial test was performed using the Kirby-Bauer disk-diffusion method against *S. mutans*, *E. faecalis*, *F. nucleatum*, *P. gingivalis*, and *P. intermedia*. The size of the zone of inhibition was measured in millimeters. **Results.** There was no zone of decolorization seen under or around the test materials for FS-MTA and RS-MTA at 24 and 48 hours. The antimicrobial test demonstrated no inhibitory effect of FS-MTA or RS-MTA on any bacterial species after 24 and 48 hours. **Conclusions.** There was no cytotoxicity or bacterial inhibition observed by the new Fast-Set MTA when compared to the ProRoot MTA after setting.

1. Introduction

Mineral trioxide aggregate was primarily created as a root-end filling material in surgical endodontic procedures [1]. It has since then been indicated for other uses such as pulp capping, apexogenesis, and apexification in immature teeth with necrotic pulp, filling of root canals, treatment of horizontal root fractures, internal and external resorption, and repair of perforations [2]. It has been recognized as a bioactive material that is hard tissue conductive, hard tissue inductive, and biocompatible, which further idealizes MTA as a repair material in endodontic procedures [3]. In primary teeth, MTA is mainly used for direct pulp capping and pulpotomy procedures [2]. A new “Fast-Set MTA” has been developed by Dr. Mahmoud Torabinejad in Loma Linda, California.

Fast-Set MTA (FS-MTA) is a brand new material that was developed to be as effective as MTA with the added advantage of a quicker setting time. The setting time of the modified MTA has been reduced to 20 minutes. Current research studies are being conducted on bacterial microleakage and physical and chemical properties. Different methods have been tested to shorten the setting time of MTA, including a light-cured MTA and the addition of accelerants, such as disodium hydrogen orthophosphate and calcium lactate gluconate; all of these affect the physical or chemical properties of MTA in some way [4–6]. A fast-setting MTA will have the clinical advantages of increasing the usage of MTA in a dental practitioner’s scope of practice, including pediatric dentistry. Because pediatric patients can often be restless and uncooperative, a fast-setting MTA can shorten the amount of chair time and increase the likelihood of a proper seal

in a shorter amount of time. Since it is to be in permanent and close contact with periradicular tissues, it is important to assess its possible cytotoxic effects on living cells [7]. Bacteria are the main culprits for the development of pulp and periapical disease; since existing materials may not provide a perfect and hermetic seal, it is desirable that the material can prevent bacterial growth [8].

The purpose of this study is to compare the biocompatibility and antimicrobial effectiveness in vitro of the new gray Fast-Set MTA (FS-MTA) with regular ProRoot Gray MTA (RS-MTA) by using two tests: the agar diffusion test for cytotoxicity on L929 mouse fibroblast cells and the Kirby-Bauer disk-diffusion method for measuring the antimicrobial effect.

2. Materials and Methods

2.1. Test Material Preparation

2.1.1. Solid Material. The gray ProRoot MTA (Dentsply, Lot Number 12120401B) was mixed according to the manufacturer's instructions and condensed into an internal diameter of 10 mm and thickness of 2 mm Teflon o-rings, which were then allowed to completely set in an incubator at 37°C for 24 hours. For the test material, a L/P = 1:4 ratio of FS-MTA was mixed and condensed into the o-rings and allowed to set in the same conditions. It was determined that the material was completely set when the tip of a clean explorer did not leave an indentation in the cement with typical force.

2.1.2. Extracts. The test material was prepared in the same manner as above and then the sets of FS-MTA and RS-MTA were put in sterile water prepared at concentrations of 0.2 g/mL to determine the volume of the solvent for the liquid extract. Eagle's minimal essential medium (MEM) or PBS (FS-MTA MEM/PBS and RS-MTA MEM/PBS) was used as the polar solvent, and cottonseed oil (FS-MTA oil and RS-MTA oil) was used as the nonpolar solvent. The extracts were incubated at 37°C in a humidified 5% CO₂ incubator for 72 hours before the experiment. The extracts were filtered before use using a 0.22 µm syringe filter on the day of the experiment.

2.2. Agar Overlay Method for Cytotoxicity. The cytotoxicity-agar diffusion test is a means to evaluate the cytotoxicity of a test material using the agar diffusion method as specified in ISO 7405 (2008) and ISO 10993-5 (2009) and adapted from the method used by Torabinejad et al. [9–11].

Mouse fibroblast L929 cells (NCTC clone 929, ATCC CCL 1, Manassas, VA) were grown to confluence and trypsinized using Trypsin-EDTA mixture (Difco Laboratories, Detroit, MI). The cell density was determined using an automated cell counter (Countess, Invitrogen, CA) and the concentration was adjusted to 1.0×10^5 cells/mL. The cell suspensions were aliquoted into 6-well plates (5 mL/well) and incubated for 24 hours. The media were then withdrawn and an overlay agar (3% agar (Difco Laboratories, Detroit, MI) in 2x complete media at the ratio of 1:1), maintained at 45°C, was poured

over the cell monolayer. The agar media were allowed to solidify at room temperature for 10 minutes. Then 200 µL of neutral red solution (0.033%) was pipetted on the agar surface and the excess dye was removed after 20 minutes. The extract samples (50 µL) were aliquoted onto sterile filter disks (6 mm diameter, AP Prefilter Filter Paper, Lot Number H8KM39502, Millipore Corporation, Bedford, MA). The filter disks and solid samples were placed at the center of the agar surfaces. The positive control used was phenol, and the negative controls were sterile MEM and cottonseed oil. The tests were run with four samples of each group, each in a separate 6-well plate to avoid cross contamination of the materials. The plates were incubated at 37°C in a humidified atmosphere of 5% CO₂ for 24 and 48 hours. The cytotoxicity was examined by measuring the zone of decolorization and evaluating cell lysis under an inverted microscope using the established criteria (ISO 7405, 2008) after 24 and 48 hours of incubation.

2.3. Kirby-Bauer Disk-Diffusion Method for Antimicrobial Effect. The Kirby-Bauer disk-diffusion measures the effect of an antimicrobial agent against bacteria. The bacterial cultures used in this study were *Streptococcus mutans* (ATCC 25175), *Enterococcus faecalis* (ATCC 19433), *Fusobacterium nucleatum* (ATCC 49256), *Prevotella intermedia* (ATCC 49046), and *Porphyromonas gingivalis* (ATCC 33277). The bacteria density was adjusted to an optical density equivalent to 0.1 at 600 nm using the Ultrospec 10 Spectrophotometer (Amersham Biosciences). One hundred microliters of the adjusted concentration of bacterial culture was spread uniformly across the culture plate using an L-shaped glass rod. Trypticase Soy Agar (Becton Dickinson, Sparks, MD) was used to plate the *S. mutans* and *E. faecalis*. Brucella Blood Agar (BRU) Plates (Anaerobe Systems, Morgan Hill, CA) were used to plate *P. gingivalis*, *F. nucleatum*, and *P. intermedia*. Four filter-paper disks (0.25 inches in diameter) were then placed on each quadrant on the surface of the agar plate, and 20 µL of the test material extract was pipetted onto each of the filter-paper disks. The same procedure was applied for the negative control, phosphate buffered saline, and positive control, 5.25% sodium hypochlorite (NaOCl). NaOCl is the main irrigating solution used to dissolve organic matter and kill microbes effectively, and a higher concentration has a better effect than 1-2% solutions [12]. The solid samples of test materials were directly placed in contact to the surface of the agar. Each plate contained 4 samples of the test material. The data was collected by measuring the zone of inhibition in millimeters at 24 hours and 48 hours.

All the data was collected and tabulated for descriptive statistics. All the data collection was negative; thus, no inferential statistics were performed.

3. Results

For the cytotoxicity test, there was no zone of decolorization seen under or around the test materials for either the RS-MTA or the FS-MTA. The negative control did not show any zone of decolorization under or around the filter-paper disks at 24 and 48 hours. The cells were viewed under 40x and 100x magnification. The positive control showed

TABLE 1: Cytotoxicity evaluation of FS-MTA and RS-MTA, using evaluation criteria for agar diffusion test (ISO 7405, 2008). For zone index, 0 indicates no detectable decolorization zone; a score of 5 indicates a zone involving the entire dish. For lysis index, a score of 0 indicates no observable cytotoxicity, 5 indicates > 80% of the decolorized zone affected. For interpretation of cytotoxicity, score of 0 indicates being noncytotoxic, and 3 indicates severe toxicity.

Material	24 hours			48 hours		
	Zone index	Lysis index	Interpretation	Zone index	Lysis index	Interpretation
MEM (-control)	0	0	Noncytotoxic	0	0	Noncytotoxic
Cottonseed oil (-control)	0	0	Noncytotoxic	0	0	Noncytotoxic
Phenol (+control)	5	5	Severely cytotoxic	5	5	Severely cytotoxic
RS-MTA solid	0	0	Noncytotoxic	0	0	Noncytotoxic
RS-MTA MEM	0	0	Noncytotoxic	0	0	Noncytotoxic
RS-MTA oil	0	0	Noncytotoxic	0	0	Noncytotoxic
FS-MTA solid	0	0	Noncytotoxic	0	0	Noncytotoxic
FS-MTA MEM	0	0	Noncytotoxic	0	0	Noncytotoxic
FS-MTA oil	0	0	Noncytotoxic	0	0	Noncytotoxic

TABLE 2: Measurements of zone of inhibition in millimeters (mm) at 24 and 48 hours for RS-MTA and FS-MTA solid, extract, and oil samples at 24 and 48 hours on bacterial species, and $N = 4$.

Material	<i>S. mutans</i>		<i>E. faecalis</i>		<i>P. gingivalis</i>		<i>P. intermedia</i>		<i>F. nucleatum</i>	
	24 h	48 h	24 h	48 h	24 h	48 h	24 h	48 h	24 h	48 h
PBS (-control)	0.00	0.00	0.00	0.00	0.00	0.00	0.00	0.00	0.00	0.00
NaOCl 5.25% (+control)	29.17 ± 0.29	29.17 ± 0.29	25.67 ± 2.31	25.67 ± 2.31	28.33 ± 2.47	28.33 ± 2.47	9.67 ± 1.15	9.67 ± 1.15	10.00 ± 0.50	10.00 ± 0.50
RS-MTA PBS	0.00	0.00	0.00	0.00	0.00	0.00	0.00	0.00	0.00	0.00
RS-MTA oil	0.00	0.00	0.00	0.00	0.00	0.00	0.00	0.00	0.00	0.00
RS-MTA solid	0.00	0.00	0.00	0.00	0.00	0.00	0.00	0.00	0.00	0.00
FS-MTA PBS	0.00	0.00	0.00	0.00	0.00	0.00	0.00	0.00	0.00	0.00
FS-MTA oil	0.00	0.00	0.00	0.00	0.00	0.00	0.00	0.00	0.00	0.00
FS-MTA solid	0.00	0.00	0.00	0.00	0.00	0.00	0.00	0.00	0.00	0.00

complete decolorization and cellular lysis of all the wells as seen in Table 1. The results are reported in the table as the average of the four samples. The data was classified into a five-point cytotoxicity grading system. The negative controls and the gray RS-MTA and gray FS-MTA all received a cytotoxicity grade of 0, and the positive control received the maximum grade of 5 for decolorization and lysis index and was graded a maximum of 3 for cytotoxicity interpretation (severely cytotoxic). Figure 1 illustrates the cells at a higher magnification (magnification at 100x), in the presence of FS-MTA oil sample at the border of the filter paper, the negative control, and positive controls. The fibroblast cells' uptake of neutral red dye after 24 hours, the presence of red dye, and absence of lysed cells show that these cells are vital.

There was no inhibitory effect of FS-MTA or RS-MTA on the aerobic bacteria, *S. mutans* and *E. faecalis*, or the anaerobic bacteria, *F. nucleatum*, *P. intermedia*, or *P. gingivalis*, in 24 and 48 hours. The negative control did not show any zone of inhibition in all of the bacteria species. The positive control showed zone of inhibition in all the bacteria species (Table 2). The results are reported as the average of the three samples. Figures 2(a)–2(h) show the results of FS-MTA and RS-MTA on *E. faecalis* when compared to the control groups; no zone of inhibition was detected.

4. Discussion

Multiple tests to determine the biocompatibility of dental materials exist, such as cytotoxicity tests in tissue cultures, in vivo subcutaneous or bone implant tests, and usage tests [11]. Cytotoxicity tests are inexpensive, simple, and rapid and can be used as a screening test, which can provide helpful information as to whether or not a material should be further tested for potential use in humans. The types of cell lines that are used for tissue culture cytotoxicity tests include L929 mouse fibroblasts, gingival fibroblast cells, and human PDL cells [13–15]. This study used L929 mouse fibroblasts, as it is a commonly used cell line.

There are three qualitative cytotoxicity tests that are commonly used for testing medical materials: the direct contact procedure, agar diffusion assay, and MEM elution assay. The direct contact procedure is recommended for low-density materials, agar diffusion assay is appropriate for high-density materials, and the MEM elution assay uses different extracting media and extraction conditions to test devices according to the actual conditions or to exaggerate those conditions [16]. A zone of malformed, degenerative, or lysed cells under and around the test material shows that the material is cytotoxic. Our test results did not show any

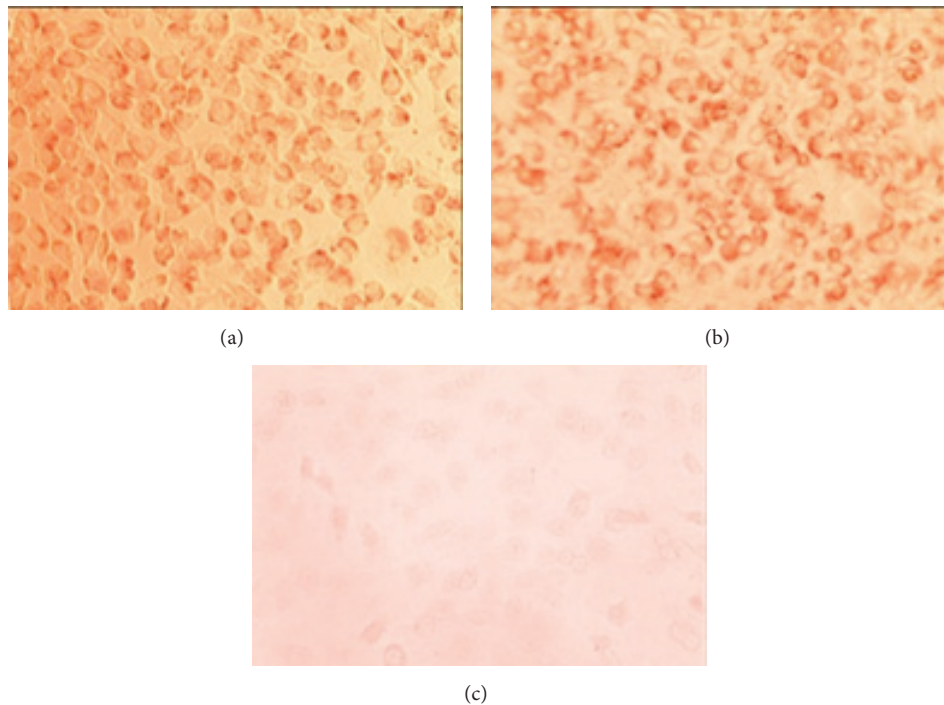


FIGURE 1: (a) FS-MTA oil sample at the border of the filter paper, (b) negative control, MEM, and (c) positive control, phenol. The cells are intact and in monolayer, with uptake of neutral red dye, indicating vitality of the cells, 100x.

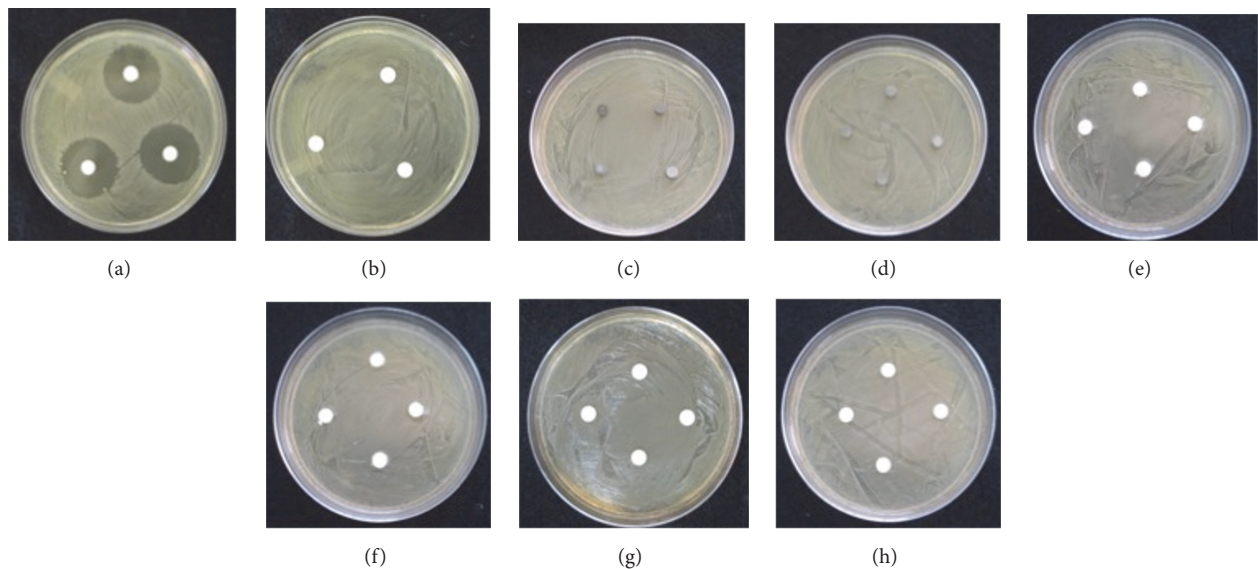


FIGURE 2: Agar diffusion test to measure the inhibition of FS-MTA and RS-MTA on bacterial growth; this particular grouping is result for *E. faecalis*. (a) Positive control, NaOCl 5.25%, (b) negative control, PBS, (c) RS-MTA solid, (d) FS-MTA solid, (e) RS-MTA oil, (f) FS-MTA oil, (g) RS-MTA PBS, and (h) FS-MTA PBS. Note that there is no zone of inhibition in any of the samples of RS-MTA or FS-MTA.

malformed or degenerated cells under or around the samples of FS-MTA, in either the extracts or the solid samples.

The agar overlay method has been used in multiple cytotoxicity tests, including Torabinejad et al. [11], who reported a zone of lysis around samples of fresh and set gray MTA. Haglund reported there were denatured medium

proteins and dead cells adjacent to the material, but only in the fresh MTA group; however the set MTA had no effect on cell morphology [17]. Miranda et al. tested 48-hour set MTA, which showed viable cells around the pellets, and dead cells were observed only under the material [18]. The results of our study showed that there was no effect on cell morphology

from either the FS-MTA or RS-MTA in the set form or the extract forms under or around the test material or extract after 24 and 48 hours.

MTA has been shown to be one of the least cytotoxic dental materials in comparison to Super EBA, IRM, amalgam, various types of glass ionomers, gutta-percha, and Dycal [13]. Our study showed that this modified form of FS-MTA does not show any cytotoxic effects on L929 mouse fibroblast cells. Although our tests were sufficient enough to screen this new material for cytotoxicity, biocompatibility testing regulation (ANSI/AAMI/ISO 10993-5:2009) has stated that qualitative tests are appropriate for screening purpose but quantitative evaluation would be preferable [16]. Our study demonstrated that the new FS-MTA does not have any cytotoxic properties and is comparable to the RS-MTA.

The Kirby-Bauer disk-diffusion method was the test used to evaluate the antibacterial properties of FS-MTA in comparison to RS-MTA. This is one of the most widely used in vitro methods for the evaluation of antimicrobial activity and allows direct comparisons between materials that could have antibacterial action [19, 20]. It has been shown that the antibacterial effect of sealers generally decreases in a set state, because once the setting reaction has been completed, diffusion in the agar is difficult [19]; the same could be stated of MTA, which is cement that undergoes a setting reaction. For this reason, we used extracts of the test materials to ensure that the leachable elements were evaluated as well as the solid material.

We used two facultative bacteria species and three anaerobic bacteria species for our tests. Of more than 300 bacterial species that are present in the normal oral flora, a relatively small group colonizes infected root canals—mainly of strict anaerobes and some facultative anaerobes and usually no aerobes [21]. Our study did not show any inhibitory effect of the FS-MTA or RS-MTA on the facultative anaerobic species *S. mutans* and *E. faecalis*, nor was there any inhibitory effect on the anaerobic bacteria, *F. nucleatum*, *P. gingivalis*, and *P. intermedia*.

S. mutans has been found to be present in the dentinal tubules of 48.7% of infected root canals and is the primary causal agent and pathogenic species responsible for dental caries because of its ability to produce acid and initiate the caries process [22]. In infected primary teeth, *P. gingivalis*, *P. intermedia*, and *F. nucleatum* were found in high percentages in both the pulp chamber and root canals [23]. *E. faecalis* is a primary pathogenic factor in endodontic treatment and is detectable in about 77% of cases that are resistant to treatment [24]. Tanomaru-Filho et al. showed that gray ProRoot MTA inhibited various facultative bacteria in a freshly mixed state [25].

Torabinejad et al. reported that both fresh and set MTA had antibacterial effect on *S. mitis* but not *S. faecalis*, *S. aureus*, and *B. subtilis*, all of which are facultative bacteria [21]. The fresh and set MTA also showed some antibacterial effect on *S. mutans*. Of the anaerobic bacteria, the same study showed that there was no antibacterial effect against any of the anaerobic bacteria tested: *P. buccae*, *B. fragilis*, *P. intermedia*, *P. melaninogenica*, *P. anaerobius*, *F. necrophorum*, and *F. nucleatum* [21]. Heyder et al. discovered that ProRoot

MTA only had an antibacterial effect in a freshly mixed state but did not inhibit any growth on anaerobes. ProRoot MTA did not have any inhibitory effect on *E. faecalis* in either the freshly mixed or set forms [24]. However, in our study, we did not see any inhibition of bacterial growth in the extracts or solid samples of the FS-MTA and RS-MTA.

The antimicrobial effects seen in MTA are thought to be from its high pH or release of diffusible substances into the growth medium, especially in the freshly mixed state [3]. We did not use freshly mixed FS-MTA and RS-MTA in our study, which may have shown a different outcome; however, we did use extracts that should contain any leachable components of the FS-MTA and RS-MTA if they were indeed present [16]. The pH of the extracts was not tested before the placement of the disks onto the bacteria-inoculated agar plates. It may be helpful to test the new material, FS-MTA, in a freshly mixed state to evaluate the antibacterial effect it may have before complete setting of the cement. Ultimately, our study showed that there was no difference between the antibacterial properties between the new FS-MTA and RS-MTA, as there was no inhibition of the bacterial species tested.

To improve this study, the biocompatibility of the new FS-MTA can be tested quantitatively with a test such as the MTT assay and can further be tested on human gingival fibroblast cells rather than mouse fibroblast cells. To further test the antibacterial properties of the new FS-MTA, it may be helpful to compare the freshly mixed state of the new product with the RS-MTA.

5. Conclusion

Under the condition of the present study, the new FS-MTA was not cytotoxic in the L929 mouse fibroblast cell line, and there was no difference between the FS-MTA and the RS-MTA. Also, the new FS-MTA did not show antimicrobial properties against the facultative anaerobic species, *S. mutans* and *E. faecalis*, or the strict anaerobic species, *P. gingivalis*, *P. intermedia*, and *F. nucleatum*. There was no difference in antimicrobial effect between the FS-MTA and the RS-MTA.

Competing Interests

The authors declare that there is no conflict of interests regarding the publication of this paper.

References

- [1] R. P. Anthonappa, N. M. King, and L. C. Martens, "Is there sufficient evidence to support the long-term efficacy of mineral trioxide aggregate (MTA) for endodontic therapy in primary teeth?" *International Endodontic Journal*, vol. 46, no. 3, pp. 198–204, 2013.
- [2] V. Srinivasan, P. Waterhouse, and J. Whitworth, "Mineral trioxide aggregate in paediatric dentistry," *International Journal of Paediatric Dentistry*, vol. 19, no. 1, pp. 34–47, 2009.
- [3] M. Parirokh and M. Torabinejad, "Mineral trioxide aggregate: a comprehensive literature review—part I: chemical, physical, and antibacterial properties," *Journal of Endodontics*, vol. 36, no. 1, pp. 16–27, 2010.

- [4] J. E. Gomes-Filho, M. D. de Faria, P. F. E. Bernabé et al., "Mineral trioxide aggregate but not light-cure mineral trioxide aggregate stimulated mineralization," *Journal of Endodontics*, vol. 34, no. 1, pp. 62–65, 2008.
- [5] S. J. Ding, C. T. Kao, M. Y. Shie, C. Hung Jr., and T. H. Huang, "The Physical and cytological properties of white MTA mixed with Na_2HPO_4 as an accelerant," *Journal of Endodontics*, vol. 34, no. 6, pp. 748–751, 2008.
- [6] S.-C. Hsieh, N.-C. Teng, Y.-C. Lin et al., "A novel accelerator for improving the handling properties of dental filling materials," *Journal of Endodontics*, vol. 35, no. 9, pp. 1292–1295, 2009.
- [7] H.-M. Zhou, Y. Shen, Z.-J. Wang et al., "In vitro cytotoxicity evaluation of a novel root repair material," *Journal of Endodontics*, vol. 39, no. 4, pp. 478–483, 2013.
- [8] S. Asgary and F. A. Kamrani, "Antibacterial effects of five different root canal sealing materials," *Journal of Oral Science*, vol. 50, no. 4, pp. 469–474, 2008.
- [9] "ISO 7405:2008: Evaluation of biocompatibility of medical devices used in dentistry," International Organization for Standardization-ISO, Geneva, Switzerland.
- [10] "ISO 10993-5: 2009: biological compatibility of medical devices—Part 5. Tests for cytotoxicity," in *In Vitro Methods*, International Organization of Standardization, Geneva, Switzerland, 1992.
- [11] M. Torabinejad, C. U. Hong, T. R. Pitt Ford, and J. D. Kettering, "Cytotoxicity of four root end filling materials," *Journal of Endodontics*, vol. 21, no. 10, pp. 489–492, 1995.
- [12] M. Haapasalo, Y. Shen, Z. Wang, and Y. Gao, "Irrigation in endodontics," *British Dental Journal*, vol. 216, no. 6, pp. 299–303, 2014.
- [13] M. Torabinejad and M. Parirokh, "Mineral trioxide aggregate: a comprehensive literature review—part II: leakage and biocompatibility investigations," *Journal of Endodontics*, vol. 36, no. 2, pp. 190–202, 2010.
- [14] M. A. Camp, B. G. Jeansonne, and T. Lallier, "Adhesion of human fibroblasts to root-end-filling materials," *Journal of Endodontics*, vol. 29, no. 9, pp. 602–607, 2003.
- [15] E.-C. Kim, B.-C. Lee, H.-S. Chang, W. Lee, C.-U. Hong, and K.-S. Min, "Evaluation of the radiopacity and cytotoxicity of Portland cements containing bismuth oxide," *Oral Surgery, Oral Medicine, Oral Pathology, Oral Radiology and Endodontology*, vol. 105, no. 1, pp. e54–e57, 2008.
- [16] Cytotoxicity (Tissue Culture), http://www.pacificbiolabs.com/bio_methods.asp.
- [17] R. Haglund, J. He, J. Jarvis, K. E. Safavi, L. S. W. Spångberg, and Q. Zhu, "Effects of root-end filling materials on fibroblasts and macrophages in vitro," *Oral Surgery, Oral Medicine, Oral Pathology, Oral Radiology, and Endodontics*, vol. 95, no. 6, pp. 739–745, 2003.
- [18] R. B. Miranda, S. R. Fidel, and M. A. A. Boller, "L929 cell response to root perforation repair cements: an in vitro cytotoxicity assay," *Brazilian Dental Journal*, vol. 20, no. 1, pp. 22–26, 2009.
- [19] M. R. Leonardo, L. A. B. Da Silva, M. Tanomaru Filho, K. C. Bonifácio, and I. Y. Ito, "In vitro evaluation of antimicrobial activity of sealers and pastes used in endodontics," *Journal of Endodontics*, vol. 26, no. 7, pp. 391–394, 2000.
- [20] D. C. Miyagak, E. M. O. F. de Carvalho, C. R. C. Robazza, J. K. Chavasco, and G. L. Levorato, "In vitro evaluation of the antimicrobial activity of endodontic sealers," *Brazilian Oral Research*, vol. 20, no. 4, pp. 303–306, 2006.
- [21] M. Torabinejad, C. U. Hong, T. R. P. Ford, and J. D. Kettering, "Antibacterial effects of some root end filling materials," *Journal of Endodontics*, vol. 21, no. 8, pp. 403–406, 1995.
- [22] T. Klinke, S. Kneist, J. J. de Soet et al., "Acid production by oral strains of *Candida albicans* and lactobacilli," *Caries Research*, vol. 43, no. 2, pp. 83–91, 2009.
- [23] G. B. Gomes, R. Sarkis-Onofre, M. L. M. Bonow, A. Etges, and R. C. Jacinto, "An investigation of the presence of specific anaerobic species in necrotic primary teeth," *Brazilian Oral Research*, vol. 27, no. 2, pp. 149–155, 2013.
- [24] M. Heyder, S. Kranz, A. Völpel et al., "Antibacterial effect of different root canal sealers on three bacterial species," *Dental Materials*, vol. 29, no. 5, pp. 542–549, 2013.
- [25] M. Tanomaru-Filho, J. M. G. Tanomaru, D. B. Barros, E. Watanabe, and I. Y. Ito, "In vitro antimicrobial activity of endodontic sealers, MTA-based cements and Portland cement," *Journal of Oral Science*, vol. 49, no. 1, pp. 41–45, 2007.

Research Article

Developing Customized Dental Miniscrew Surgical Template from Thermoplastic Polymer Material Using Image Superimposition, CAD System, and 3D Printing

Yu-Tzu Wang,¹ Jian-Hong Yu,² Lun-Jou Lo,³ Pin-Hsin Hsu,¹ and CHun-Li Lin¹

¹Department of Biomedical Engineering, National Yang-Ming University, Taipei, Taiwan

²School of Dentistry, College of Medicine, China Medical University, Taichung, Taiwan

³Plastic & Reconstructive Surgery, Department of Surgery, Chang Gung Memorial Hospital, Taiwan

Correspondence should be addressed to CHun-Li Lin; cllin2@ym.edu.tw

Received 11 November 2016; Revised 8 January 2017; Accepted 19 January 2017; Published 9 February 2017

Academic Editor: Wei-Jen Chang

Copyright © 2017 Yu-Tzu Wang et al. This is an open access article distributed under the Creative Commons Attribution License, which permits unrestricted use, distribution, and reproduction in any medium, provided the original work is properly cited.

This study integrates cone-beam computed tomography (CBCT)/laser scan image superposition, computer-aided design (CAD), and 3D printing (3DP) to develop a technology for producing customized dental (orthodontic) miniscrew surgical templates using polymer material. Maxillary bone solid models with the bone and teeth reconstructed using CBCT images and teeth and mucosa outer profile acquired using laser scanning were superimposed to allow miniscrew visual insertion planning and permit surgical template fabrication. The customized surgical template CAD model was fabricated offset based on the teeth/mucosa/bracket contour profiles in the superimposition model and exported to duplicate the plastic template using the 3DP technique and polymer material. An anterior retraction and intrusion clinical test for the maxillary canines/incisors showed that two miniscrews were placed safely and did not produce inflammation or other discomfort symptoms one week after surgery. The fitness between the mucosa and template indicated that the average gap sizes were found smaller than 0.5 mm and confirmed that the surgical template presented good holding power and well-fitting adaption. This study addressed integrating CBCT and laser scan image superposition; CAD and 3DP techniques can be applied to fabricate an accurate customized surgical template for dental orthodontic miniscrews.

1. Introduction

The orthodontic miniscrew provides skeletal anchorage with the advantages of being relatively inexpensive, easily implemented, and predictable enough to be used routinely in medical practice [1]. Nonetheless, the failure rates of interradicularly inserted miniscrews are considered still too high [2]. The miniscrew placement poses a challenge to the orthodontist because of the limited space available for miniscrew placement and the potential risk for root damage, puncture to the maxillary sinus, and neurovascular damage during miniscrew placement procedures [3]. Safe and optimal miniscrew stabilization requires ideal placement point and trajectory. Several methods have been developed to achieve precise and safe miniscrew placement in interradicular sites; however, they cannot guarantee precise placement [4–11]. A

controllable method for miniscrew placement and direction is important for orthodontists.

Traditionally, 2-dimensional (2D) information in the radiographs is usually used for surgical sites planning to minimize the root damage risks [7–9]. A metal wire-guide is used to superimpose radiograph images for analyzing surgical plan coordinates, distances, and angles and the corresponding miniscrew assessment [7]. However, metal wire bending skills are necessary and difficult to bend in shallow sulcus areas [5, 6]. Otherwise, direction of 2D radiograph should be parallel to the occlusal guide which limited 2D projection images and still cannot solve the 3-dimensional spatial error occurring during miniscrew placement or eliminate the risk for root injury [5, 6]. Custom-made surgical guides and templates have recently been proposed for transferring computed tomography (CT) images to the surgical site and outlining the

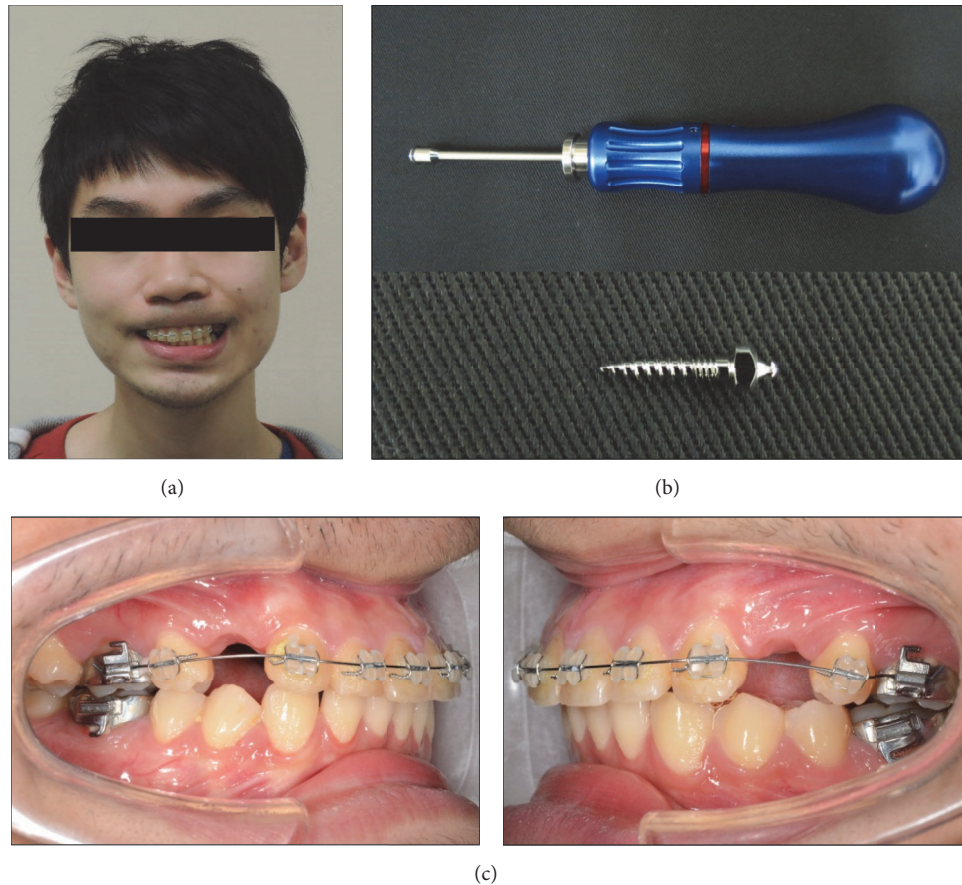


FIGURE 1: (a) A 25-year-old male patient with skeletal Class II occlusal features; (b) dual-thread miniscrew (materials: Ti6Al4V, Bomei Co, Ltd, Taoyuan, Taiwan) 1.6 mm in diameter and 8 mm in length was selected as the anchor implants; (c) two miniscrews were planned for insertion at the canine-second premolar space of the left/right buccal sites to provide a controlled anterior retraction and intrusion with power chain for the maxillary canines/incisors.

ideal miniscrew axis, to promote safe miniscrew placement into the dentoalveolar bone [4, 10, 11]. However, fabricating the accuracy and fit of individualized surgical guides is time-consuming and requires extensive advance preparation because CT images only isolate the hard tissue positions (jawbone or teeth). Another template needed to be fabricated on the stone cast with the vacuum-formed technique for providing radiopaque landmarks for further CT scan alignment. Complex double CT scan, landmark definition, and image processing procedures are needed to identify the accurate position and thickness of the soft tissue (mucosa) that comes in direct contact with the surgical templates [1, 4, 7].

This study integrates image superposition of CBCT/laser scanning, computer-aided design (CAD), and rapid prototyping technologies to develop a simplified, accurate technique for producing customized miniscrew surgical templates with adaptive fitness between the mucosa and template for accurate miniscrew insertion paths.

2. Materials and Methods

2.1. Image Superimposition and Miniscrew Inserted Path Definition. The patient was a 25-year-old male patient with

skeletal Class II occlusal features (Figure 1(a)). Two dual-thread miniscrews (materials: Ti6Al4V, Bomei Co, Ltd, Taoyuan, Taiwan) 1.6 mm in diameter and 8 mm in length were selected as the anchor implants and planned for insertion at the canine-second premolar space of the left/right buccal sites to provide a controlled anterior retraction and intrusion with power chain for the maxillary canines/incisors (Figures 1(b) and 1(c)).

CBCT (Cone-Beam Computed Tomography, Asahi AZ3000, Kyoto-shi, Japan) scan with 0.155 mm interval was performed on the patient to reconstruct the 3D maxillae model. All DICOM CT cross-section image data were processed on a personal PC using commercially available image processing software (Amira, v4.1, Mercury Computer Systems, Chelmsford, MA). This approach allowed identifying the contours of different hard tissues (cortical, cancellous bone and teeth) and those contours were extracted and converted into mathematical entities. A 3D solid model of the maxillary bone with teeth was reconstructed (Figures 2(a)–2(c)).

In order to ensure that the surgical template would fit well with the patient's teeth and soft tissue (mucosa), a maxilla impression was taken to make a stone cast (Figure 3(a)). The

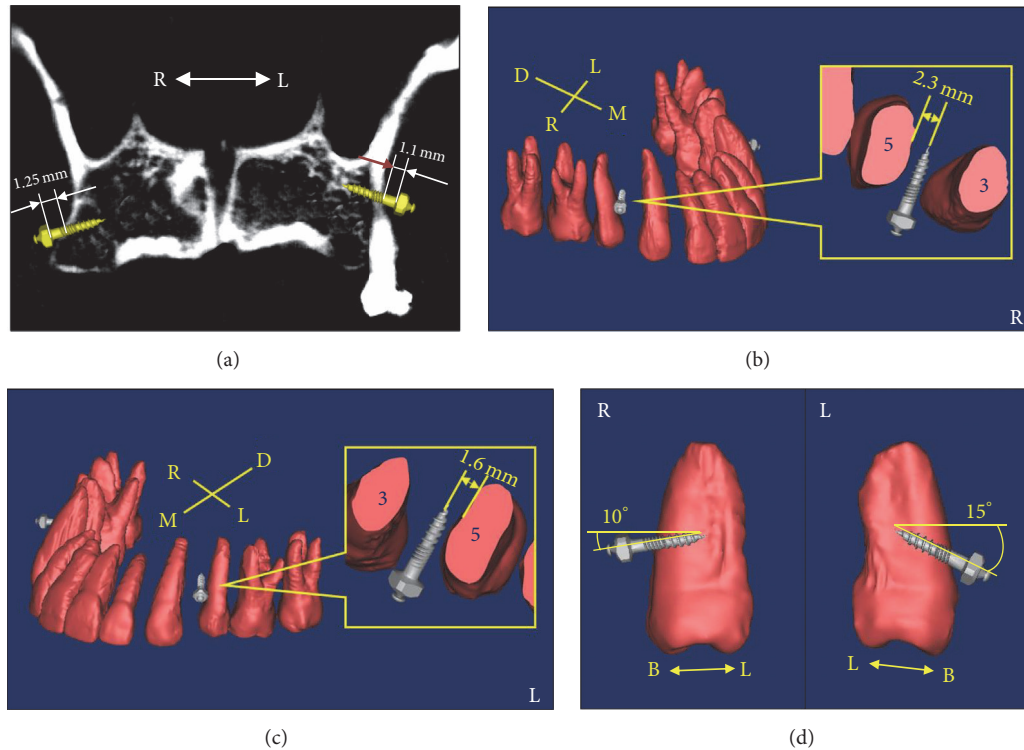


FIGURE 2: (a) Section image of CBCT reconstructed model to identify the contours of cortical, cancellous bone and teeth for planning the miniscrews microthreads to contact the cortical bone layer; (b) and (c) 3D solid model of the maxillary bone with teeth was reconstructed for surgical miniscrew planning at right and left sites; (d) two miniscrews were planned to insert to the occlusal surface inclination at angles of 15° and 10° for the left and right placement sites.

stone cast was then scanned using a 3D surface laser scan system (3Shape Scanners, 3D Scan CO., Ltd., USA) to make a digital 3D impression model for recording the geometry and profile of the teeth and mucosa (Figure 3(a)). Solid models of maxillary bone with teeth reconstructed using CBCT images and maxillary dental arches with mucosa acquired using laser scanning were superimposed using the common register positions at the distoincisor angle of left/right incisors and distobuccal cusp of left/right first molar (Figures 3(b) and 3(c)). The superimposition model consisted of hard tissue (bone and teeth) positions to allow miniscrew visual insertion planning accurate orientation and teeth/mucosa/bracket contour profiles to permit surgical template fabrication with well-fitting adaption.

The CAD miniscrew models were imported and placed in safe and optimal positions, that is, between the canine and second premolar space and as close as possible to premolar for canine distal drive when the teeth roots were visualized (Figures 2(b) and 2(c)). The distance between the second premolar and canine roots for the miniscrew were measured. The periodontal ligament is about 0.15 to 0.38 mm thick on average (assumed as 0.4 mm in this study) [4, 12, 13] and the miniscrew diameter in this study was 1.6 mm. The safe distance between the second premolar root and miniscrew axis was calculated and should be larger than 1.2 mm, that is, the sum of the periodontal ligament thickness is 0.4 mm

and miniscrew radius is 0.8 mm for safe placement. Two miniscrews were inserted to the occlusal surface inclination at angles of 15° and 10° for the left and right placement sites (Figure 2(d)). The insertion depth was controlled to allow the miniscrew microthreads to contact the cortical bone layer for better stabilization (Figure 2(a)).

2.2. Surgical Template Fabrication and Interfacial Adaption Test. The customized surgical template CAD model was fabricated with a 1.8 mm thick layer average offset based on the teeth/mucosa/bracket contour profiles in previous superimposition models, ranging from half canine to second molar (Figures 4(a) and 4(b)). The surgical template height was designed to cover the entire occlusal surface and extend to half the crown height to protect the orthodontic brackets bonded onto each tooth. The miniscrew drill paths and guided cylinders (5.3 mm in diameter and 6 mm in height) were generated in the surgical template CAD model according to previous 3D information from the visual surgical plan (Figures 4(a) and 4(b)). The solid surgical template model can be exported as a stereo-lithographic (STL) file that can be loaded into a fused deposition modeling (FDM) 3D printing (3DP) printer with 0.254 mm slicing additive manufacturing (Dimension 1200es SST, Stratasys, Ltd., Minnesota, USA) to duplicate the acrylonitrile butadiene styrene (ABS) (ABS-P430, Stratasys, Ltd., Minnesota, USA) polymer material

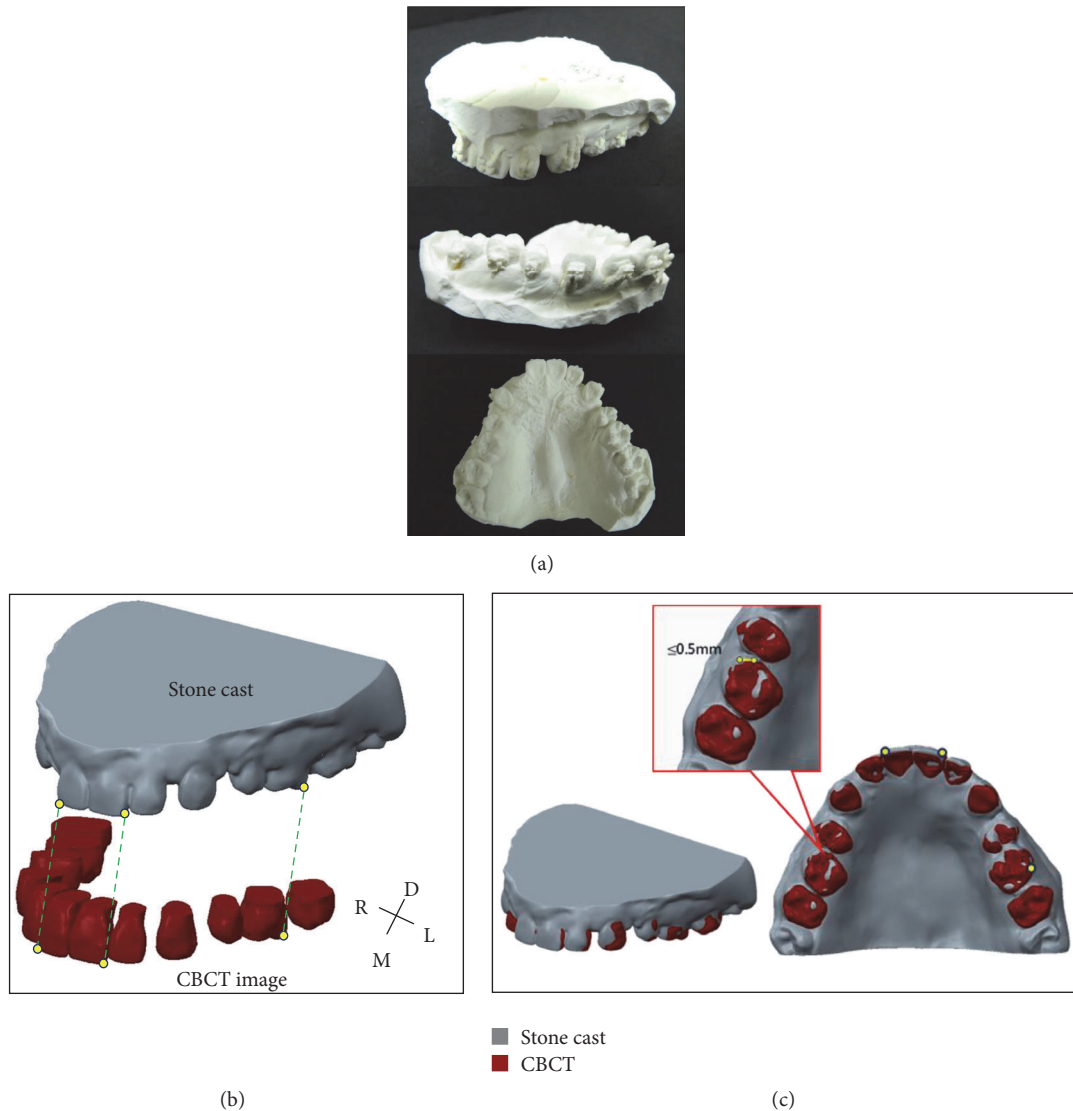


FIGURE 3: (a) Stone cast was fabricated from the patient (including teeth/mucosa/bracket contour profiles); (b) reconstructed models from CBCT and laser scanning images; (c) solid models of maxillary bone with teeth reconstructed using CBCT images and maxillary dental arches with mucosa acquired using laser scanning were superimposed using the common register positions at the distoincisor angle of left/right incisors and distobuccal cusp of left/right first molar.

template (Figure 5). The ABS material is a thermoplastic polymer with mechanical properties suitable to endure impact resistance and toughness.

In order to evaluate the interfacial fitness accuracy, an interfacial adaption test was performed to measure the gap sizes between the surgical template and teeth/mucosa tissue [1]. The customized surgical template was fitted onto teeth/mucosa stone cast models and embedded into clear rectangular test boxes with epoxy resin (Truetime Industrial Co., Taiwan) to provide a stable base. The resin block was sectioned in the buccal-palatal direction from the second premolar to molar with 6 section slices using a low speed diamond saw with copious cooling (CL50 Precision Saw, Top Tech Machines Co., Ltd., Taiwan) (Figure 6). The section slices were scanned using a noncontact video measurement

system (SVP-2010, ARCS Co., Ltd., Taichung, Taiwan) to measure the gap sizes at 5 points with 45° separation in the counterclockwise direction on each section.

2.3. Clinical Test. The surgical templates were placed intraorally onto the teeth by a clinician after the patient was given a local anesthetic (Figure 7(a)). The fitting adaption accuracy between the surgical template and teeth should be confirmed again with the surgical template held in place using the patient's bite force. Once the template was seated the patient was asked to bite the template to expose the guide surgical sites. The miniscrews were then placed with a screwdriver (Figures 7(b)–7(e)) until the screw head bottom slightly touched the mucosa. X-rays were taken after implantation to assess whether damage to the peripheral tissue occurred for

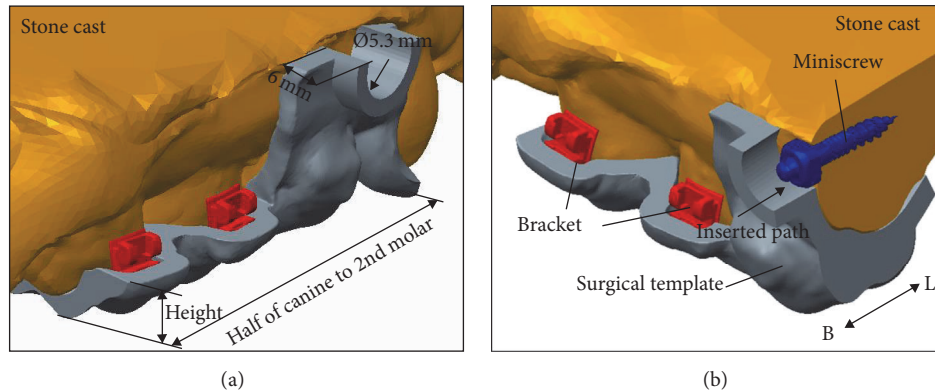


FIGURE 4: (a) and (b) The customized surgical template was 1.8 mm thick layer average offset based on the teeth/mucosa/bracket contour profiles and ranged from half canine to second molar. The surgical template height was designed to cover the entire occlusal surface and extend to half the crown height to protect the orthodontic brackets bonded onto each tooth. The miniscrew drill paths and guided cylinders were designed 5.3 mm in diameter and 6 mm in height.

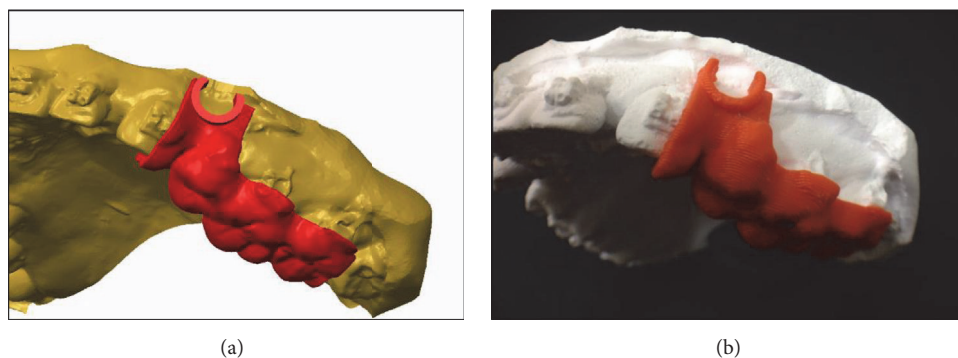


FIGURE 5: (a) The assembly solid models of stone cast of dental arch and left site surgical template; (b) the surgical template (left site) was fabricated using a 3DP printer with 0.254 mm slicing additive manufacturing and wore on the stone cast.

assessing miniscrew stability (Figure 7(f)). The patient was given instructions for postoperative care and antibiotics were prescribed (500 mg amoxicillin 4 times daily for 3 days).

3. Results and Discussion

Safe distances between the second premolar root and miniscrew axis were designed 1.6 mm and 2.3 mm for the left and right buccal insertion placements, respectively (Figures 2(b) and 2(c)). The clinical application indicated that two miniscrews were placed smoothly, safely, and without problems. No inflammation, screw loosening, or other symptoms of discomfort had occurred one week after surgery.

Miniscrews are always placed at an inclined angle, obviously limiting 2D image measurement. CT scan therefore must be used to measure the interradiacal spaces for accurate and reproducible results. CT scan has become an important diagnostic tool for the craniofacial region and is used for many applications including the study of treatment planning for orthognathic and reconstructive surgery, bone grafting, distraction osteogenesis, and dental implantology. However, the CT characteristic only presents/identifies deeper anatomical hard tissue, which often limits its applicability in surgery

guiding templates [4, 14, 15]. Much effort and numerous methods such as double CT scans for hard tissue and the radiographic template and landmark definition used with metal wires/balls were proposed to identify the contour profile and thickness of soft tissue (mucosa) that comes into direct contact with surgical templates [1, 4, 7]. This study proposes an image superimposition method using laser scan and CBCT images to improve the surgical template interfacial fitting adaption problem. Laser scanning can be used as a complementary tool for designing surgical templates because the images obtained from laser scanning can present the patient's dental arch with a good degree of similarity and may enhance the holding power and stability of the surgical template.

The stability and inherent support of the surgical template is a crucial factor. The template in this study was supported using 3 surfaces—occlusal teeth and buccal/palatal mucosa. The bite forces on the template provided support to keep it stable. The results of the interfacial adaption test showed that the average gap sizes in the different tooth sections were found to be smaller than 0.5 mm (total average 0.30 ± 0.10 mm) (Tables 1 and 2) and confirmed that the image superimposed method can produce a surgical template with good holding power and well-fitting adaption. It is difficult

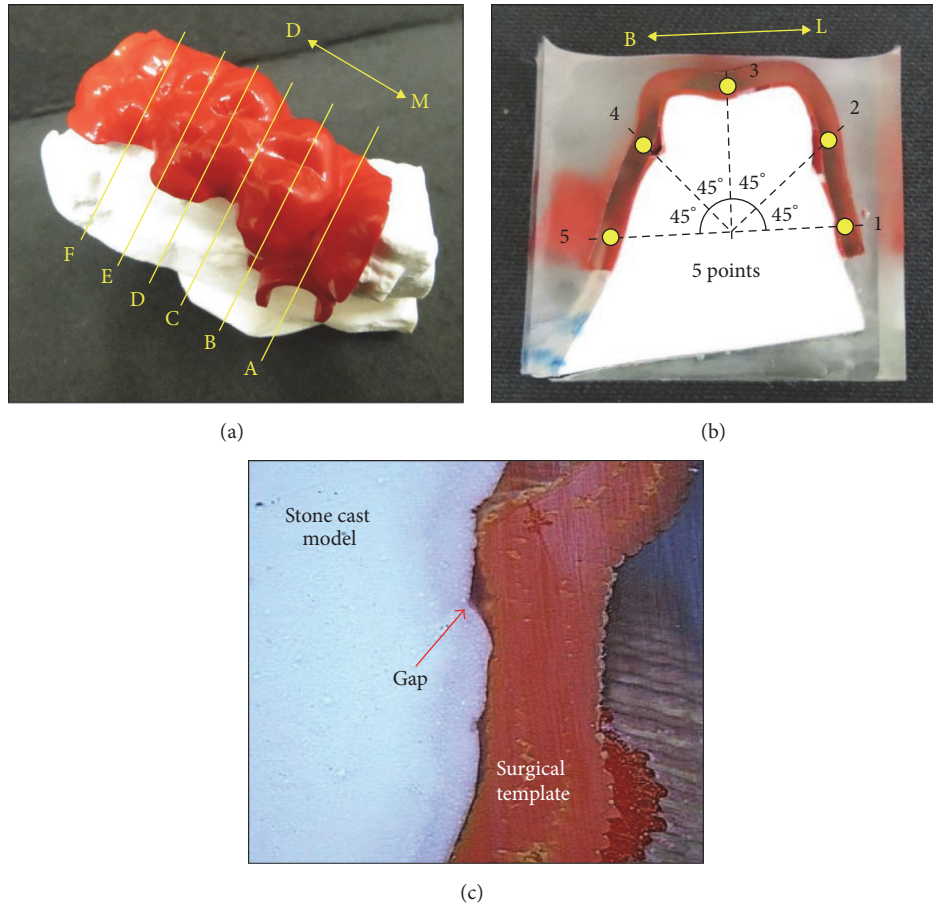


FIGURE 6: (a) Customized surgical template was fitted on the teeth/bracket/mucosa stone cast model of the patient to perform the interfacial adaption test. Six (A–F) buccal–palatal direction sections were obtained using a diamond saw; (b) and (c) each cutting section was scanned using a noncontact video measurement system to measure the gap sizes for 5 points with 45° separation in the counterclockwise direction on each section.

TABLE 1: Gap size of the interfacial adaption test of left surgical template (unit: mm).

Section	Placement	Point					Average	SD
		1	2	3	4	5		
A	Canine	0.29	0.40	0.11	0.09	0.13	0.20	0.12
B	2nd Premolar	0.33	0.06	0.30	0.05	0.09	0.17	0.12
C	2nd Premolar/1st Molar	0.55	0.27	0.35	0.54	0.47	0.44	0.11
D	1st Molar	0.33	0.20	0.32	0.48	0.40	0.35	0.09
E	1st Molar	0.53	0.38	0.17	0.10	0.28	0.29	0.15
F	2nd Molar	0.38	0.67	0.29	0.16	0.25	0.35	0.18
Total average							0.30 ± 0.10	

to compare other template holding power accuracy directly to that of our fitting adaption which was not evaluated in these literatures [4–11]. Nevertheless, surgical template with well-fitting adaption dominates and is relative to the precise miniscrew placement. The study by Liu et al. showed that the linear distomesial deviation of placing miniscrews was 0.42 mm at the tip. This deviation may be useful to compare the accuracy of our surgical template fitting adaption (average

0.30 mm in gap size) and confirmed that the image superimposed method can produce a surgical template with good holding power and well-fitting adaption.

The 3D superposition digital model from CBCT and laser scanning images produced accurate hard tissue relationship positions (bone and teeth) to simulate miniscrews placed in the safe position with ideal inclined angle and positions. Dual-thread miniscrews with correct microthread

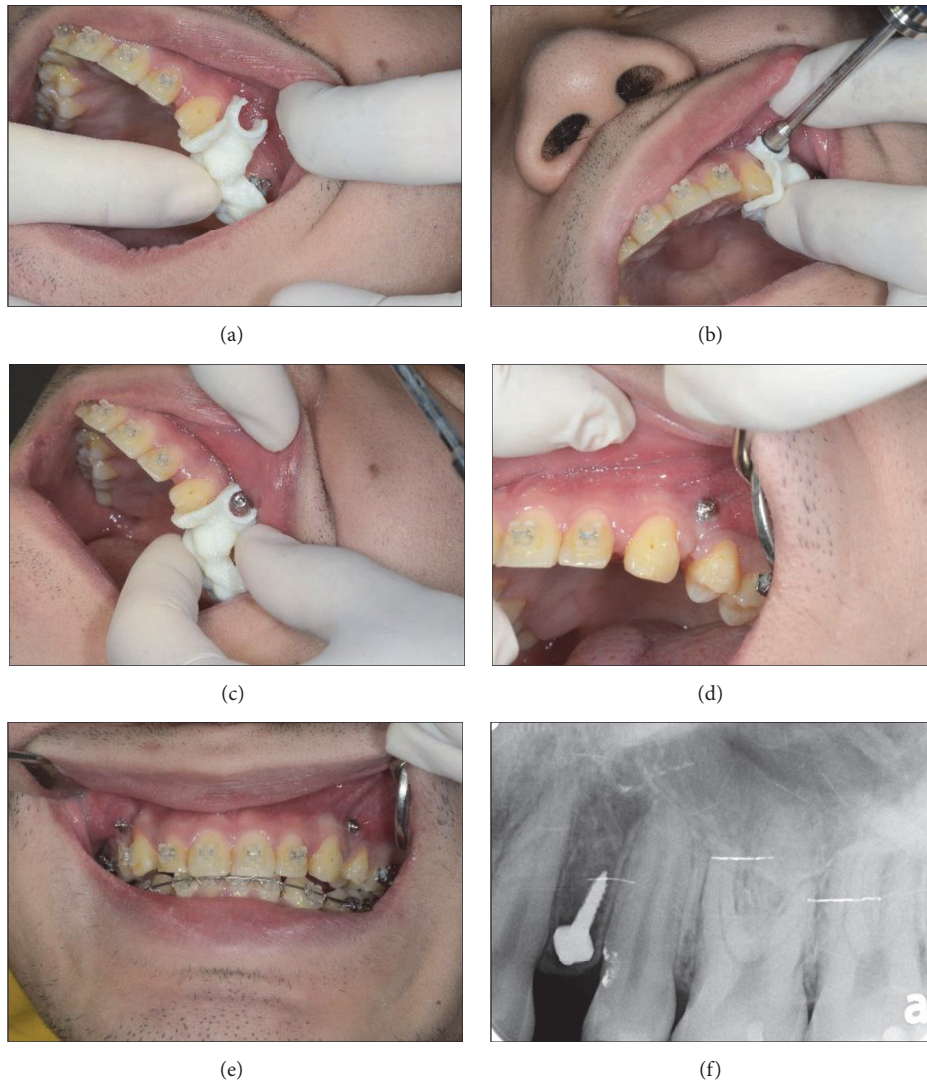


FIGURE 7: (a) The surgical templates were placed intraorally onto the teeth by a clinician; (b) to (e) showed the clinical application of the customized surgical template; (f) X-rays were taken after implantation to assess whether damage to the peripheral tissue occurred for assessing miniscrew stability.

TABLE 2: Gap size of the interfacial adaption test of right surgical template (unit: mm).

Section	Placement	Point					Average	SD
		1	2	3	4	5		
A	Canine	0.45	0.47	0.83	0.25	0.44	0.49	0.19
B	2nd Premolar	0.17	0.41	0.13	0.15	0.54	0.28	0.17
C	2nd Premolar/1st Molar	0.21	0.41	0.07	0.44	0.31	0.29	0.14
D	1st Molar	0.08	0.14	0.32	0.20	0.39	0.23	0.11
E	1st Molar	0.07	0.27	0.41	0.30	0.15	0.24	0.12
F	2nd Molar	0.21	0.20	0.05	0.46	0.43	0.27	0.15
Total average							0.30 ± 0.10	

pitch (parametrical relationship with macrothread pitch) in the cortical bone region can improve primary stability and enhance mechanical retention [16]. The microthread portion in the miniscrews must be precisely controlled to contact the cortical bone layer in the visual planning procedure,

that is, total lengths of microthread and smooth (sliding) portions below the screw head (3 mm) need to be larger than the cortical bone layer and soft tissue (mucosa) total thickness. In our clinical test case, that is, canine distal drive, the cortical bone layers/mucosa thicknesses at the left and

right buccal sites were 1.15 mm/1.1 mm and 1.53 mm/1.25 mm, respectively (Figure 2(a)). This case indicated that the miniscrew microthread can contact the cortical bone layer when the miniscrew head bottom is controlled to slightly touch the mucosa during insertion.

3DP in medical applications has been widely used in several broad categories, including the creation of customized surgical templates, implants, and anatomical models because of its medical product customization and personalization, cost-effectiveness, and design and manufacturing democratization. However, the FDM 3DP printer with 0.254 mm slicing additive manufacturing was used in this study. The 3DP mechanic must take into account the high resolution to meet the well-fitting template accuracy requirement. Otherwise, biocompatibility considerations, especially for the toxicity of 3DP material, must be tested before template fabrication. The patient may delay the overall orthodontic treatment time because the timing of producing the surgical template was about one week from reconstructing the patient image to complete the 3DP fabrication. Time-consuming surgical template production must be compressed when the surgical template is required for miniscrew placement.

A new method for integrating CBCT/laser scan image superimposition, CAD system, and 3DP techniques was developed in this study and applied to fabricate an accurate customized surgical template for orthodontic miniscrews. More clinical applications can be applied to verify the feasibility of the proposed method. For clinical consideration, this customized surgical template can be used for situations when molar intrusion/extrusion, molar uprighting, molar distalization, buccoversion/scissors bite, and molar mesial drive are to be performed. It is not applicable when there is no sufficient room for interradicular miniscrew placement or when extremely low maxillary sinus floor is observed. In addition, severely unstable occlusal surfaces of the anchor teeth can also be excluded when a surgical template is to be used.

Competing Interests

The authors declare that they have no competing interests.

Acknowledgments

This study is supported in part by NSC Project 100-2628-E-010-003-MY3 of the National Science Council, Taiwan.

References

- [1] S. Baumgaertel, "Temporary skeletal anchorage devices: the case for miniscrews," *American Journal of Orthodontics and Dentofacial Orthopedics*, vol. 145, no. 5, pp. 558–564, 2014.
- [2] M. Schätzle, R. Männchen, M. Zwahlen, and N. P. Lang, "Survival and failure rates of orthodontic temporary anchorage devices: a systematic review," *Clinical Oral Implants Research*, vol. 20, no. 12, pp. 1351–1359, 2009.
- [3] N. D. Kravitz and B. Kusnoto, "Risks and complications of orthodontic miniscrews," *American Journal of Orthodontics and Dentofacial Orthopedics*, vol. 131, no. 4, pp. S43–S51, 2007.
- [4] H. Liu, D.-X. Liu, G. Wang, C.-L. Wang, and Z. Zhao, "Accuracy of surgical positioning of orthodontic miniscrews with a computer-aided design and manufacturing template," *American Journal of Orthodontics and Dentofacial Orthopedics*, vol. 137, no. 6, pp. 728.e1–728.e10, 2010.
- [5] A. S. Felicita, "A simple three-dimensional stent for proper placement of mini-implant," *The International Journal of Adult Orthodontics & Orthognathic Surgery*, vol. 131, pp. 352–356, 2013.
- [6] T. Shyagali, N. Dungarwal, and A. Prakash, "A new stent for miniscrew implant placement," *Orthodontic Waves*, vol. 71, no. 4, pp. 134–137, 2012.
- [7] E. Y. Suzuki and B. Suzuki, "Accuracy of miniscrew implant placement with a 3-dimensional surgical guide," *Journal of Oral and Maxillofacial Surgery*, vol. 66, no. 6, pp. 1245–1252, 2008.
- [8] H. M. Kyung, H. S. Park, S. M. Bae, J. H. Sung, and I. B. Kim, "Development of orthodontic miniscrew implants for intraoral anchorage," *Journal of Clinical Orthodontics*, vol. 6, pp. 321–328, 2003.
- [9] S. H. Kyung, J. H. Choi, and Y. C. Park, "Miniscrew anchorage used to protract lower second molars into first molar extraction sites," *Journal of Clinical Orthodontics*, vol. 37, pp. 575–579, 2003.
- [10] N. Kitai, Y. Yasuda, and K. Takada, "A stent fabricated on a selectively colored stereolithographic model for placement of orthodontic mini-implants," *The International Journal of Adult Orthodontics & Orthognathic Surgery*, vol. 17, no. 4, pp. 264–266, 2002.
- [11] W. Martin, M. Heffernan, and J. Ruskin, "Template fabrication for a midpalatal orthodontic implant: technical note," *The International Journal of Oral & Maxillofacial Implants*, vol. 17, no. 5, pp. 720–722, 2002.
- [12] J.-E. Lim, H. L. Won, and S. C. Yoon, "Quantitative evaluation of cortical bone thickness and root proximity at maxillary interradicular sites for orthodontic mini-implant placement," *Clinical Anatomy*, vol. 21, no. 6, pp. 486–491, 2008.
- [13] P. M. Poggio, C. Incorvati, S. Velo, and A. Carano, "'Safe zones': a guide for miniscrew positioning in the maxillary and mandibular arch," *Angle Orthodontist*, vol. 76, no. 2, pp. 191–197, 2006.
- [14] C.-H. Moon, D.-G. Lee, H.-S. Lee, J.-S. Im, and S.-H. Baek, "Factors associated with the success rate of orthodontic miniscrews placed in the upper and lower posterior buccal region," *The Angle Orthodontist*, vol. 78, no. 1, pp. 101–106, 2008.
- [15] S. Suri, A. Utreja, N. Khandelwal, and S. K. Mago, "Craniofacial computerized tomography analysis of the midface of patients with repaired complete unilateral cleft lip and palate," *American Journal of Orthodontics & Dentofacial Orthopedics*, vol. 134, no. 3, pp. 418–429, 2008.
- [16] Y.-S. Lin, Y.-Z. Chang, J.-H. Yu, and C.-L. Lin, "Do dual-thread orthodontic mini-implants improve bone/tissue mechanical retention?" *Implant Dentistry*, vol. 23, no. 6, pp. 653–658, 2014.

Research Article

Fabrication of Novel Hydrogel with Berberine-Enriched Carboxymethylcellulose and Hyaluronic Acid as an Anti-Inflammatory Barrier Membrane

Yu-Chih Huang,¹ Kuen-Yu Huang,² Bing-Yuan Yang,³ Chun-Han Ko,³
and Haw-Ming Huang^{1,2,4}

¹School of Dentistry, College of Oral Medicine, Taipei Medical University, Taipei, Taiwan

²Graduate Institute of Biomedical Materials and Tissue Engineering, College of Biomedical Engineering, Taipei Medical University, Taipei, Taiwan

³School of Forestry and Resource Conservation, National Taiwan University, Taipei, Taiwan

⁴Graduate Institute of Biomedical Optomechanics, College of Biomedical Engineering, Taipei Medical University, Taipei, Taiwan

Correspondence should be addressed to Chun-Han Ko; chunhank@ntu.edu.tw and Haw-Ming Huang; hmm@tmu.edu.tw

Received 4 October 2016; Accepted 1 December 2016

Academic Editor: Jung-Wei Chen

Copyright © 2016 Yu-Chih Huang et al. This is an open access article distributed under the Creative Commons Attribution License, which permits unrestricted use, distribution, and reproduction in any medium, provided the original work is properly cited.

An antiadhesion barrier membrane is an important biomaterial for protecting tissue from postsurgical complications. However, there is room to improve these membranes. Recently, carboxymethylcellulose (CMC) incorporated with hyaluronic acid (HA) as an antiadhesion barrier membrane and drug delivery system has been reported to provide excellent tissue regeneration and biocompatibility. The aim of this study was to fabricate a novel hydrogel membrane composed of berberine-enriched CMC prepared from bark of the *P. amurense* tree and HA (PE-CMC/HA). In vitro anti-inflammatory properties were evaluated to determine possible clinical applications. The PE-CMC/HA membranes were fabricated by mixing PE-CMC and HA as a base with the addition of polyvinyl alcohol to form a film. Tensile strength and ultramorphology of the membrane were evaluated using a universal testing machine and scanning electron microscope, respectively. Berberine content of the membrane was confirmed using a UV-Vis spectrophotometer at a wavelength of 260 nm. Anti-inflammatory property of the membrane was measured using a Griess reaction assay. Our results showed that fabricated PE-CMC/HA releases berberine at a concentration of 660 $\mu\text{g}/\text{ml}$ while optimal plasticity was obtained at a 30 : 70 PE-CMC/HA ratio. The berberine-enriched PE-CMC/HA had an inhibited 60% of inflammation stimulated by LPS. These results suggest that the PE-CMC/HA membrane fabricated in this study is a useful anti-inflammatory berberine release system.

1. Introduction

An antiadhesion barrier is one of the essential requirements for maintaining health and protecting tissue from postsurgical complications. For example, an antiadhesion barrier membrane is essential after intra-abdominal surgery to prevent normally free-moving tissues from sticking together [1]. For successful dental implant surgery, it is important to maintain adequate alveolar ridge dimensions and it often requires guided bone regeneration (GBR). This surgical procedure

uses barrier membranes [2] that are often manufactured using expanded polytetrafluoroethylene (e-PTFE) [3, 4]. However, clinical and experimental studies have demonstrated that complications such as incomplete coverage or gingival recession can occur when this nonresorbable material is used for GBR [5–7]. Accordingly, bioresorbable polymeric membranes, such as polylactides and polyglycolides, were developed to replace nonresorbable membranes. The advantage of bioresorbable membranes is the elimination of the need for membrane removal giving the surgical procedure

greater time-effectiveness. However, it was reported that polymeric membranes are greatly associated with inflammatory reactions [8]. Collagen has been recently introduced as a GBR membrane material because it can overcome the disadvantages of previous nonresorbable polymeric membranes [9, 10]. However, the speed of collagen membrane degradation is a concern when fabricating barrier membranes [11].

Recently, several natural polymers have been used to fabricate hydrogel tissue barriers. Among these natural polymers, hyaluronic acid (HA) [12] and cellulose [13] are two ubiquitous and abundant biopolymers used for tissue engineering and regenerative medicine. To produce inexpensive GBR membranes that can be easily manipulated, carboxymethylcellulose (CMC) and HA were used. CMC is a polysaccharide based hydrogel that when incorporated with hydroxyapatite in a CMC-based hydrogel provides excellent tissue engineering function [14]. In 2013, Sagar et al. developed a nanohydroxyapatite/gelatin and chemically carboxymethylated chitin scaffold that enhanced osteoblastic activity and mineralization [15]. However, cellulose-based hydrogels lack good mechanical properties for clinical use [14].

Hyaluronic acid is a natural component found in abundance in the extracellular space [16] and load-bearing joints [17, 18] that has been reported to play an important role in wound healing and for retaining skin moisture [19]. In addition, it has anti-inflammatory, antioxidant, and antibacterial effects for the treatment of periodontal diseases [20]. However, the lubricating effect of HA is generally short-lived and the duration of its bioeffects is not predictable. To address these issues, a semisynthetic natural polymer obtained from the CMC combined with HA has been developed that can generate a new hybrid membrane for use as a tissue barrier [1, 14, 21]. The CMC can cross-link with HA by 1-(3-dimethylaminopropyl)-3-ethylcarbodiimide hydrochloride (EDC) with a various cross-linking degree [22]. This hybrid membrane can thus prolong the drug-release function. In addition, the issues of lack of mechanical property of CMC when it is applied alone can be solved.

Phellodendron amurense Rupr (*P. amurense*) is a Chinese herb used to treat different forms of inflammation and pain. Berberine is an active compound of *P. amurense* found in relatively high concentrations which has been shown to possess the antimicrobial [23] and anti-inflammatory [24] properties. While the bark of *P. amurense* contains abundant cellulose [25], whether or not berberine-enriched CMC can be fabricated from the bark of *P. amurense* has not yet been determined.

Accordingly, the aim of this study was to fabricate a novel hydrogel membrane composed of berberine-enriched CMC prepared from the bark of *P. amurense* and HA (PE-CMC/HA). In vitro anti-inflammatory property was evaluated to determine possible clinical applications.

2. Materials and Methods

2.1. Physical Property Tests of HA. The particle size distribution of the HA used in this study was determined using a particle size analyzer (90 Plus, Brookhaven Instruments

Corporation, Holtsville, NY, USA). Before testing, the HA sample was diluted to 0.25 mg/ml with purified water and stirred for 12 hrs. The pH value of the HA and PE-CMC/HA was measured at room temperature using a pH-meter (Model 6173, JENCO Quality Instrument, San Diego, USA). Thermal stability was detected using a thermogravimeter (TGA, TG 209 F3 Tarsus, Netzsch-Gerätebau GmbH, Germany). During the tests, 5 mg samples were heated from room temperature to 700°C at a rate of 10°/min. Thermal decomposition temperatures (T_d) and the residual weight were detected. Kinematic viscosity of the HA was tested using a viscometer (X-420, Cannon Instrument Co., PA, USA). 40 mg samples were added to analytical grade water to bring the concentration of each solution to 0.5 mg/ml. After magnetic stirring for 1 hour, the kinematic viscosity of the test HA was read with a unit of centistokes (cSt).

2.2. Cytotoxicity Test of HA Used in This Study. Testing for cytotoxicity was performed according to international standard ISO10993-5. NIH 3T3 and RAW264.7 macrophage cell lines were used to test the cytotoxicity of the HA and PE-CMC/HA membranes. For HA testing, NIH-3T3 fibroblast cells were seeded onto Petri dishes at a density of 10,000 cells/ml. Dulbecco's modified Eagle's medium (DMEM, Gibco, Grand Island, NY, USA) supplemented with L-glutamine and 10% fetal bovine serum was used as culture medium. The cells were incubated at 37°C in 5% CO₂ at 100% humidity. The NIH-3T3 cells cultured with a 2% dimethyl sulfoxide (DMSO, Sigma-Aldrich, St. Louis, MO, USA) was used for a positive control while the cells cultured with DMEM alone were used for negative control. After coculturing with HA for 24 hours, cell viability was determined using the MTT method. Absorbance was measured at 570/690 nm wavelengths using a microplate reader (Model 2020, Anthos Labtec Instruments, Eugendorf, Wals, Austria).

2.3. PE-CMC Preparation. The PE-CMC was prepared following a modified technique from a previous study [26]. The crude *P. amurense* bark extracts containing a high content of berberine were prepared as per the previous report. Then the residue pomace was dried, ground into powder, immersed in 5% NaOH (Fisher Scientific, Pittsburgh, PA, USA) for 2 hours at room temperature, and then heated to 90°C in 10% NaOH for 4 hours. The NaClO (Acros Organics, Geel, Belgium): H₂O₂ (Acros Organics) = 3 : 4 was used to bleach the substrate and then washed with fresh water. An air suction filler was used to further dry the substrate for 2 hours. The substrate was alkalinized at 30°C for 60 min and etherified at 70°C for 150 min in 85% ethanol. After the substrate was cooled, it was washed twice with 75% alcohol and an air suction filler was used to obtain the pure CMC substrate. Finally, a freeze-drying machine was used for 3 hours to obtain the dry PE-CMC powder.

2.4. CMC/HA and PE-CMC/HA Membrane Fabrication. The PE-CMC/HA membrane was composed of a PE-CMC and HA base with Polyvinyl alcohol (PVA, Sigma-Aldrich) to form a film, TWEEN80 (MERU Chemical, Taipei, Taiwan) for emulsifying. *Sapindus mukorossi* seed-extracted oil was

added for lubrication. The sodium hyaluronic acid (M.W: 2.6×10^6 Da) was purchased from MERU Chemical. The PVA and TWEEN80 were commercially available from Sigma-Aldrich and MERU Chemical, respectively. First, the PVA was dissolved in distilled water at a concentration of 0.5 g/mL at 121°C for 30 min. The PE-CMC (10 mg/mL), HA (30 mg/mL), TWEEN80, seed oil, and berberine-enriched CMC were added and mixed with a magnetic stirrer. When thoroughly mixed, 3 ml of the mixture was moved to a round mold 60 mm in diameter and 15 mm in depth. The mold was then put into an oven at 37°C for 3 hours to form a dried membrane. In this study, CMC/HA fabricated using commercialized CMC (Sigma-Aldrich) and HA using the same method mentioned above was used as control group.

2.5. Mechanical Tests of the Membrane. Before the test, the membrane was cut into a 15 × 20 mm rectangle. Mechanical tests of the PE-CMC/HA and CMC/HA membranes with various CMC:HA ratios (30:70, 50:50, and 60:40) were performed using a universal testing machine (AGS-1000D, Shimadzu, Tokyo, Japan) according to ASTM D 638-08 regulations. Briefly, the samples were fixed 5 mm from both widths. The crosshead speed was set at 30 mm/min and a load was applied until the sample fractured. Tensile strength was determined as the maximum value of the force.

2.6. Morphological Features of the Membrane. To enhance morphological features, PE-CMC/HA and CMC/HA membrane surfaces were given a thin coating of palladium gold (IB-2, Hitachi Ltd., Chiyoda, Tokyo, Japan). Ultrastructure images of the samples were observed using scanning electron microscopy (SEM) (Model 2400; Hitachi, Tokyo, Japan).

2.7. Berberine Detection. Berberine content was determined using a NanoDrop UV-Vis Spectrophotometer (ND-1000, Thermo Scientific, Waltham, MA, USA) at 260 nm wavelength as in a previous study [27]. The calibration curve of the berberine standard (B3251, Sigma-Aldrich) was determined from six concentration points over the range of concentrations (37.25 to 1000 µg/mL) with an *R* value greater than 0.99. Before detection, the membranes were dissolved in distilled water to create a solution with a concentration of 500 µg/mL. The amounts of berberine released from the tested membranes were calculated from the standard curves.

2.8. Anti-Inflammatory Test of the Membrane. To test the anti-inflammatory properties of the CMC/HA and PE-CMC/HA membrane, RAW264.7 macrophage cells were seeded into a 96-well plate at a concentration of 4×10^5 cells/mL and cultivated in an incubator at 37°C and 5% CO₂. After incubating for 24 hours, cells were stimulated with 1 µg/mL of lipopolysaccharide (LPS, Sigma-Aldrich) from *Escherichia coli* strain 055:B5 and HA/CMC membrane extracted medium. The N-nitro-L-arginine-methyl ester (L-NAME, Sigma-Aldrich) with a concentration 1 mM was used as a positive control. The nitric oxide concentration produced by RAW 264.7 cells was determined through Griess assay. Briefly, an equal volume of Griess reagent (N5751, Sigma) was

mixed with the culture supernatant and color development was measured at 530 nm using a microplate reader (EZ Read 400, Biochrom, Holliston, MA, USA). Anti-inflammatory activity was presented in terms of NO production inhibition percentage.

2.9. Statistical Analysis. For cell viability tests, mean values and standard deviations of each measurement were recorded. To evaluate the changes between the samples and control, one-way analysis of variance (ANOVA) (SPSS Inc., Chicago, IL, USA) with Tukey's post hoc was performed. A *p* value lower than 0.05 was considered statistically significant.

3. Results

3.1. Physical Properties of HA. The HA particles had two populations in size. As shown in Figure 1, HA particles sizes are concentrated at 100–250 µm and 600–900 µm. The kinematic viscosity of HA increases as a function of concentration (Figure 1(b)). When the concentration of HA increased from 0.1 to 0.8 mg/ml, the kinematic viscosity of the HA increased from 2.93 to 36.31. Figure 1(c) illustrates the thermography of the HA used in this study. The decomposition temperature (*T_d*) of test HA was 71.75°C. The residual weight was 25.82% at 700°C.

3.2. Cytotoxicity Test of HA Used in This Study. Figure 2 shows the results of cytotoxic tests of HA used in this study. The viability of NIH-3T3 cells cultured with 2% DMSO was significantly reduced by 20%. Growth analysis of NIH-3T3 cells cultured with HA with concentrations up to 0.4 mg/ml showed no relevant viability inhibition. That is, under the given conditions no cytotoxic substrates were released from the HA material.

3.3. Berberine Detection. The UV-Vis spectrum of standard berberine is shown in Figure 3(a). There are two absorption bands at around 250 and 350 nm and a weak band at about 430 nm. The shape of the absorption spectrum of the *P. amurense* bark extract is similar to berberine standard. The sample also exhibited two absorption bands at around 250 and 350 nm. However, the band at about 430 nm was not significant. The 250 and 350 nm bands can also be detected in fabricated PE-CMC/HA as with *P. amurense* extract (Figure 3(b)). Figure 4 shows the quantitative results of UV detection at a wavelength of 260 nm. When the fabricated PE-CMC/HA membrane was dissolved in water, significant berberine release was confirmed at a concentration of 660 µg/ml.

3.4. Mechanical Tests. Figure 5 shows the mechanical tests of the CMC/HA membranes fabricated in this study. The membranes exhibited a critical plastic characteristic. The ultimate strength of the CMC/HA decreases when increasing the amount of HA. For samples mixed to a ratio of 30:70, 50:50, and 60:40, the ultimate strengths were 1.57 ± 0.37 , 2.06 ± 0.13 , and 2.36 ± 0.13 kgf, respectively. In contrast, the ultimate displacement for the CMC/HA increases when

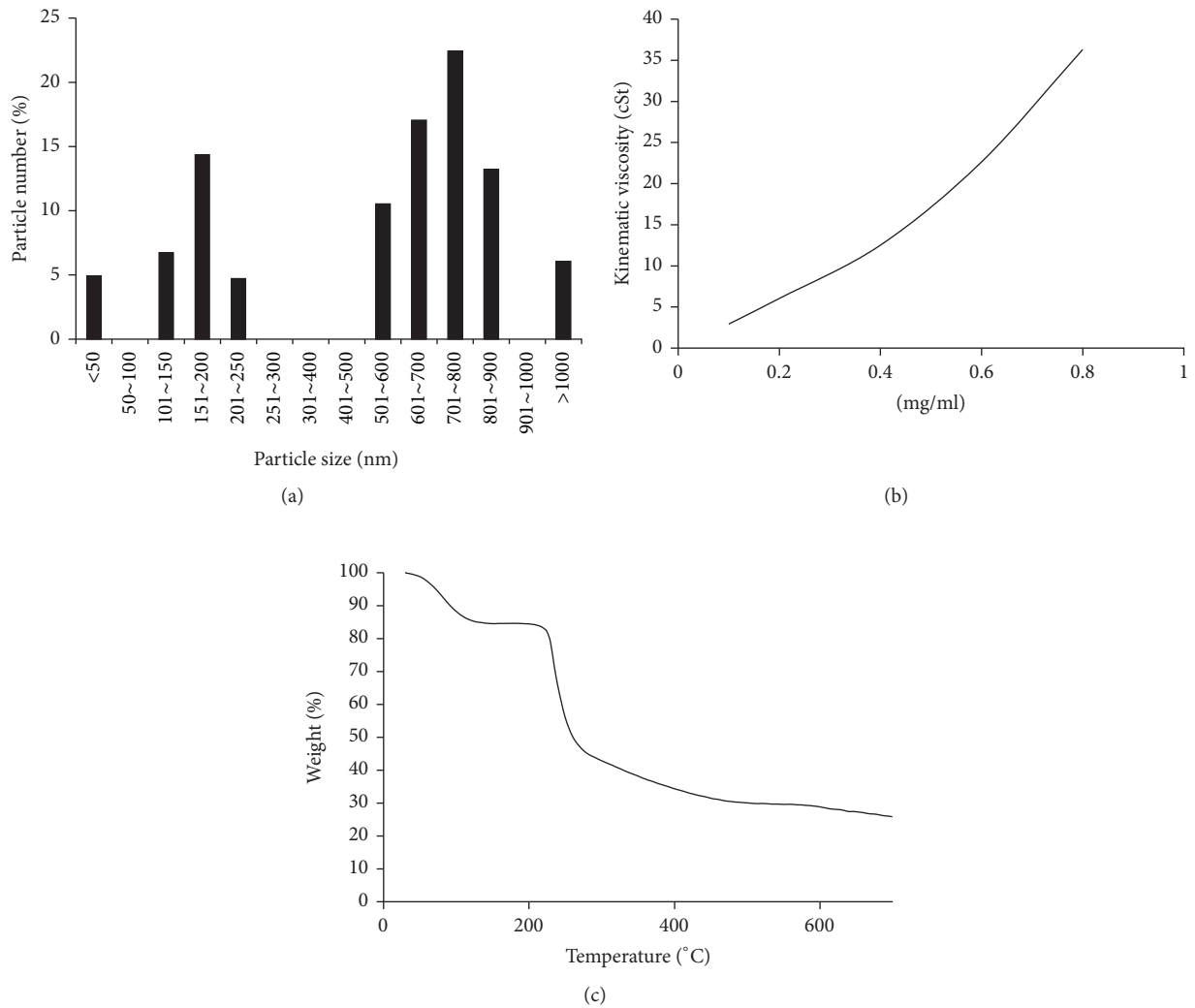


FIGURE 1: HA physical properties. (a) HA particle diameter distributions. (b) HA kinematic viscosity. (c) HA TGA patterns.

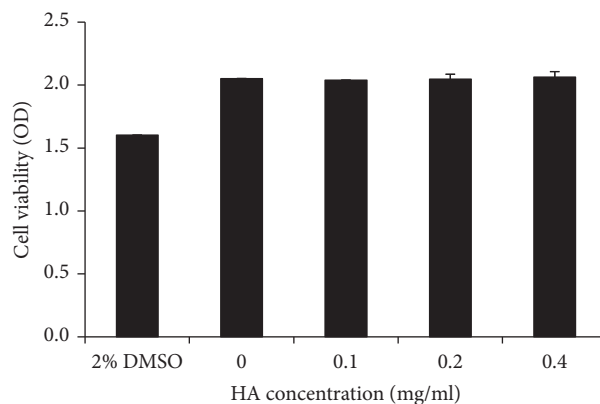


FIGURE 2: Cytotoxicity tests for the HA used in this study.

the HA amount was increased. The ultimate displacement readings for the 30:70, 50:50, and 60:40 CMC/HA are 12.04 ± 2.14 , 11.78 ± 1.22 , and 10.76 ± 0.68 mm, respectively. The addition of *P. amurensis* extract reduces both ultimate strength and elongation of the membrane. The ultimate

strength and displacement of the PE-CMC/HA membrane were 1.42 ± 0.32 kgf and 11.75 ± 1.57 mm, respectively. Considering the plasticity, deformation capability is more important than strength for the purpose of this study. Meanwhile, the HA amount can have a biological effect on wound

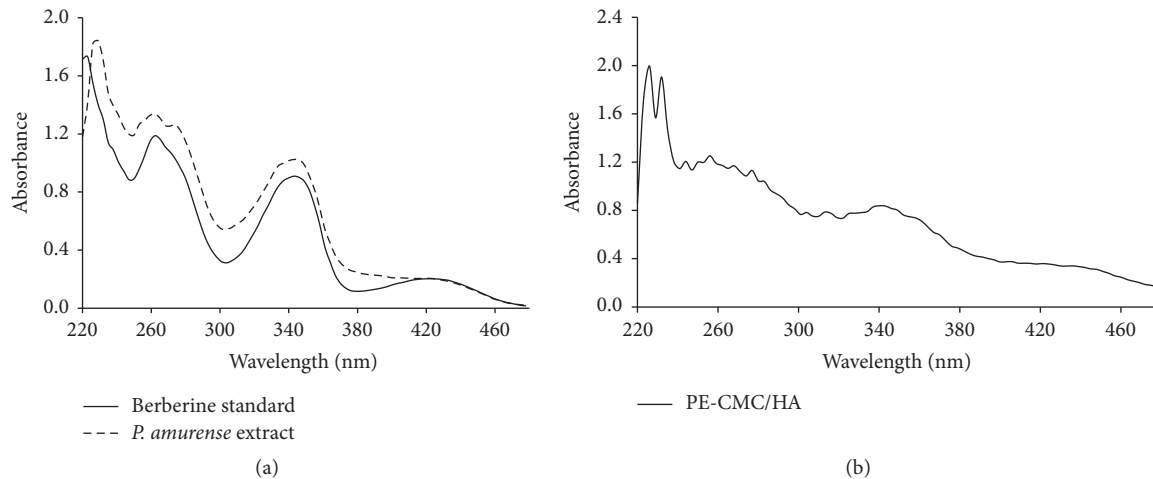


FIGURE 3: UV-Vis absorption spectra of (a) berberine standard, *P. amurensis* extract, and (b) the fabricated PE-CMC/HA membrane.

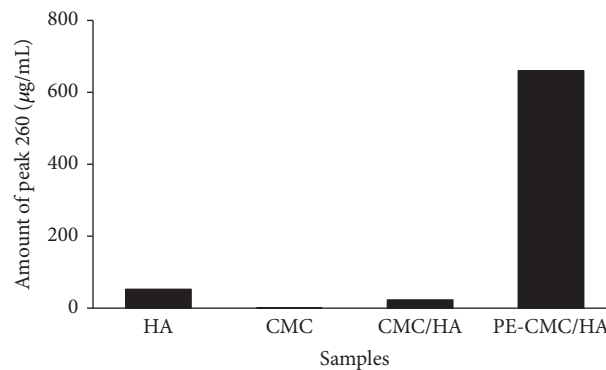


FIGURE 4: UV-Vis detection at a wavelength of 260 nm.

healing. Since the HA amount has a markedly positive effect on membrane plasticity, a membrane incorporating 70 wt% HA was used for fabricating the PE-CMC/HA used in the following biofunction tests.

3.5. Surface Topographies of the Membrane. SEM images of the fabricated CMC/HA and PE-CMC/HA samples revealed different surface topographies. The 30:70 CMC/HA sample was porous with any uniformly shaped holes observed (Figure 6(a)). For the 50:50 CMC/HA sample, the surface porosity was significantly lower (Figure 6(b)). Interestingly, the 60:40 CMC/HA sample is a nonporous material. Only the 60:40 CMC/HA sample had a smooth, planar texture (Figure 6(c)). The porosity of the PE-CMC/HA surface was also observable (Figure 6(d)). However, the holes were irregular in shape and significantly larger in pore size than those of CMC/HA samples.

3.6. Anti-Inflammatory Test. As shown in Figure 7, when the cell was treated with LPS (1 µg/ml), obvious morphological changes were found. Furthermore, the cells cultured with CMC-HA and PE-CMC/HA did not have altered morphological changes due to LPS treatment. However, CMC-HA and PE-CMC/HA significantly affected the NO release of the LPS-

treated cells. The NO release of the sample was normalized by comparing the measured data to the untreated sample. Significant reductions in NO release (8.56%) were noted in the L-NAME group when compared to the blank control (Figure 8). That is, the inhibition ratio of NO release for L-NAME was 91.44%. When the LPS loaded RAW 264.7 cells were treated with the composite fabricated from commercialized CMC and HA the NO release was reduced to 54.11%. When *P. amurensis* extract was added to the fabricated PE-CMC/HA and used in culture with the LPS loaded RAW 264.7 cells, the detected NO was decreased to 39.73% compared to the blank control.

4. Discussion

The preclinical evaluation demonstrated that HA/CMC is nontoxic, nonmutagenic, nonimmunogenic, nonirritating, and nonpyrogenic [28]. A previous study indicated that HA/CMC did not induce an inflammatory cytokine response [29]. Thus HA/CMC can be not only an antiadhesive material but also a material for drug release. Since infection is the major reason for GBR membrane failure in clinical application [30], developing GBR membranes that can perform localized drug delivery to prevent infection is an important

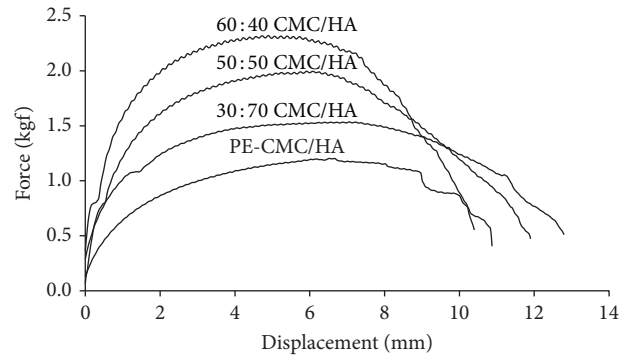


FIGURE 5: Mechanical tests of the PE-CMC/HA and CMC/HA membranes at various mix ratios.

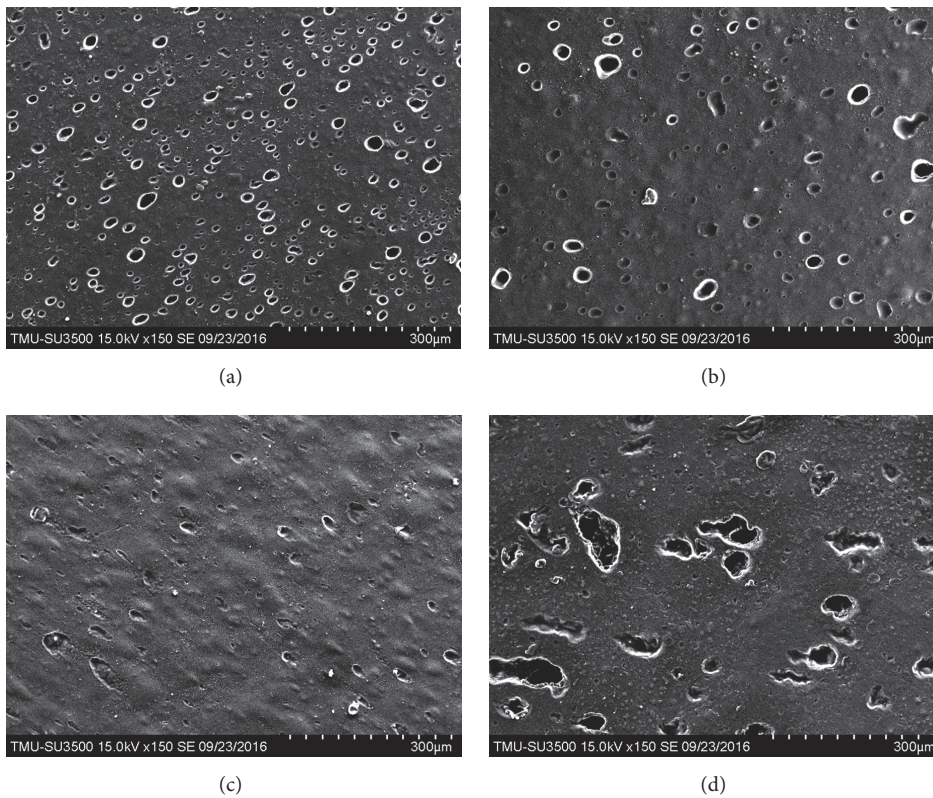


FIGURE 6: Scanning electron microscopy (SEM) images of the CMC/HA membranes surface at various mix ratios: (a) 30 : 70, (b) 50 : 50, and (c) 60 : 40. (d) shows a topographical image of the fabricated PE-CMC/HA surface.

biomaterials engineering issue. In 2012, Epstein-Barash et al. fabricated a hydrogel by cross-linking CMC and HA as a protein/peptide release system [22]. For clinical usage, this hybrid hydrogel has several advantages, such as slow protein release, ease of handling, and the ability to be delivered via minimally invasive means. In addition, fabrication of such a CMC/HA hydrogel does not require chemical additives or a source of energy source.

The main bioactive component of *P. amurensis* is berberine. In this study, the extract of *P. amurensis* was added to the fabricated PE-CMC/HA as a released substrate. As shown in Figure 4, the berberine-specific absorbance band at 260 nm

was detected as in a previous study [31]. This result indicates that our PE-CMC/HA membrane can operate as a berberine-released system. It is well known that berberine exhibits specific pharmacological properties, such as being antimicrobial, antiparasitic, anti-inflammatory, and anticarcinogenic properties [23, 24, 27]. As shown in Figure 8, the fabricated PE-CMC/HA significantly reduced inflammatory cytokine (NO) release. According to this result, it is reasonable to suggest that the current PE-CMC/HA membrane can be used as an antibacterial and anti-inflammatory drug-release system.

It has been reported that the strength of a membrane is determined by the size, shape, and density of the structure's

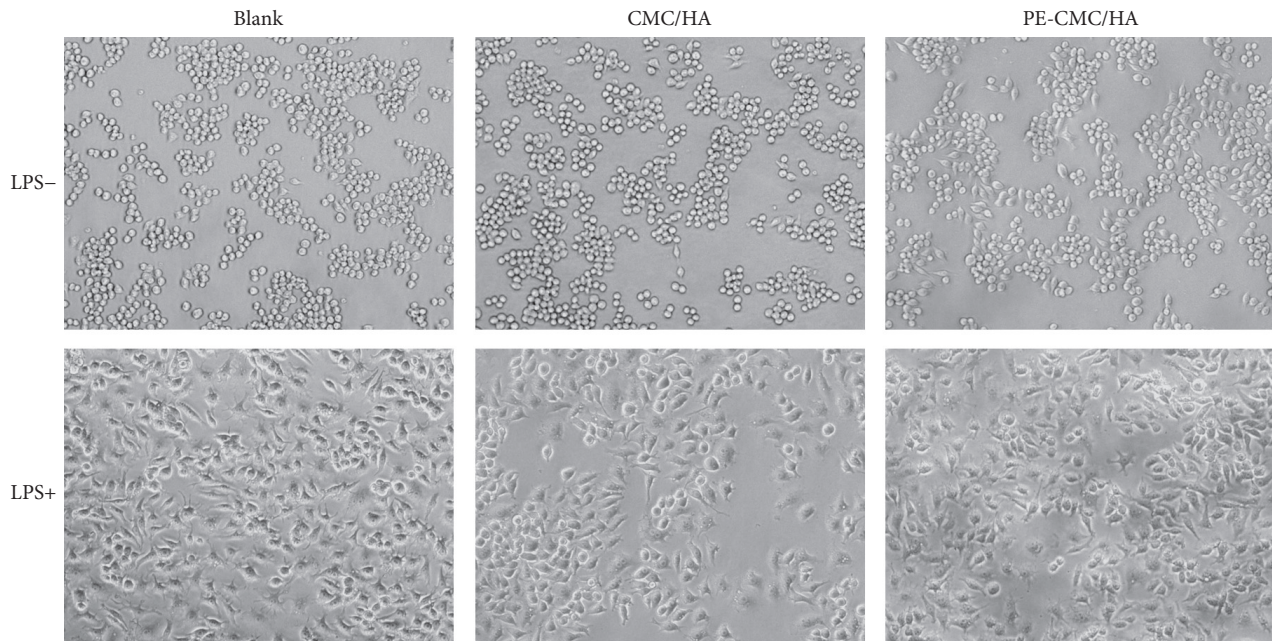


FIGURE 7: Microscopy of LPS-treated and untreated RAW 264.7 cells. The addition of CMC-HA and PE-CMC/HA did not alter the morphology of the cells.

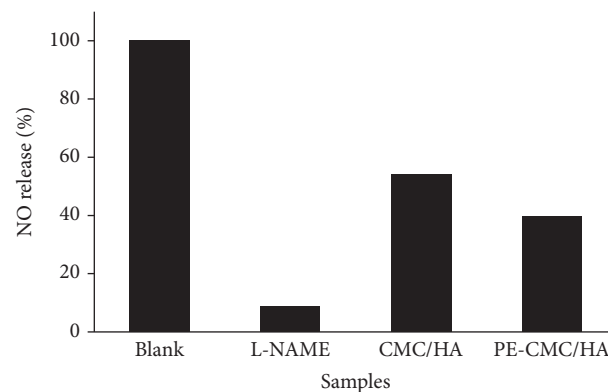


FIGURE 8: Normalized NO release of the LPS-induced RAW 264.7 cells. The fabricated CMC-HA and PE-CMC/HA tended to reduce NO release.

micropores/nanopores [32]. Since the strength of a membrane decreases as the size and porosity of the pores increase, it is not surprising that the mechanical property of current CMC/HA membrane is strongly correlated to the CMC-to-HA mix ratio (Figure 5). From Figure 5, we can see that higher CMC concentrations result in a higher ultimate membrane strength. This is because the increase of the CMC ratio tends to decrease the porosity of the membrane (Figure 6). This result confirmed a previous finding that cellulose-based hydrogels lack good mechanical proprieties for clinical use [14]. In contract, the amount of HA has a markedly positive effect on the plasticity of the membrane (Figure 5). This is because the HA is a highly viscous gel (Figure 1(b)) allowing the water-dissolved PE-CMC/HA fabricated in this study that can be injected into tissues and coating to follow the contours of underlying tissues.

According to the specific characteristic of the PE-CMC/HA, the membrane can be used for extensive biomedical applications. For example, the fabricated PE-CMC/HA membrane has potential as a candidate for treating vaginal infections. The characteristics of the vaginal epithelium change depending on variations in the concentration of estrogenic and progestational hormones. During the fertile period, the vagina is soft and elastic due to the balance mechanism of the vaginal epithelium that maintains appropriate hydration and lubrication. In some cases, such as during lactation, menopause, after pregnancy, with the use of oral contraceptives, or when under stress, this balance may be disturbed. In such situations, signs of vaginal dryness, burning sensations, or itching may be observed due to insufficient vaginal lubrication. It is well known that the major ability of HA is to hold water and retain a balanced amount of moisture

[33]. As shown in Figure 6, the ultrastructure images of the PE-CMC/HA membrane fabricated in this study have a porous structure. Such porosity moisturizes the membrane. In addition, HA exhibits a number of healing properties, including the facilitation of cell migration and differentiation during tissue formation and repair [33]. Thus, it is efficient and safe to use HA to treat vaginal dryness in postmenopausal women [34].

However, HA is quickly degraded by enzymes and absorption by tissue. This means HA cannot be used for long-term treatment. Mixing HA with CMC not only delays the absorption of HA but also prolongs the duration of the antimicrobial and anti-inflammatory effects of HA and berberine [35, 36]. Park et al. (2011) indicated that the peptide/protein release profiles of the CMC/HA can be easily tuned by adjusting its cross-linker density [21]. In this study, cross-linker was not added during fabrication of the PE-CMC/HA. Understanding how the degree of cross-linking affects the release efficiency of berberine and the mechanical properties of the membrane were limitations of this study.

5. Conclusion

In conclusion, the PE-CMC/HA membrane fabricated in this study is a berberine release system to provide antibacterial and anti-inflammatory functions. The excellent viscosity of PE-CMC/HA makes it a possible candidate for manufacturing hydrogel for treating infections of disease.

Competing Interests

The authors have declared that there is no conflict of interests.

Authors' Contributions

Haw-Ming Huang and Chun-Han Ko contributed equally to this work.

Acknowledgments

Authors would like to express their sincere appreciation to Lake Forest Co., Guizhou, China, which provided the bark of *P. amurense* tree and the great support of the research resources.

References

- [1] L. Picaud, B. Thibault, E. Mery et al., "Evaluation of the effects of hyaluronic acid-carboxymethyl cellulose barrier on ovarian tumor progression," *Journal of Ovarian Research*, vol. 7, no. 1, article no. 40, 2014.
- [2] J. Liu and D. G. Kerns, "Mechanisms of guided bone regeneration: a review," *The Open Dentistry Journal*, vol. 8, supplement 1, pp. 56–65, 2014.
- [3] D. Buser, K. Dula, U. Belser, H. P. Hirt, and H. Berthold, "Localized ridge augmentation using guided bone regeneration. 1. Surgical procedure in the maxilla," *The International Journal of Periodontics and Restorative Dentistry*, vol. 13, no. 1, pp. 29–45, 1993.
- [4] W. Becker, C. Dahlin, U. Lekholm et al., "Five-year evaluation of implants placed at extraction and with dehiscences and fenestration defects augmented with ePTFE membranes: results from a prospective multicenter study," *Clinical implant dentistry and related research*, vol. 1, no. 1, pp. 27–32, 1999.
- [5] E. E. Machtei, "The effect of membrane exposure on the outcome of regenerative procedures in humans: a meta-analysis," *Journal of Periodontology*, vol. 72, no. 4, pp. 512–516, 2001.
- [6] M. Simion, M. Baldoni, P. Rossi, and D. Zaffe, "A comparative study of the effectiveness of e-PTFE membranes with and without early exposure during the healing period," *The International Journal of Periodontics and Restorative Dentistry*, vol. 14, no. 2, pp. 166–180, 1994.
- [7] N. U. Zitzmann, R. Naef, and P. Schärer, "Resorbable versus nonresorbable membranes in combination with Bio-Oss for guided bone regeneration," *International Journal of Oral & Maxillofacial Implants*, vol. 12, no. 6, pp. 844–852, 1997.
- [8] A. Piattelli, A. Scarano, F. Coraggio, and S. Matarasso, "Early tissue reactions to polylactic acid resorbable membranes: a histological and histochemical study in rabbit," *Biomaterials*, vol. 19, no. 10, pp. 889–896, 1998.
- [9] H.-L. Wang and W. J. Carroll, "Guided bone regeneration using bone grafts and collagen membranes," *Quintessence International*, vol. 32, no. 7, pp. 504–515, 2001.
- [10] D. Rothamel, F. Schwarz, A. Sculean, M. Herten, W. Scherbaum, and J. Becker, "Biocompatibility of various collagen membranes in cultures of human PDL fibroblasts and human osteoblast-like cells," *Clinical Oral Implants Research*, vol. 15, no. 4, pp. 443–449, 2004.
- [11] K. W. Owens and R. A. Yukna, "Collagen membrane resorption in dogs: a comparative study," *Implant Dentistry*, vol. 10, no. 1, pp. 48–58, 2001.
- [12] H. Geckil, F. Xu, X. Zhang, S. Moon, and U. Demirci, "Engineering hydrogels as extracellular matrix mimics," *Nanomedicine*, vol. 5, no. 3, pp. 469–484, 2010.
- [13] R. M. A. Domingues, M. E. Gomes, and R. L. Reis, "The potential of cellulose nanocrystals in tissue engineering strategies," *Biomacromolecules*, vol. 15, no. 7, pp. 2327–2346, 2014.
- [14] D. Pasqui, P. Torricelli, M. De Cagna, M. Fini, and R. Barbucci, "Carboxymethyl cellulose—hydroxyapatite hybrid hydrogel as a composite material for bone tissue engineering applications," *Journal of Biomedical Materials Research Part A*, vol. 102, no. 5, pp. 1568–1579, 2014.
- [15] N. Sagar, A. K. Pandey, D. Gurbani et al., "In-vivo efficacy of compliant 3D nano-composite in critical-size bone defect repair: a six month preclinical study in rabbit," *PLoS ONE*, vol. 8, no. 10, Article ID e77578, 2013.
- [16] P. Korn, M. C. Schulz, V. Hintze et al., "Chondroitin sulfate and sulfated hyaluronan-containing collagen coatings of titanium implants influence peri-implant bone formation in a minipig model," *Journal of Biomedical Materials Research—Part A*, vol. 102, no. 7, pp. 2334–2344, 2014.
- [17] C. R. Correia, L. S. Moreira-Teixeira, L. Moroni et al., "Chitosan scaffolds containing hyaluronic acid for cartilage tissue engineering," *Tissue Engineering—Part C: Methods*, vol. 17, no. 7, pp. 717–730, 2011.
- [18] P. Dahiya and R. Kamal, "Hyaluronic acid: a boon in periodontal therapy," *North American Journal of Medical Sciences*, vol. 5, no. 5, pp. 309–315, 2013.
- [19] J. Kablik, G. D. Monheit, L. Yu, G. Chang, and J. Gershkovich, "Comparative physical properties of hyaluronic acid dermal fillers," *Dermatologic Surgery*, vol. 35, pp. 302–312, 2009.

- [20] H. Jentsch, R. Pomowski, G. Kundt, and R. Göcke, "Treatment of gingivitis with hyaluronan," *Journal of Clinical Periodontology*, vol. 30, no. 2, pp. 159–164, 2003.
- [21] J. S. Park, J. H. Lee, C. S. Han, D. W. Chung, and G. Y. Kim, "Effect of hyaluronic acid-carboxymethylcellulose solution on perineural scar formation after sciatic nerve repair in rats," *Clinics in Orthopedic Surgery*, vol. 3, no. 4, pp. 315–324, 2011.
- [22] H. Epstein-Barash, C. F. Stefanescu, and D. S. Kohane, "An in situ cross-linking hybrid hydrogel for controlled release of proteins," *Acta Biomaterialia*, vol. 8, no. 5, pp. 1703–1709, 2012.
- [23] C.-L. Kuo, C.-W. Chi, and T.-Y. Liu, "The anti-inflammatory potential of berberine in vitro and in vivo," *Cancer Letters*, vol. 203, no. 2, pp. 127–137, 2004.
- [24] Z.-B. Yi, Y. Yu, Y.-Z. Liang, and B. Zeng, "Evaluation of the antimicrobial mode of berberine by LC/ESI-MS combined with principal component analysis," *Journal of Pharmaceutical and Biomedical Analysis*, vol. 44, no. 1, pp. 301–304, 2007.
- [25] M. A. K. Azad, S. Yokota, F. Ishiguri, and N. Yoshizawa, "Plant regeneration from mesophyll protoplasts of a medicinal plant, *Phellodendron amurense* Rupr.," *In Vitro Cellular & Developmental Biology—Plant*, vol. 42, no. 6, pp. 502–507, 2006.
- [26] P. Rojsanga, W. Gritsanapan, and L. Suntorasuk, "Determination of berberine content in the stem extracts of *Coscinium fenestratum* by TLC densitometry," *Medical Principles and Practice*, vol. 15, no. 5, pp. 373–378, 2006.
- [27] M. S. Díaz, M. L. Freile, and M. I. Gutiérrez, "Solvent effect on the UV/Vis absorption and fluorescence spectroscopic properties of berberine," *Photochemical and Photobiological Sciences*, vol. 8, no. 7, pp. 970–974, 2009.
- [28] J. W. Burns, M. J. Colt, L. S. Burgees, and K. C. Skinner, "Preclinical evaluation of Seprafilm bioresorbable membrane," *The European Journal of Surgery. Supplement*, vol. 577, pp. 40–48, 1997.
- [29] K. Uchida, K. Otake, M. Inoue et al., "Bacteriostatic effects of hyaluronan-based bioresorbable membrane," *Surgical Science*, vol. 2, no. 9, pp. 431–436, 2011.
- [30] J. Xue, M. He, Y. Niu et al., "Preparation and in vivo efficient anti-infection property of GTR/GBR implant made by metronidazole loaded electrospun polycaprolactone nanofiber membrane," *International Journal of Pharmaceutics*, vol. 475, no. 1-2, pp. 566–577, 2014.
- [31] G. Srinivasan, K. Unnikrishnan, A. Rema Shree, and I. Balachandran, "HPLC estimation of berberine in *Tinospora cordifolia* and *Tinospora sinensis*," *Indian Journal of Pharmaceutical Sciences*, vol. 70, no. 1, pp. 96–99, 2008.
- [32] Y. Liu and X. Chen, "Mechanical properties of nanoporous graphene membrane," *Journal of Applied Physics*, vol. 115, no. 3, Article ID 034303, 2014.
- [33] J. Necas, L. Bartosikova, P. Brauner, and J. Kolar, "Hyaluronic acid (hyaluronan): a review," *Veterinarni Medicina*, vol. 53, no. 8, pp. 397–411, 2008.
- [34] J. Chen, L. Geng, X. Song et al., "Evaluation of efficacy and safety of Hyaluronic acid vaginal gel (Hyalofemme) for improvement of vaginal dryness A multicenter, randomized, open, positive and parallel controlled clinical trial," *The Journal of Sexual Medicine*, vol. 10, no. 6, pp. 1575–1584, 2013.
- [35] M. Yamamoto, N. Endo, M. Ito et al., "Novel polysaccharide-derived hydrogel prevents perineural adhesions in a rat model of sciatic nerve adhesion," *Journal of Orthopaedic Research*, vol. 28, no. 3, pp. 284–288, 2010.
- [36] S. Işık, S. Öztürk, S. Gürses et al., "Prevention of restrictive adhesions in primary tendon repair by HA-membrane: experimental research in chickens," *British Journal of Plastic Surgery*, vol. 52, no. 5, pp. 373–379, 1999.

Research Article

UV Photofunctionalization Effect on Bone Graft in Critical One-Wall Defect around Implant: A Pilot Study in Beagle Dogs

Min-Young Kim,¹ Hyunmin Choi,¹ Jae-Hoon Lee,¹ Jee-Hwan Kim,¹ Han-Sung Jung,² Jae-Hong Kim,³ Young-Bum Park,¹ and Hong-Seok Moon¹

¹*Department of Prosthodontics, Oral Science Research Center, BK21 PLUS Project, Yonsei University College of Dentistry, Seoul, Republic of Korea*

²*Division in Anatomy and Developmental Biology, Department of Oral Biology, Oral Science Research Center, BK21 PLUS Project, Yonsei University College of Dentistry, Seoul, Republic of Korea*

³*Department of Dental Technology, School of Medical and Public Health, Kyungdong University, Wonju, Gangwon-do, Republic of Korea*

Correspondence should be addressed to Hong-Seok Moon; hsm5@yuhs.ac

Received 19 August 2016; Revised 3 November 2016; Accepted 1 December 2016

Academic Editor: Wei-Jen Chang

Copyright © 2016 Min-Young Kim et al. This is an open access article distributed under the Creative Commons Attribution License, which permits unrestricted use, distribution, and reproduction in any medium, provided the original work is properly cited.

The purpose of this study was to compare and evaluate, through histomorphometric and radiological analysis, the effects of UV photofunctionalization on an implant placed over a critical defect area with and without a bone graft. Four female beagle dogs were first divided into control and bone graft groups. Each group was then subdivided into UV-treated and UV-untreated groups. The mandibular premolars in each dog were extracted. 12 weeks after extraction, implants were placed according to the condition of each group. Four and 12 weeks after implantation on left and right mandible, the dogs were sacrificed. The specimens were prepared for histomorphometric and micro-computed tomographic analysis. In both 4-week and 12-week groups, UV-treated implant surfaces showed better osseointegration than SA implant surfaces. Also, with implant surfaces placed over the critical defect with bone graft, UV photofunctionalization increased bone-to-implant contact (BIC) and new bone formation at the initial stage (4 weeks). Based on the results of this study, it can be suggested that UV photofunctionalization on the surface of implants placed over large critical defects with bone graft aids initial osseointegration and osteogenesis.

1. Introduction

In modern implant dentistry, implant therapy is known as the most effective treatment for edentulous patient and is regarded as the first treatment of choice for missing teeth. The success of dental implants depends on how directly new bone formation occurs on titanium surface after implant placement [1]. The initial amounts of osseointegration and osteogenesis are crucial factors in the success rate of implant therapy [2, 3]. In recent studies, Ogawa et al. researched the effects of UV photofunctionalization on titanium surface and concluded that conversion of implant surface from bioinert to bioactive yielded better osseointegration and osteogenesis on titanium surface [4–6].

The success of implant therapy also depends on bone condition of the surgical site during implant placement, as surgery is not always under ideal conditions. When there is insufficient bone support from the surrounding bones and surfaces are not fully covered with bones, this may lead to a failure of the surgery in the long term. In the case of a large bone defect area, a bone graft may be used along with an implant placement and the bone graft becomes a scaffold around the implant. It was reported that migration of osteoblast and osteoinductive materials to the implant surface increases the probability of implant success in the long term [7–9]. On the other hand, however, some reported that bone graft materials arrested new bone formation at the outset by blocking proliferation of osteoblast [10–12]. Nevertheless, it is

generally accepted that once grafting materials are absorbed and eventually disappear, the space is filled with new bone so that the level of osseointegration and osteogenesis eventually increases [13, 14].

Since there already exists previous study regarding positive effects of UV photofunctionalization on implant surfaces under insufficient bone condition [5], the purpose of this study was to compare and evaluate the effects of UV photofunctionalization on an implant placed over a critical defect area that did not heal over the duration of the study with and without a bone graft through histomorphometric and radiological analysis.

2. Materials and Methods

2.1. Experimental Animals. In this study, four female beagle dogs of twelve months old (weighing approximately 10 kg) were used. As a prestudy preparation, scaling and plaque control were performed for periodontal health. After treatment, they were fed with liquid foods to prevent masticatory trauma during healing. Animal selection, management, surgical protocol, and all experiments were reviewed and approved by the Animal Care and Use Committee, Yonsei Medical Center, Seoul, Korea (Approval number 2010-0362).

2.2. Experimental Implants. A total of 32 sandblasting with alumina and acid etching (SA) surface-treated internal type implants (Osstem implant system, TS II SA Fixture, Busan, Korea) being 3.5 mm in diameter and 8.5 mm in length were used in this study. All implants used in the experiment were manufactured simultaneously and stored in a sealed container, being kept minimally exposed to the air immediately before placement.

2.3. Ultraviolet Photofunctionalization. Photofunctionalization was performed by treating implants with UV light for 15 minutes using a photo device (TheraBeam Affiny, Ushio Inc., Tokyo, Japan) immediately before implantation according to manufacturer's recommendation [1, 4–6] (Figure 1). Details specifications of a photo device were as follows: input voltage (AC 100 to 240 V \pm 10%), input current (2.2 A max), temperature (15°C to 30°C), humidity (20% to 70% RH), and altitude (below 2,000 m).

2.4. Graft Materials. Demineralized freeze dried bone allograft (DFDBA) (SureOss-D, Demineralized Cortical Bone Powder, Hans Biomed Corp., Seoul, Korea) 200~850 μ m in particle size was used for grafting at bone defect.

2.5. Experimental Groups Design. First, all implant placement sites were divided into bone graft groups and control groups, with each group then subdivided again into UV-treated group and UV untreated group. The UV untreated group with bone graft was set to Group 2 (BG only), the UV-treated group with bone graft was set to Group 4 (UV/BG), the UV-treated group without bone graft was set to Group 3 (UV only), and finally the UV untreated group without bone graft was set to Group 1 (control). Eight SA surface implants were used for Group 4, eight SA surface implants for Group 2, four SA surface implants for Group 3, and lastly twelve SA surface

implants for Group 1. In this study, the sample sizes of Group 3 were reduced since the UV photofunctionalization effect has already been proven in many previous studies [1, 5, 6, 15, 16]. Implants were placed symmetrically to reduce differences in the sites by matching the initial states. Four implants were placed from posterior area of the 1st premolar in the right and left side of mandible (Figure 2). The distance between each implant was 10 mm and the experiment was carried out using a split-mouth design to minimize the interindividual variability from the estimates of the treatment effect [17]. The implants placed in the left side of mandible had a healing period of four weeks (4-week group) and the other implants placed in the right side of mandible had a healing period of twelve weeks (12-week group) (Figure 3).

2.6. Surgical Procedure. All of the surgical treatments were carried out under general anesthesia. Both mandibular premolars (from first to fourth premolar) were extracted atraumatically. 12 weeks after the extraction of four teeth (P1, P2, P3, and P4) on right side of mandible, sequential drilling for implant placement was performed. The distance between centers of implants was 10 mm. A one-wall bony defect in cuboid shape was then formed for each group. Those defects were uniformly 3 mm in depth and 5 mm in width (buccolingual and mesiodistal). The center of implant was then placed on the edge of the cuboid (Figure 4). Photofunctionalization of implants was performed for 15 minutes using a photo device immediately before implantation. 0.25 cc DFDBA was gently packed into each bone defect until it filled the entire cavity (Figure 5). One week after the surgical procedure, stitching out was done. The same processes were executed on left side of mandible eight weeks later. The beagle dogs were sacrificed after 4 weeks.

2.7. Fabrication of Histologic Specimens. After buffering of the tissue samples with neutral formalin fixation for two weeks, micro-CT was taken. Next, the samples were dehydrated in increasing grades of ethanol and subsequently infiltrated in Technovit 7200 resin (Heraeus Kulzer, Dormagen, Germany). Following the embedding in the acrylic resin, the blocks were polymerized and sectioned in the mesiodistal plane using a cutting-grinding unit (Exakt Exakt 300, Heraeus Kulzer, Norderstedt, Germany). The tissue samples were processed for ground sectioning according to methods described by Donath and Breuner and the sections were stained in H&E (hematoxylin and eosin) for light microscopic examination [18].

2.8. Micro-Computed Tomographic Analysis. A micro-computed tomography scanner (SkyScan 1076, SkyScan, Aartselaar, Belgium) was used to measure the percentage of the amount of new bone formation around implants. The new region of interest (ROI), the area most prone to be affected by the UV photofunctionalization and bone grafting, was set up in a rectangular parallelepiped 3.5 mm in width (mesiodistal) from the center of implant, 3.0 mm in length (buccolingual), and 3.0 mm in height. The amount of bone was measured in this area (Figure 6).

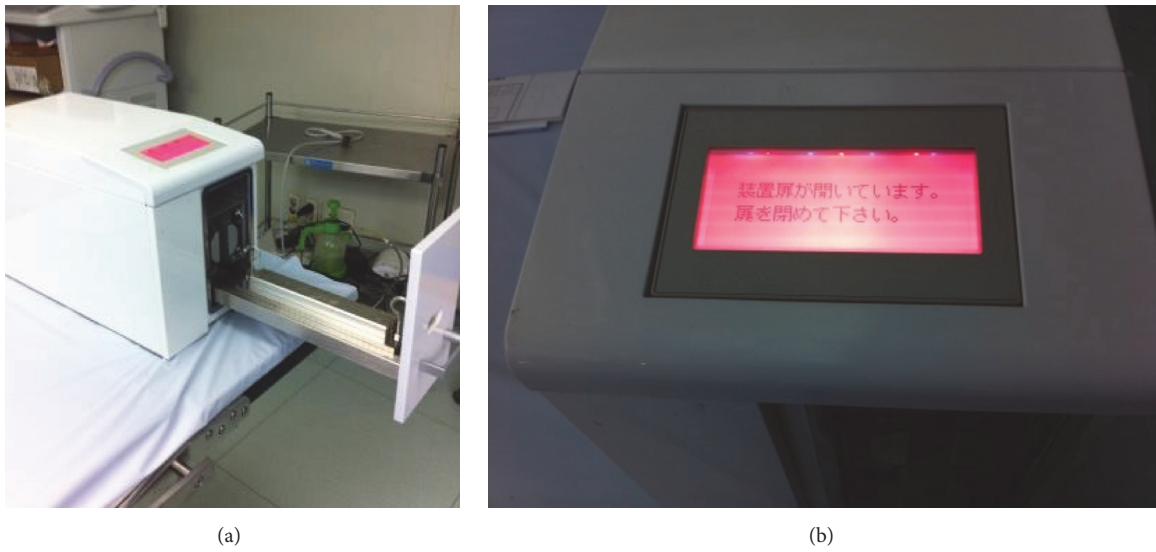


FIGURE 1: Photofunctionalization of implant fixture surface by ultraviolet light. (a) TheraBeam Affiny device (TheraBeam Affiny, Ushio, Tokyo, Japan). (b) Process of UV treatment on implant fixture during 15 minutes.

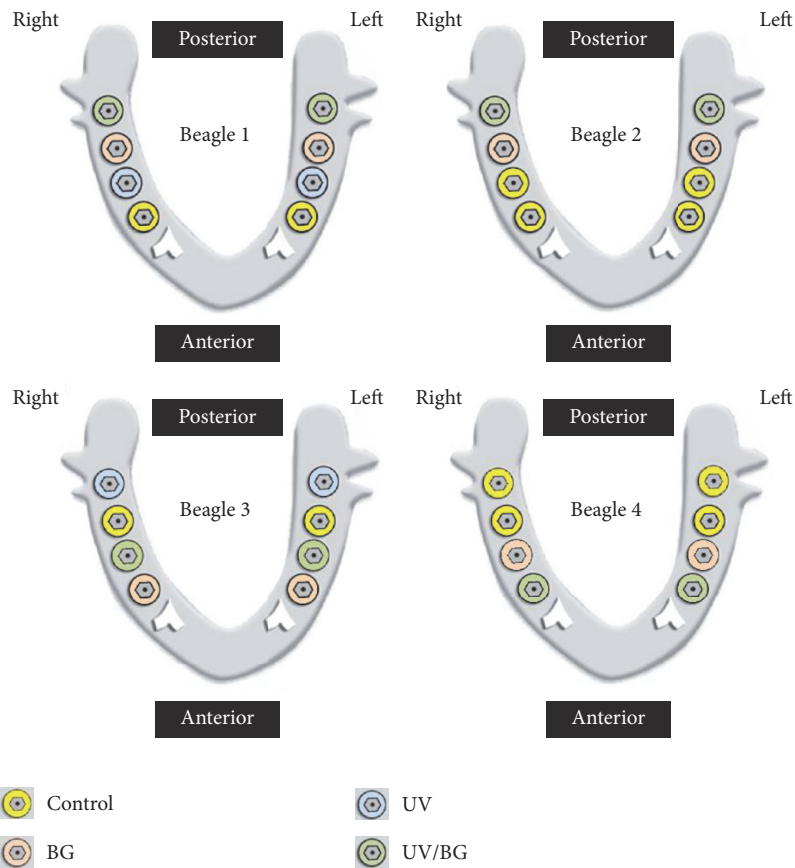


FIGURE 2: Experimental schematic diagrams.

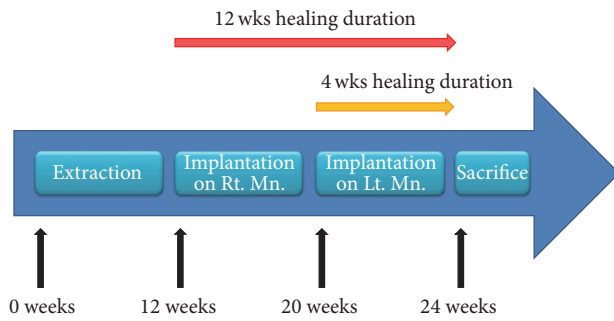


FIGURE 3: Diagram of experimental design protocol.

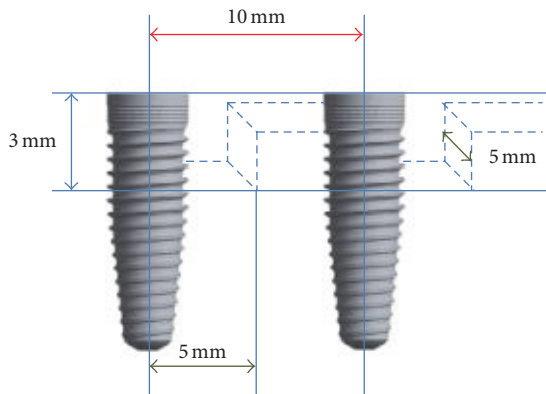


FIGURE 4: Schematic diagram of experimental design.

2.9. Histomorphometric Analysis. The stained histologic specimens were scanned and captured using optical microscopy at 12.5x and 50x magnification and then histomorphometrically measured using ImagePro Plus 4.5 (Media Cybernetics, Silver Spring, Maryland, USA). At first, the actual zone of formed defect was set as ROI, the area most prone to be affected by the UV photofunctionalization and bone grafting, by sectionalizing the region on histologic specimens. Then, the ratio for bone-to-implant contact (BIC, %), new bone area formed in defect area (new bone area, %), remaining graft material area in defect area (graft material area, %), and resorption area in defect area (resorption area, %) were calculated in ROI. BIC was measured at three consecutive threads in ROI. New bone area ratio and remaining graft material area ratio were calculated as a percentage of the area occupied by each one in ROI. Lastly, resorption area ratios were obtained as a percentage of the area in which bone filling did not occur in ROI (Figure 7).

2.10. Statistical Analysis. The ratios for BIC, new bone area, remaining graft material area, resorption area, and micro-CT value were compared to verify the difference between Groups 1 and 3. The same measurements were carried out for Groups 2 and 4. The Wilcoxon rank sum test was used as a nonparametric statistical method to evaluate the data due to the small sample size and large standard deviations. All calculations were performed using a specific statistical program (SPSS ver. 18.0, IBM Co., Somers, NY, USA), and the level of significance was set at 5%.

TABLE 1: The mean of micro-CT value ratios at 4 and 12 weeks.

Group	Micro CT value ratio	
	4 weeks	12 weeks
1	12.33 ± 4.52	12.18 ± 8.17
2	10.97 ± 1.74	7.62 ± 6.95
3	14.37 ± 13.55	27.9 ± 16.45
4	15.06 ± 3.59	0.44 ± 0.13

3. Results

3.1. Micro-Computed Tomographic Findings. For the comparison of cases without bone graft, in Groups 1 and 3, micro-CT bone volume ratio was measured in ROI (Figures 8 and 9). The mean value and standard deviation were then calculated (Table 1). Group 3 showed significantly increased micro-CT bone volume at 12 weeks compared to that of Group 1 ($p < 0.05$). However, for the comparison of cases with bone graft, in Groups 2 and 4, Group 4 displayed significantly increased micro-CT bone volume at 4 weeks compared to that of Group 2 ($p < 0.05$) (Figure 10).

3.2. Histomorphometric Findings. In Groups 1 and 3, BIC ratio (%) was calculated. Although increased BIC ratio was identified in Group 3, there was no significant difference in BIC ratio between the two groups at either time point (4 weeks and 12 weeks). Also, no significant difference in BIC was identified between Groups 2 and 4 at either time point (Table 2 and Figure 11).

Regarding new bone area ratio (%), a greater new bone area was identified in Group 3 than in Group 1. However, there was no significant difference in new bone area ratio between Groups 1 and 3. Also, in Groups 2 and 4, the similar results were identified but with no significant difference identified between two groups. Also, the remaining graft material area ratio (%) was calculated and there was no significant difference between Group 2 and Group 4.

Although no significant difference was found, there was much reduced resorption area ratio (%) observed in Group 3 compared to that in Group 1 at 12 weeks. Even when bone graft materials was used, decreased resorption area ratio was identified in Group 4 compared to that in Group 2. However, no statistically significant difference was found.

4. Discussion

The purpose of this study was to compare and evaluate, through histomorphometric and radiological analysis, the effects of UV photofunctionalization on an implant placed over a critical defect area with and without a bone graft. A large critical bone defect 5 mm in width was designed for the present study as the term “Critical Size Defect” (CSD) was defined in animal research as the size of a defect that will not heal over the duration of the study [19].

First, measurements for BIC ratio (%) in ROI of each group were compared. The groups of implants placed over bone defect without graft yielded the similar BIC ratios at 4 weeks regardless of the presence of UV treatment. Conversely,

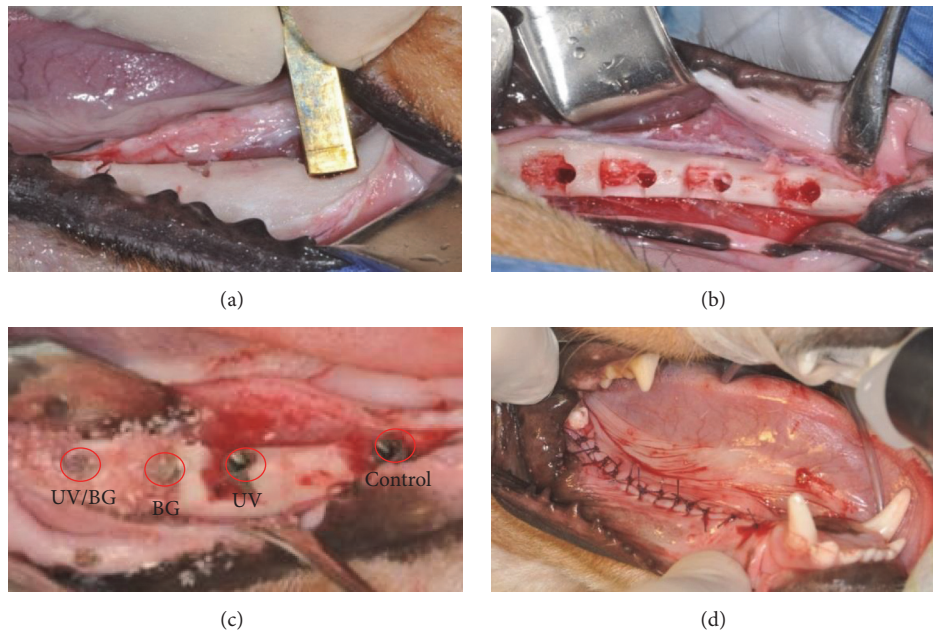


FIGURE 5: Clinical views of surgical procedure. (a) Forming the standardized defects. (b) Drilling for implant placement and forming the defects. (c) Implants placed with bone graft (Group 4, Group 2, Group 3, and Group 1). (d) Wound closure with suture.

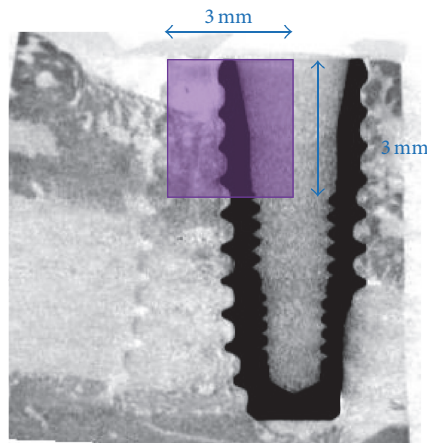


FIGURE 6: Bone volume measuring range in micro-CT image.

TABLE 2: The mean value of each ratio at 4 and 12 weeks.

	Group 1		Group 2		Group 3		Group 4	
	4 weeks	12 weeks						
BIC ratio (%)	42.73 ± 31.27	40.47 ± 18.59	13.59 ± 19.22	25.78 ± 23.94	47.98 ± 32.96	70.94 ± 14.59	28.11 ± 19.11	22.43 ± 31.72
New bone area ratio (%)	32 ± 16.26	48.53 ± 13.61	7.43 ± 6.17	14.2 ± 15.74	40.62 ± 39.33	55.49 ± 29.57	15.09 ± 8.81	5.28 ± 3.2
Remaining graft material area ratio (%)			9.78 ± 5.82	12.08 ± 9.57			21.4 ± 6.62	16.48 ± 6.31
Resorption area ratio (%)	36.13 ± 7.91	46.09 ± 17.99	17.4 ± 19.3	39.23 ± 35.91	33.76 ± 28.58	12.15 ± 17.19	5.09 ± 10.18	21.79 ± 17.66

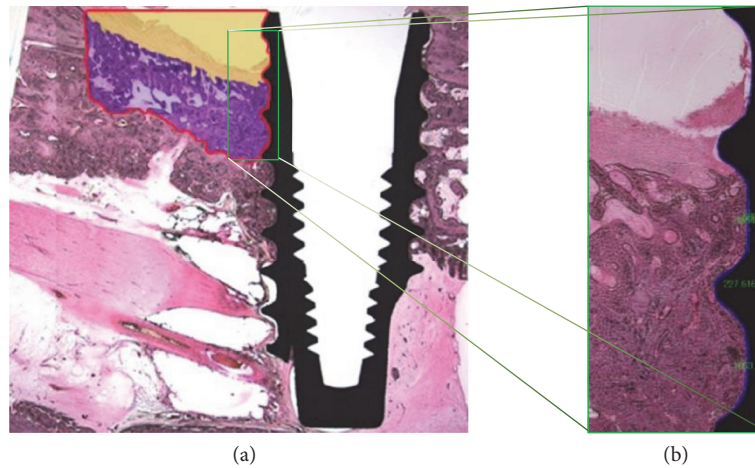


FIGURE 7: Histologic images showing experimental site, red box → ROI. (a) H&E stained image showing experimental site ($\times 12.5$), purple zone → new bone area (%) or remaining graft material area (%), and yellow zone → resorption area (%). (b) BIC in ROI, (H&E stained, $\times 50.0$).

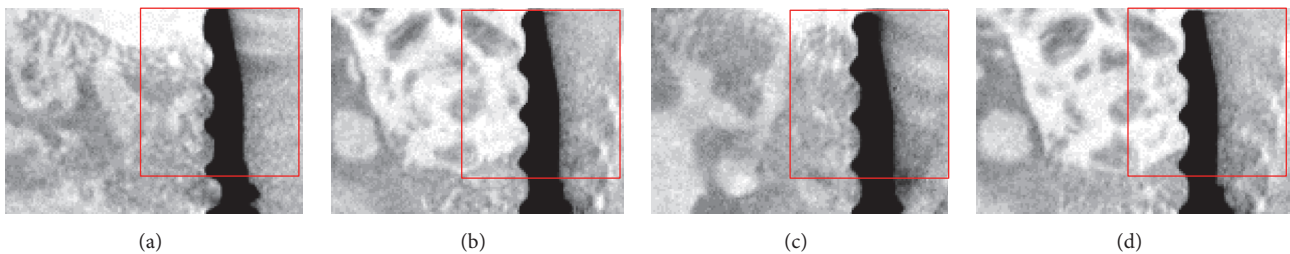


FIGURE 8: The representative micro-CT images of each group at 4 weeks. Red box → ROI in experimental site. (a) Group 1, (b) Group 2, (c) Group 3, and (d) Group 4.

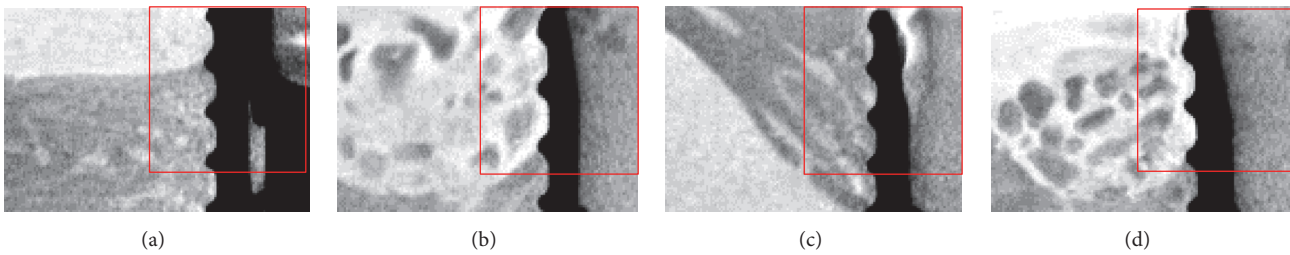


FIGURE 9: The representative micro-CT images of each group at 12 weeks. Red box → ROI in experimental site. (a) Group 1, (b) Group 2, (c) Group 3, and (d) Group 4.

in the group of implants placed over bone defect with graft, BIC ratios of UV-treated implant surfaces were greater than those at 4 weeks but lower than those at 12 weeks although there was no statistically significant difference in BIC ratio between UV-treated group and UV-untreated group. BIC values in Group 4 at 4 weeks were actually more than twice the BIC values in Group 2. On the other hand, BIC values in Group 4 at 12 weeks showed little difference from BIC values in Group 2. These results suggest that BIC of implant surfaces was increased by UV photofunctionalization for bone defects with a bone graft at the initial stage of the implant placement. The decrease in BIC values at 12 weeks could possibly be attributable to the characteristics of female

beagle dogs, including concerns that they are more variable than males due to cyclical reproductive hormones [20], which may lead to a larger variation among the individuals. This can be related to the one of the limitations of the present study: relatively high standard deviation. A small number of sample sizes may also have resulted in such high standard deviation. To resolve these issues in further research and to further evaluate the effect of experimental intervention prior to the application in clinic, it may be necessary to use a larger number of male dogs.

Next, the new bone area ratio (%) was measured in ROI. The mean of groups with UV photofunctionalization was slightly higher at both 4 and 12 weeks when the implant

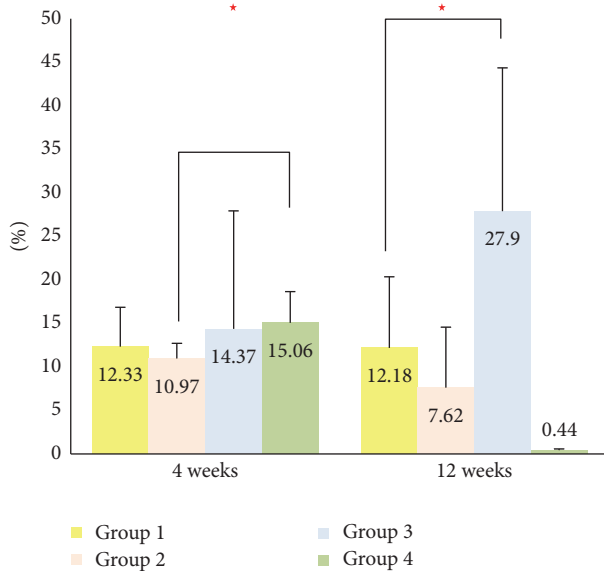


FIGURE 10: The mean of micro-CT value ratios at 4 and 12 weeks. Red star indicates that there was a significant difference ($p < 0.05$).

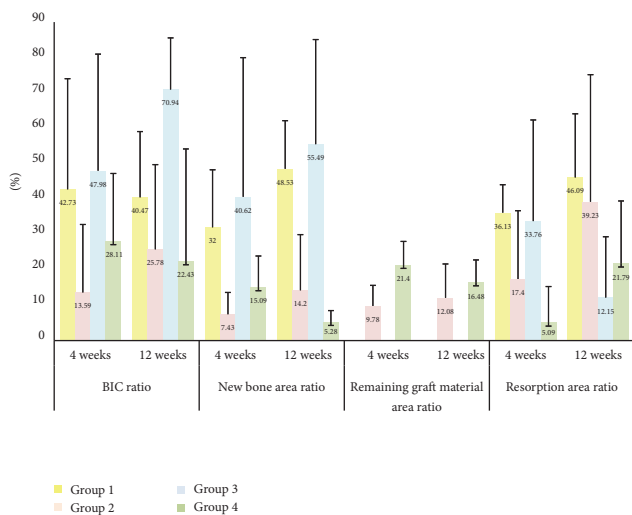


FIGURE 11: The mean value of each ratio at 4 and 12 weeks.

was placed without a bone graft, yet with no statistically significant difference. As UV photofunctionalization affected the bone defect area itself, more new bone might have been formed. Group 4 at 4 weeks had a greater new bone area ratio (%) values than those of Group 2, which may indicate that the UV photofunctionalization had again a positive influence on early new bone formation for bone defect with a bone graft. However, Group 2 measurements at 12 weeks were higher than those in Group 4, which is in accordance with the results from the BIC ratio at 12 weeks and can be explained in the same extent.

The area of the remaining graft material ratio (%) in ROI was measured for comparisons. The higher the remaining graft material ratio is, the more the graft material remained in the defect area and thus the greater the volume of the defect

is maintained. Because the grafted, demineralized materials were absorbed rapidly, there were questions whether they could serve as a scaffold for a long time. In fact, Group 2 showed greater measurements at 4 weeks than at 12 weeks. Group 4 showed less remaining grafting material at 12 weeks. Based on comparisons of the actual measurements of each group, values were inconsistent and had large standard deviations at 12 weeks. In fact, it was previously reported that, in a one-wall defect, it is important to prevent dissipation of graft materials [21, 22]. In the present study, however, no membrane or any other methods for maintenance of graft material were used and this may have resulted in inconsistent and large standard deviation at 12 weeks. Therefore, subsequent experiments may yield more reliable results if any methods for maintaining graft material are used.

The resorption area ratio (%) reflected the degree of defect volume maintenance. In the group without bone graft, UV treatment showed little effect at 4 weeks. With time, the resorption area ratio decreased in Group 3. This maybe resulted from the large amount of new bone as well as from less resorption of bone itself. The differences in bone volume measured using micro-CT surely account for the differences in resorption area ratio. The amount of new bone was measured in three dimensions with a micro-CT scanner whereas the resorption area was measured in one plane with a light microscopy. These differences must be considered in calculating each measurement and may underlie limitations in calculating the resorption area using micro-CT measurements. For this reason, the implant placement position was considered the major cause of differences in resorption area ratio at 12 weeks. Further study should be required to employ more subdivided positions for implant placement in order to enable greater uniformity of placement. The resorption area ratio in Group 4 was less than in Group 2 at 4 weeks. This may be attributed to the greater amount of new bone and remaining graft material in Group 4 than in Group 2. Similarly, the resorption area ratio in Group 4 was less than in Group 2 at 12 weeks, a consequence of the difference in resorption rates due to posterior implant placement. Due to the difference in resorption rate caused by implant placement position, the amount of remaining graft material in Group 4 exceeded that of Group 2 and this may also explain the relatively reduced resorption area ratio in Group 4.

Regarding amount of new bone in ROI measured by micro-CT, in the group without bone graft, although the similar patterns in histomorphometric measurements at 4 weeks are identified, Group 3 measurements were about twice higher than those of Group 1 at 12 weeks. There was also statistically significant difference identified. These distinctions may be due to differences between measurement with light microscopy and micro-CT scanner as mentioned above. In the bone graft groups, Group 4 scored higher in new bone volume measurements than Group 2 at an early stage (4 weeks). This agrees with the pattern of new bone formation measurements using a light microscopy.

Within the limitation of the present study, based on aforementioned results, it can be concluded that UV photofunctionalization had a positive effect on new bone formation of bone defect with bone graft in the early stage. However, the

results of each group in a late stage (12 weeks) were not significantly correlated with the presence of UV treatment and this may be partly attributed to the fact that the results of these experiments do not completely rule out the effect of implant location. Therefore, further study will be required to maintain uniform implant conditions including placement location as much as possible by increasing the number of sample sizes and by subdividing the location of implant placement.

Disclosure

Young-Bum Park is co-corresponding author for supervising overall animal study. This paper is a part of Min-Young Kim's thesis.

Competing Interests

The authors declare that they have no competing interests.

Authors' Contributions

Min-Young Kim and Hyunmin Choi equally contributed to the works described in this manuscript.

Acknowledgments

This research was supported by a faculty research grant of Yonsei University College of Dentistry (6-2015-0106), Basic Science Research Program, through the National Research Foundation of Korea (NRF) funded by the Ministry of Education (NRF-2016R1D1A1B03934584) and Institute for Information & Communications Technology Promotion (IITP) grant funded by the Korea Government (MSIP) (no. R0190-15-1113).

References

- [1] T. Ogawa, "Ultraviolet photofunctionalization of titanium implants," *The International journal of oral & maxillofacial implants*, vol. 29, no. 1, pp. e95–102, 2014.
- [2] T. Berglundh, I. Abrahamsson, N. P. Lang, and J. Lindhe, "De novo alveolar bone formation adjacent to endosseous implants: a model study in the dog," *Clinical Oral Implants Research*, vol. 14, no. 3, pp. 251–262, 2003.
- [3] J. E. Davies, "Mechanisms of endosseous integration," *International Journal of Prosthodontics*, vol. 11, no. 5, pp. 391–401, 1998.
- [4] H. Aita, N. Hori, M. Takeuchi et al., "The effect of ultraviolet functionalization of titanium on integration with bone," *Biomaterials*, vol. 30, no. 6, pp. 1015–1025, 2009.
- [5] A. Funato and T. Ogawa, "Photofunctionalized dental implants: a case series in compromised bone," *The International journal of oral & maxillofacial implants*, vol. 28, no. 6, pp. 1589–1601, 2013.
- [6] A. Funato, M. Yamada, and T. Ogawa, "Success rate, healing time, and implant stability of photofunctionalized dental implants," *The International Journal of Oral & Maxillofacial Implants*, vol. 28, no. 5, pp. 1261–1271, 2013.
- [7] D. Buser, V. Chappuis, M. M. Bornstein, J.-G. Wittneben, M. Frei, and U. C. Belsler, "Long-term stability of contour augmentation with early implant placement following single tooth extraction in the esthetic zone: a prospective, cross-sectional study in 41 patients with a 5- to 9-year follow-up," *Journal of Periodontology*, vol. 84, no. 11, pp. 1517–1527, 2013.
- [8] G. E. Friedlaender, "Bone grafts. The basic science rationale for clinical applications," *The Journal of Bone & Joint Surgery—American Volume*, vol. 69, no. 5, pp. 786–790, 1987.
- [9] R. E. Jung, N. Fenner, C. H. F. Hämmerle, and N. U. Zitzmann, "Long-term outcome of implants placed with guided bone regeneration (GBR) using resorbable and non-resorbable membranes after 12–14 years," *Clinical Oral Implants Research*, vol. 24, no. 10, pp. 1065–1073, 2013.
- [10] A. Stavropoulos, L. Kostopoulos, J. R. Nyengaard, and T. Karring, "Deproteinized bovine bone (Bio-Oss) and bioactive glass (Biogran) arrest bone formation when used as an adjunct to guided tissue regeneration (GTR): an experimental study in the rat," *Journal of Clinical Periodontology*, vol. 30, no. 7, pp. 636–643, 2003.
- [11] D. Carmagnola, T. Berglundh, M. Araújo, T. Albrektsson, and J. Lindhe, "Bone healing around implants placed in a jaw defect augmented with Bio-Oss. An experimental study in dogs," *Journal of Clinical Periodontology*, vol. 27, no. 11, pp. 799–805, 2000.
- [12] F. A. Santos, M. T. Pochapski, M. C. Martins, E. G. Zenóbio, L. C. Spolidoro, and E. Marcantonio Jr, "Comparison of biomaterial implants in the dental socket: histological analysis in dogs," *Clinical Implant Dentistry and Related Research*, vol. 12, no. 1, pp. 18–25, 2010.
- [13] M. Marco Degidi, A. Piattelli, V. Perrotti, and G. Iezzi, "Histologic and histomorphometric evaluation of an implant retrieved 8 years after insertion in a sinus augmented with anorganic bovine bone and anorganic bovine matrix associated with a cell binding peptide," *The International Journal of Periodontics & Restorative Dentistry*, vol. 32, pp. 451–457, 2012.
- [14] A. Philipp, W. Duncan, M. Roos, C. H. Hämmerle, T. Attin, and P. R. Schmidlin, "Comparison of SLA® or SLActive® implants placed in the maxillary sinus with or without synthetic bone graft materials—an animal study in sheep," *Clinical Oral Implants Research*, vol. 25, no. 10, pp. 1142–1148, 2014.
- [15] T. Ueno, M. Yamada, N. Hori, T. Suzuki, and T. Ogawa, "Effect of ultraviolet photoactivation of titanium on osseointegration in a rat model," *The International Journal of Oral & Maxillofacial Implants*, vol. 25, no. 2, pp. 287–294, 2010.
- [16] T. Ueno, M. Yamada, T. Suzuki et al., "Enhancement of bone-titanium integration profile with UV-photofunctionalized titanium in a gap healing model," *Biomaterials*, vol. 31, no. 7, pp. 1546–1557, 2010.
- [17] J. C. de Vicente, O. Recio, L. Martín-Villa, L. M. Junquera, and J. S. López-Arranz, "Histomorphometric evaluation of guided bone regeneration around implants with SLA surface: an experimental study in beagle dogs," *International Journal of Oral and Maxillofacial Surgery*, vol. 35, no. 11, pp. 1047–1053, 2006.
- [18] K. Donath, "Equipment and methodical performance," in *Preparation of Histologic Sections*, EXAKT-Kulzer-Publication, Norderstedt, Germany, 1995.
- [19] A. K. Gosain, L. Song, P. Yu et al., "Osteogenesis in cranial defects: reassessment of the concept of critical size and the expression of TGF- β isoforms," *Plastic and Reconstructive Surgery*, vol. 106, no. 2, pp. 360–371, 2000.
- [20] I. Zucker and A. K. Beery, "Males still dominate animal studies," *Nature*, vol. 465, no. 7299, p. 690, 2010.
- [21] J. Sakata, H. Abe, A. Ohazama et al., "Effects of combined treatment with porous bovine inorganic bone grafts and bilayer

porcine collagen membrane on refractory one-wall intrabony defects,” *International Journal of Periodontics and Restorative Dentistry*, vol. 26, no. 2, pp. 161–169, 2006.

- [22] J.-I. Park, C. Yang, Y.-T. Kim et al., “Space maintenance using crosslinked collagenated porcine bone grafted without a barrier membrane in one-wall intrabony defects,” *Journal of Biomedical Materials Research B Applied Biomaterials*, vol. 102, no. 7, pp. 1454–1461, 2014.

Research Article

Bone Healing Improvements Using Hyaluronic Acid and Hydroxyapatite/Beta-Tricalcium Phosphate in Combination: An Animal Study

Yen-Lan Chang,^{1,2} Yi-June Lo,³ Sheng-Wei Feng,^{1,4} Yu-Chih Huang,¹ Hsin-Yuan Tsai,¹
Che-Tong Lin,¹ Kan-Hsin Fan,⁵ and Haw-Ming Huang^{1,6}

¹School of Dentistry, College of Oral Medicine, Taipei Medical University, Taipei, Taiwan

²Dental Department, Mackey Memorial Hospital, Taipei, Taiwan

³Dental Department, Wan Fang Hospital, Taipei Medical University, Taipei, Taiwan

⁴School of Oral Hygiene, College of Oral Sciences, Taipei Medical University, Taipei, Taiwan

⁵Dental Department, En Chu Kong Hospital, New Taipei City, Taiwan

⁶Graduate Institute of Biomedical Materials and Tissue Engineering, College of Biomedical Engineering, Taipei Medical University, Taipei, Taiwan

Correspondence should be addressed to Haw-Ming Huang; hbm@tmu.edu.tw

Received 3 October 2016; Accepted 23 November 2016

Academic Editor: Ren-Yeong Huang

Copyright © 2016 Yen-Lan Chang et al. This is an open access article distributed under the Creative Commons Attribution License, which permits unrestricted use, distribution, and reproduction in any medium, provided the original work is properly cited.

The purpose of this study was to investigate whether the use of HLA as an aqueous binder of hydroxyapatite/beta-tricalcium phosphate (HA- β TCP) particles can reduce the amount of bone graft needed and increase ease of handling in clinical situations. In this study, HA/ β TCP was loaded in commercially available crosslinking HLA to form a novel HLA/HA- β TCP composite. Six New Zealand White rabbits (3.0–3.6 kg) were used as test subjects. Four 6 mm defects were prepared in the parietal bone. The defects were filled with the HLA/HA- β TCP composite as well as HA- β TCP particle alone. New bone formation was analyzed by micro-CT and histomorphometry. Our results indicated that even when the HA- β TCP particle numbers were reduced, the regenerative effect on bone remained when the HLA existed. The bone volume density (BV/TV ratio) of HLA/HA- β TCP samples was 1.7 times larger than that of the control sample at week 2. The new bone increasing ratio (NBIR) of HLA/HA- β TCP samples was 1.78 times higher than the control group at week 2. In conclusion, HA- β TCP powder with HLA contributed to bone healing in rabbit calvarial bone defects. The addition of HLA to bone grafts not only promoted osteoconduction but also improved handling characteristics in clinical situations.

1. Introduction

Guided bone regeneration is a surgical procedure to regenerate enough bone for successful implant placement. It can be achieved by performing ridge augmentation and bone regeneration procedures which increase bone volume at bone defect areas. The materials used for guided bone regeneration should be osteoconductive or osteoinductive. Although commercialized bone graft materials have been available for some time and are proven to be a useful material for bone regeneration, there is still room for improvement.

Sinus elevation is a surgical procedure that adds bone volume to a patient's upper jaw in the area of molars and

premolars. During surgery, bone graft material was packed into space where the sinus was. The most commonly used compositions for sinus elevation and guided bone regeneration is a mixture of hydroxyapatite (HA) and beta-tricalcium phosphate (β TCP) [1–3]. However, shaping this material to fit the sinus cavity is difficult. In addition, it is hard to adhere the material without loss during operation.

Hyaluronic acid (HLA) is a polysaccharide consisting of alternating residues of D-glucuronic acid and N-acetylglucosamine [4]. It is found in abundance in the extracellular space [5] and load-bearing joints [6, 7]. In addition, HLA is also involved in skin moisture due to its unique capacity to retain water [8]. It has been reported that HLA

can be used for knee and temporomandibular osteoarthritis treatments [9]. In the field of dentistry, hyaluronic acid demonstrated anti-inflammatory, antioxidant, and antibacterial properties in the treatment of periodontal diseases [10]. In addition, due to its viscoelastic properties, it can be used as an adjunct to maintain space during the treatment of periodontitis.

Recently HLA has been studied as a biomaterial for tissue engineering. In 2011, Correia et al. prepared freeze-dried composite scaffolds of chitosan and HLA for cartilage tissue engineering and found that the incorporation of HLA enhanced cartilage ECM production [6]. In an animal study, Sasaki and Watanabe (1995) studied the osteoinductive action of HLA and found that HLA is capable of accelerating new bone formation through mesenchymal cell differentiation in bone wounds [11]. This is because bone grafts mixed with HLA can alter the physical and chemical properties of graft materials which results in enhanced capability for cell adhesion, proliferation, and migration. Their conclusion indicated that scaffolds incorporating HLA served as a support system for enhancing bone regeneration. Other recent animal studies also support the idea that composites made of bone grafts and HLA enhance bone growth and mineralization [7, 12, 13]. According to these results, Schulz et al. (2014) coated HLA on the surface of dental titanium implants and inserted them into the maxilla of miniature pigs. Their results demonstrated that HLA increases bone formation at implant/bone interface in the early healing period [4].

In 2013, ELkarargy conducted a histomorphometric study to investigate the usefulness of HA/ β TCP with HLA for alveolar sockets preservation. He found that HA/ β TCP with HLA exhibits a more efficient in osteoconduction when compared to the samples without HLA [14]. Bone grafts such as HA/ β TCP used for sinus elevation and guided bone regeneration are expensive. Thus reducing the amount of the bone graft material used without affecting treatment efficiency is a challenge for scientists and dentists. Due to HLA's unique viscoelastic and osteogenetic properties, the combination of HLA and HA/ β TCP should provide advantages compared to the use of either alone. Accordingly, the aim of this study is to test the hypothesis that an HLA and HA/ β TCP composite material can reduce the amount of bone graft needed and increase ease of handling in clinical situations.

2. Materials and Methods

2.1. Physical Properties of HLA. The HLA used in this study is a commercially available HLA (Global Xtra, DermaFill Global, Paris, France) with a molecular weight of 2.5–3.0 MDa. The HLA was crosslinked with 1,4-butanediol diglycidyl ether (BDDE) and its concentration is 25 mg/mL. Measurement of HLA particle size distribution in this study was performed using a particle size analyzer (90 Plus, Brookhaven Instruments Corporation, Holtsville, NY, USA). Before the test, a 1 mL sample was diluted 1 : 500 with purified water and stirred for 12 hrs. The pH value of the HLA used in this study was measured using a pH-meter at room temperature (Model 6173, JENCO Quality Instruments, San Diego, USA). The

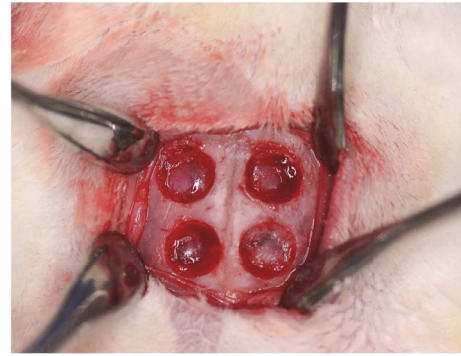


FIGURE 1: Skull defects for currently prepared material implantation. The two defects on the right were used for HLA/HA- β TCP and HA- β TCP implantation, while the two on the left were unfilled controls.

rheological characteristic of the tested HLA was performed on a rheometer (RheoStress 1, Haake, Germany). The HLA properties were characterized under steady and oscillatory regimes at 25°C as a previous study [15]. Briefly, oscillatory measurements were performed at a stress of 1.88 Pa in the linear region. The frequency range and shear ratio were set at 0.1–10 Hz and 0.1–20 s⁻¹, respectively. Storage (G') and loss (G'') moduli of the tested HLA were recorded as a function of frequency. Dynamic viscosity (η^*) of the tested HLA was recorded as a function of oscillation frequency.

2.2. Animal Study. In this study, 6 New Zealand White rabbits, weighing 3.0–3.6 kg, were used as test subjects. The rabbits were fed solid food and water for adaptation in bracket cages at a temperature of 25°C and a humidity of 50%. All rabbits were maintained and used according to the guidelines set out in “The Care and Use of Laboratory Animals of Taipei Medical University” (LAC-2014-0087). To prepare the HLA/HA- β TCP sample, 1 mL commercialized hyaluronic acid (Global Xtra, DermaFill, Paris, France) was diluted with 3.5 mL phosphate buffer solution (PBS). Then 100 mg HA- β TCP (250–500 μ m, MBCP, Biomatlante, Belin, France) was added to the diluted HLA solution.

Before surgery, the rabbits were anesthetized with intramuscular Zoletil 50 at a dose of 0.5 mL (Virbac, Carros Cedex, France). The operation site was shaved and the calvaria bone was exposed through a skin incision. According to previous studies [16, 17], four circular defects with a diameter of 6 mm were prepared in the parietal bone (Figure 1). The two right defects were grafted with 0.2 g of prepared HA- β TCP and HLA/HA- β TCP. The two left defects were unfilled controls.

After 2 and 4 weeks of healing, the rabbits were euthanized under anesthesia by CO₂ gas asphyxiation and tissues from inside the surgical sites were collected. Bone blocks were obtained using a surgical burr attached to a slow-speed electrical hand piece. The blocks were then preserved and fixed in a 10% formaldehyde solution at pH 7.0 for further analysis.

2.3. Micro-CT Examination. To test the new bone formation, the collected bone blocks were scanned in a micro-CT

scanner (SkyScan 1076, Bruker, Kontich, Belgium). The machine was set with the following parameters: images were acquired at 49 kV, 200 μ A, through a 0.5 mm thick aluminum filter with a pixel size of 18.27 μ m. The reconstructed images were imported into the analysis software (CTAn, Bruker) for calculating bone volume. According to previous studies [18–20], the volume of interest (VOI) was defined as the relative changes in bone volume density (BV/TV%), the percentage of bone volume (BV) to the total tissue volume (TV). The new bone growth was evaluated using calculated VOI. In addition, the numbers of HA- β TCP particles found in the defect were counted using the micro-CT images.

2.4. Histological Analysis. To quantitate bone growth condition, the bone specimens were decalcified. The samples were immersed in 10% EDTA (0.1M phosphate buffer, pH 7.4) for 4 weeks. After embedding the samples in paraffin, they were cut into 5 μ m thick sections. The dehydrating procedure was performed in an ascending alcohol gradient (60%–100%). Then the samples were stained with hematoxylin and eosin. Histological images were observed with a light microscope connected to a digital camera. The new bone growth condition was obtained by counting the area of newly formed bone in the defect using commercial imaging software (ImageJ, National Institutes of Health, USA). In this study, the new bone increase ratio was calculated to represent the bone growth condition. This normalized value was defined as the newly formed bone area of filled samples divided by the control sample analogue value.

2.5. Statistical Analysis. Mean values and standard deviations of each measurement were obtained. To evaluate differences between the sample and control, one-way analysis of variance (ANOVA) (SPSS Inc., Chicago, IL, USA) with Tukey's post hoc was performed. A *p* value lower than 0.05 was considered statistically significant.

3. Results

3.1. Physical Properties of HLA. Figure 2 shows the particle size distributions of HLA used in this study. Our results show that the diameter of HLA particles is concentrated at 0.1–0.8 μ m with an average of $0.36 \pm 0.20 \mu$ m. The pH value of HLA was 6.96 ± 0.04 . Figure 3(a) shows the mechanical tests of the dynamic moduli. The elastic modulus (G') is higher than loss modulus (G''). The slope of the G' line is small and G'' displays a frequency dependence manner. Figure 3(b) shows the curve of complex viscosity (η^*) versus oscillation frequency. The HLA demonstrates a strong shear thinning property at higher shear rates. This phenomenon indicates that the test HLA is a non-Newtonian pseudoplastic material.

3.2. Micro-CT Examination. Typical results of micro-CT images of bone specimens are shown in Figure 4. At both weeks 2 and 4, new bone formation can be observed in all the three groups. For the control group, newly formed bone can be found only at the area around the inner surface of the defect (Figures 4(a) and 4(d)). However, newly formed bone

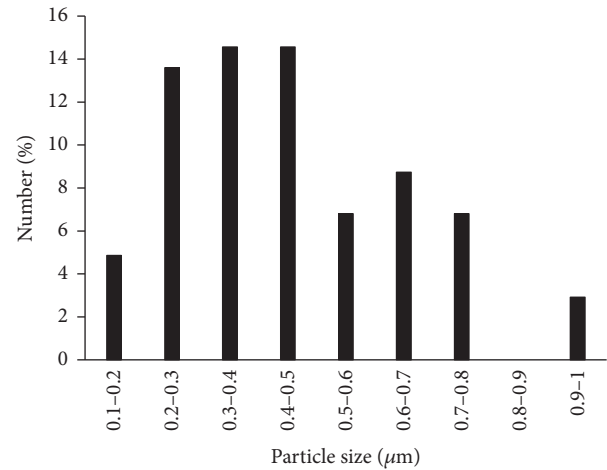


FIGURE 2: Particle diameter distribution of the HLA used in this study.

can be observed in the central area of the defect that was filled with HA- β TCP (Figures 4(b) and 4(e)). For the HLA/HA- β TCP samples, a similar phenomenon can also be identified (Figures 4(c) and 4(f)).

The differences in newly formed bone volume density (BV/TV ratio) between filled samples and controls were noted at both weeks 2 (Figure 5(a)) and 4 (Figure 5(b)) but were more obvious in the second week. However, no difference can be observed when comparing the HA- β TCP and HLA/HA- β TCP groups. At week 2, the BV/TV ratios for the HA- β TCP and HLA/HA- β TCP samples were $34.68 \pm 4.04\%$ and $34.21 \pm 2.90\%$, respectively. These values were almost 1.7 times larger than that of the control sample (19.65 ± 5.87). At week 4, the BV/TV ratios of the HA- β TCP and HLA/HA- β TCP samples increased to $40.81 \pm 1.79\%$ and $40.18 \pm 2.57\%$. However, there was a lower 1.25-fold difference between the filled group and blank control (Figure 5(b)). Figure 6 shows the particles in the defect at week 2. The number of particles in the HA- β TCP group was 134.0 ± 14.0 which is significantly higher than that of the HLA/HA- β TCP group (105.7 ± 12.7). Statistical analysis revealed that this increase was significant ($p < 0.05$).

3.3. Histological Analysis. Histological evaluation for all groups at each time point was shown in Figure 7. After 2 weeks of healing, the newly formed woven bone was in partial direct contact with the filled HA- β TCP surface in both the HA- β TCP and the HLA/HA- β TCP groups (Figures 7(b) and 7(c)). At 4 weeks, the newly formed bone was in close contact with the filled HA- β TCP surface (Figures 7(e) and 7(f)).

The histomorphometrical evaluation and the quantitative results seen in the new bone increase ratio (NBIR) are presented in Figure 8. Mean NBIR values were higher when the defect was filled with HA- β TCP, a 1.58-fold increase compared to the control. The ratio difference increased to 1.78-fold when HLA/HA- β TCP was used as the filling material. However, the NBIR values were not significantly different at 4 weeks.

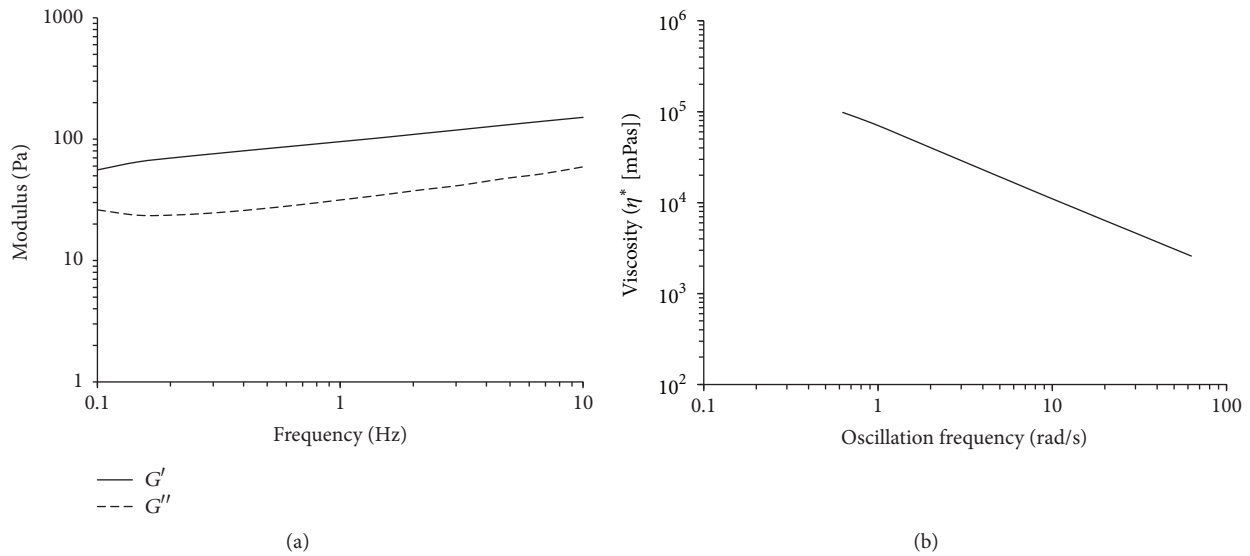


FIGURE 3: The mechanical spectra of the dynamic moduli of the HLA used in this study. Storage modulus (G') is shown in graph (a) and loss modulus (G'') is shown in graph (b). Graph (c) shows complex viscosity (η^*) as a function of oscillation frequency.

4. Discussion

The H&E staining and micro-CT data obtained in this study showed that the prepared HLA/HA- β TCP had excellent biocompatibility and osteointegration (Figures 7(c) and 7(f)). Micro-CT analysis showed that the BV/TV ratio increased in both HA- β TCP and HLA/HA- β TCP samples (Figure 5). In Figure 4, significant empty space can be observed in the HLA/HA- β TCP filled sample. A previous report indicated that HLA in the space between bone graft powder and bone tissue may affect new bone formation [21]. However, when comparing the BV/TV ratio between HA- β TCP and HLA/HA- β TCP groups, the addition of HLA did not significantly reduce BV/TV ratio at both weeks 2 and 4 (Figure 5). The histological results showed that HLA/HA- β TCP-treated defects had a greater new bone increase ratio than in defects treated with HA- β TCP alone and untreated controls (Figure 8). This inconsistency may be due to the limitation of micro-CT, which cannot detect bone quality change until the alternation reaches 30–40% [21].

From Figures 6 and 8, we found that while the particle number for HA- β TCP was reduced, the bone regenerative effect remained when the HLA was present. These results provide evidence that HLA/HA- β TCP is useful for tissue engineering, which is consistent with previous reports suggesting that bone grafts combined with HLA enhance bone growth [7, 13, 14, 21] and mineralization [12]. From the results of micro-CT images and BV/TV ratio, a smaller number of particles were used in HLA/HA- β TCP group and have the same healing results compared to the HA- β TCP group. It is reasonable to suggest that incorporating HA- β TCP with HLA provides higher regenerative efficiency for bone healing.

Previous studies have also suggested that the positive effect on bone healing is found at an early stage. For example, Schulz et al. (2014) coated HLA on the surface of dental titanium implants and inserted them into the maxilla of

miniature pigs [4]. They found that HLA increases bone formation at the implant-bone interface in the early healing period. An animal study by Krause et al. (2014) investigated a new bone substitute paste composed of pure phase β -TCP and HLA. They found that the substitute showed an early indication of bone formation [22]. In 2014, Nguyen and Lee prepared a scaffold by loading HLA hydrogel into a biphasic calcium phosphate (BCP) ceramic. After a series of animal studies, they suggested that this novel bone substitute exhibited rapid new bone formation and a high rate of collagen mineralization [12]. In the present study, the BV/TV ratio for the HLA/HA- β TCP filled samples was almost 1.7 times larger than that of the control sample at week 2. However, the difference between ratios was 1.25 at week 4. This phenomenon confirmed the results of previous studies which indicated that the positive effect of HLA on bone healing is seen at an early healing period because HLA is one of the components of the extracellular matrix that serves as a scaffold for mesenchymal cell migration [23]. This effect induced the mesenchymal cells to differentiate, proliferate [11, 24], and migrate [25] which induced growth of osteoblasts and osteocytes at the early healing stage.

It has been reported that HLA's regenerative function is strongly affected by its physical properties. The HLA used in this study is a commercially available crosslinked product with high molecular weight. According to a previous study, the reticulated HLA can demonstrate a better regenerative function compared to linear HLA when it is mixed with β TCP granules [26]. In addition, particle size and molecular weight also strongly affects the biofunction of HLA [8, 27]. In 2015, Zhao et al. found that high molecular weight HLA increased the mRNA expressions of ALP, RUNX-2, and OCN [28]. That is, HLA of higher molecular weight promoted bone formation. It is well known that high molecular weight and crosslinking degree result in high HLA viscosity. Figure 3(a) shows mechanical tests of the dynamic moduli. The elastic G'

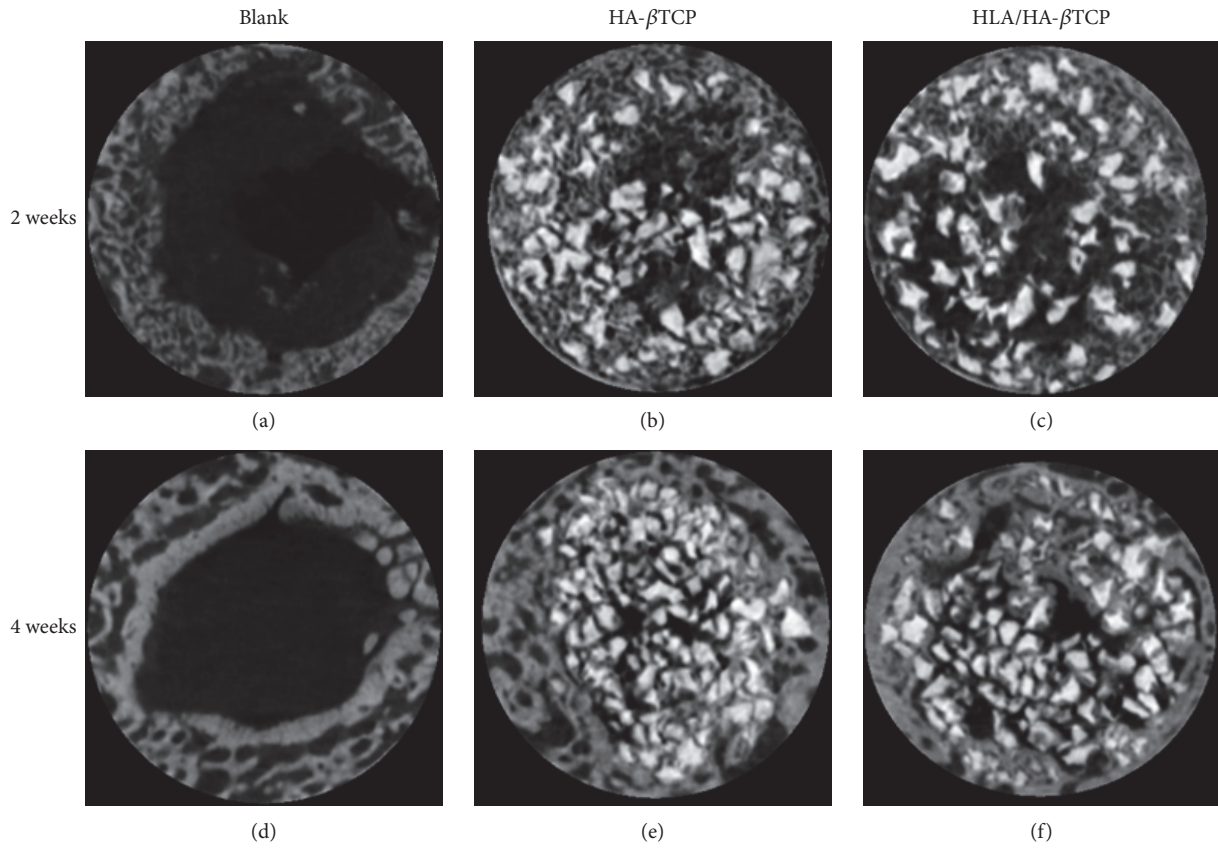


FIGURE 4: Micro-CT images of the artificial defects. (a) and (d) are the blank control at weeks 2 and 4, respectively. (b) and (e) are HA-βTCP filled groups at weeks 2 and 4, respectively. (c) and (f) are HLA/HA-βTCP filled groups at weeks 2 and 4, respectively.

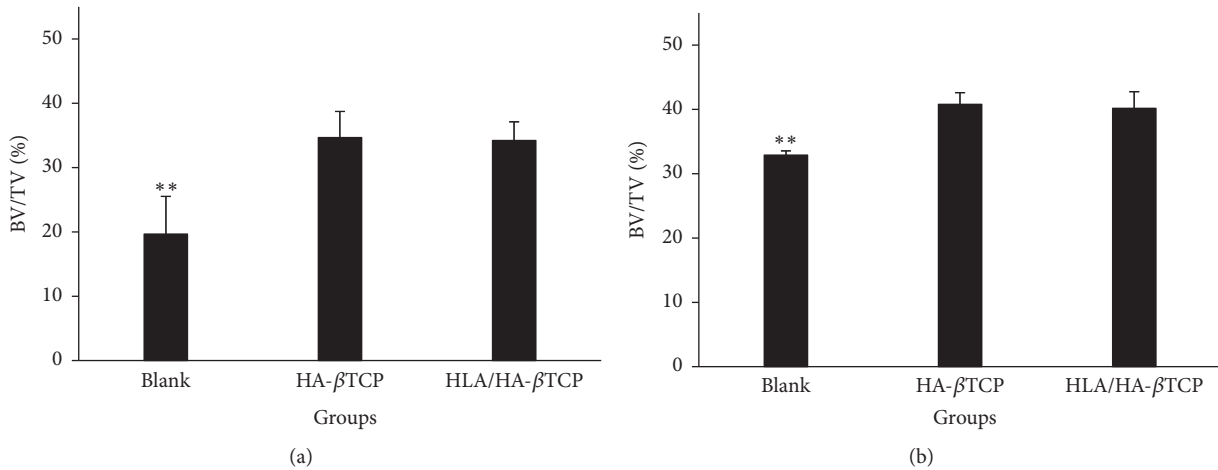


FIGURE 5: BV/TV% for the artificial defects filled with HA-βTCP alone and HLA/HA-βTCP from 2 weeks (a) and 4 weeks (b) after implantation surgery (** $p < 0.01$).

is higher than G'' . In addition, the slope of the G' line is small and G'' displays a minimum at intermediate frequencies dependence manner as previously reported [14]. This result demonstrates that the HLA used in this study is a gel with high viscosity. This phenomenon suggests that the HLA used in this study may provide bone growth effect as mentioned

above. Although HA and β TCP granules are commonly used biomaterials for repairing bone defects, when they are dried these granules are difficult to handle in the surgical room because of low weight and lacking cohesion [26]. Incorporating these bone graft particles into a hydrogel could be a possible way to solve this problem. From the result,

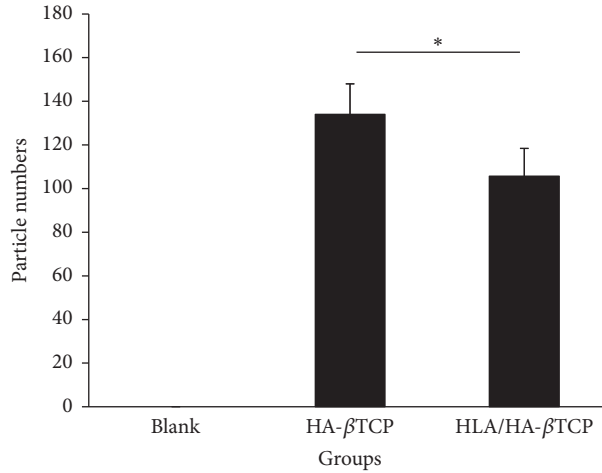


FIGURE 6: Particle numbers used in artificial defects filled with HA-βTCP alone and HLA/HA-βTCP at 2 weeks after surgery (* $P < 0.05$).

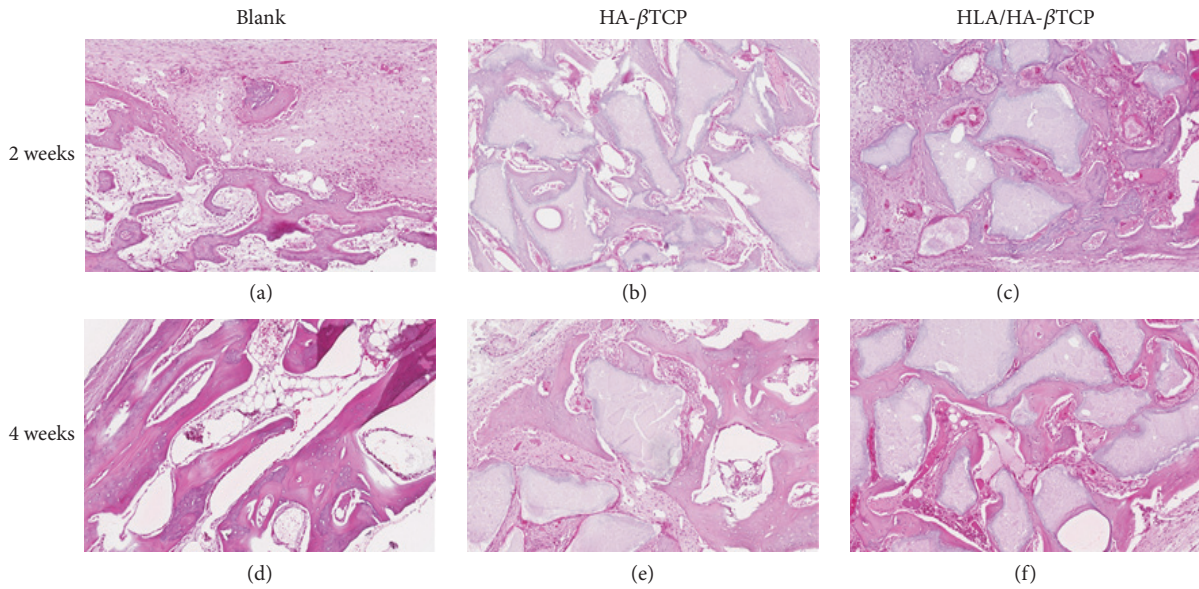


FIGURE 7: Histomorphometric images of the blank control, HA-βTCP alone, and HLA/HA-βTCP treated samples at 2 and 4 weeks.

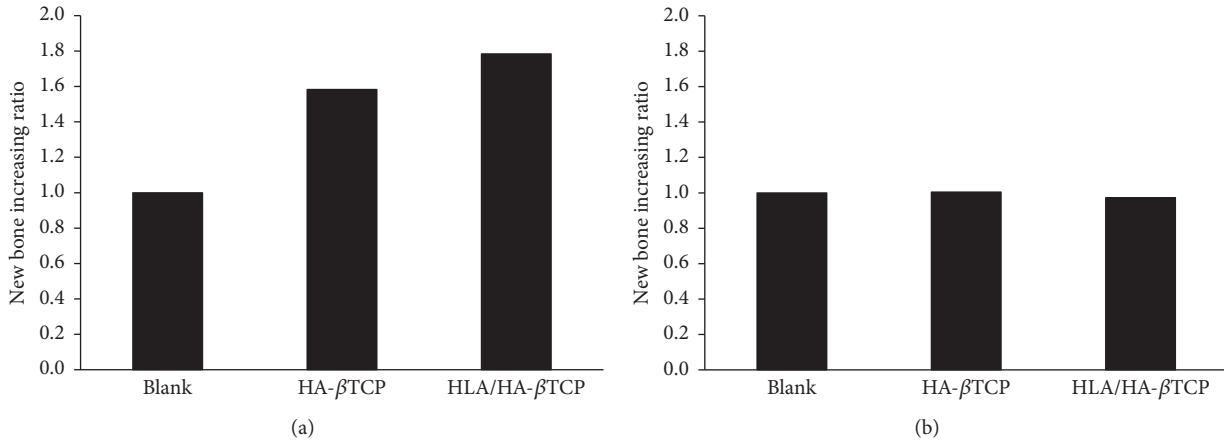


FIGURE 8: New bone increase ratio (NBIR) for the artificial defects filled with HA-βTCP alone and HLA/HA-βTCP from 2 weeks (a) and 4 weeks (b) after implantation surgery.

we concluded that incorporating HA- β TCP with HLA could be a satisfactory method for improving both regenerative efficiency and ease of handling [29–31].

5. Conclusion

In conclusion, the HLA/HA- β TCP present in this study provides bone regeneration in situations with a low amount of HA- β TCP granules. In addition, this novel material provides handling efficiency during the surgical process. Overall, HLA/HA- β TCP exhibits great promise for use in stimulating new bone formation for the treatment of sinus elevation and guided bone regeneration.

Competing Interests

The authors have declared that there is no conflict of interests.

Authors' Contributions

Yen-Lan Chang and Yi-June Lo contributed equally to this work.

Acknowledgments

This study was supported by the Ministry of Science and Technology, Taiwan (Grant MOST 104-2221-E-038-002) and in part by Wan Fang Hospital, Taipei Medical University, Taipei, Taiwan (Grant 104TMU-WFH-10).

References

- [1] R. F. Ellinger, E. B. Nery, and K. L. Lynch, "Histological assessment of periodontal osseous defects following implantation of hydroxyapatite and biphasic calcium phosphate ceramics: a case report," *The International Journal of Periodontics & Restorative Dentistry*, vol. 6, no. 3, pp. 22–33, 1986.
- [2] G. Daculsi, R. Z. LeGeros, E. Nery, K. Lynch, and B. Kerebel, "Transformation of biphasic calcium phosphate ceramics in vivo: ultrastructural and physicochemical characterization," *Journal of Biomedical Materials Research*, vol. 23, no. 8, pp. 883–894, 1989.
- [3] E. B. Nery, R. Z. LeGeros, K. L. Lynch, and K. Lee, "Tissue response to biphasic calcium phosphate ceramic with different ratios of HA/beta TCP in periodontal osseous defects," *Journal of Periodontology*, vol. 63, no. 9, pp. 729–735, 1992.
- [4] M. C. Schulz, P. Korn, B. Stadlinger et al., "Coating with artificial matrices from collagen and sulfated hyaluronan influences the osseointegration of dental implants," *Journal of Materials Science: Materials in Medicine*, vol. 25, no. 1, pp. 247–258, 2014.
- [5] P. Korn, M. C. Schulz, V. Hintze et al., "Chondroitin sulfate and sulfated hyaluronan-containing collagen coatings of titanium implants influence peri-implant bone formation in a minipig model," *Journal of Biomedical Materials Research Part A*, vol. 102, no. 7, pp. 2334–2344, 2014.
- [6] C. R. Correia, L. S. Moreira-Teixeira, L. Moroni et al., "Chitosan scaffolds containing hyaluronic acid for cartilage tissue engineering," *Tissue Engineering Part C: Methods*, vol. 17, no. 7, pp. 717–730, 2011.
- [7] P. Dahiya and R. Kamal, "Hyaluronic acid: a boon in periodontal therapy," *North American Journal of Medical Sciences*, vol. 5, no. 5, pp. 309–315, 2013.
- [8] J. Kablik, G. D. Monheit, L. Yu, G. Chang, and J. Gershkovich, "Comparative physical properties of hyaluronic acid dermal fillers," *Dermatologic Surgery*, vol. 35, supplement 1, pp. 302–312, 2009.
- [9] S.-F. Sun, Y.-J. Chou, C.-W. Hsu et al., "Efficacy of intra-articular hyaluronic acid in patients with osteoarthritis of the ankle: a prospective study," *Osteoarthritis and Cartilage*, vol. 14, no. 9, pp. 867–874, 2006.
- [10] H. Jentsch, R. Pomowski, G. Kundt, and R. Göcke, "Treatment of gingivitis with hyaluronan," *Journal of Clinical Periodontology*, vol. 30, no. 2, pp. 159–164, 2003.
- [11] T. Sasaki and C. Watanabe, "Stimulation of osteoinduction in bone wound healing by high-molecular hyaluronic acid," *Bone*, vol. 16, no. 1, pp. 9–15, 1995.
- [12] T. B. L. Nguyen and B.-T. Lee, "A combination of biphasic calcium phosphate scaffold with hyaluronic acid-gelatin hydrogel as a new tool for bone regeneration," *Tissue Engineering A*, vol. 20, no. 13–14, pp. 1993–2004, 2014.
- [13] M. R. Nejadnik, X. Yang, M. Bongio et al., "Self-healing hybrid nanocomposites consisting of bisphosphonated hyaluronan and calcium phosphate nanoparticles," *Biomaterials*, vol. 35, no. 25, pp. 6918–6929, 2014.
- [14] A. ELkarargy, "Alveolar sockets preservation using hydroxyapatite/beta tricalcium phosphate with hyaluronic acid (histomorphometric study)," *Journal of American Science*, vol. 9, no. 1, pp. 556–563, 2013.
- [15] A. A. M. Shimojo, A. M. B. Pires, L. G. De La Torre, and M. H. A. Santana, "Influence of particle size and fluid fraction on rheological and extrusion properties of crosslinked hyaluronic acid hydrogel dispersions," *Journal of Applied Polymer Science*, vol. 128, no. 3, pp. 2180–2185, 2013.
- [16] F. M. Tamimi, J. Torres, I. Tresguerres, C. Clemente, E. López-Cabarcos, and L. J. Blanco, "Bone augmentation in rabbit calvariae: comparative study between Bio-Oss® and a novel β -TCP/DCPD granulate," *Journal of Clinical Periodontology*, vol. 33, no. 12, pp. 922–928, 2006.
- [17] L. Andersson, A. Ramzi, and B. Joseph, "Studies on dentin grafts to bone defects in rabbit tibia and mandible; development of an experimental model," *Dental Traumatology*, vol. 25, no. 1, pp. 78–83, 2009.
- [18] R. Bedini, D. Meleo, R. Pecci, and L. Pacifci, "The use of microtomography in bone tissue and biomaterial three-dimensional analysis," *Annali dell'Istituto Superiore di Sanita*, vol. 45, no. 2, pp. 178–184, 2009.
- [19] N. Bakhshalian, S. Hooshmand, S. C. Campbell, J.-S. Kim, K. Brummel-Smith, and B. H. Arjmandi, "Biocompatibility and microstructural analysis of osteopromotive property of allogenic demineralized dentin matrix," *The International Journal of Oral & Maxillofacial Implants*, vol. 28, no. 6, pp. 1655–1662, 2013.
- [20] S. W. Feng, K. N. Ho, Y. H. Chan, K. Chang, W. Lai, and H. Huang, "Damping factor as a diagnostic parameter for assessment of osseointegration during the dental implant healing process: an experimental study in rabbits," *Annals of Biomedical Engineering*, vol. 44, no. 12, pp. 3668–3678, 2016.
- [21] H. I. Atilgan, K. Demirel, Y. Kankaya et al., "Scintigraphic and histopathologic evaluation of combined bone grafts," *Journal of Craniofacial Surgery*, vol. 24, no. 6, pp. 1902–1907, 2013.

- [22] M. Krause, R. Oheim, P. Catala-Lehnen et al., “Metaphyseal bone formation induced by a new injectable β -TCP-based bone substitute: a controlled study in rabbits,” *Journal of Biomaterials Applications*, vol. 28, no. 6, pp. 859–868, 2014.
- [23] S. Mathews, R. Bhonde, P. K. Gupta, and S. Totey, “Novel biomimetic tripolymer scaffolds consisting of chitosan, collagen type 1, and hyaluronic acid for bone marrow-derived human mesenchymal stem cells-based bone tissue engineering,” *Journal of Biomedical Materials Research—Part B Applied Biomaterials*, vol. 102, no. 8, pp. 1825–1834, 2014.
- [24] M. Aslan, G. Şimşek, and E. Dayi, “The effect of hyaluronic acid-supplemented bone graft in bone healing: experimental study in rabbits,” *Journal of Biomaterials Applications*, vol. 20, no. 3, pp. 209–220, 2006.
- [25] N. Karaçal, P. Koşucu, U. Cobanglu, and N. Kutlu, “Effect of human amniotic fluid on bone healing,” *The Journal of Surgical Research*, vol. 129, no. 2, pp. 283–287, 2005.
- [26] E. Aguado, F. Pascaretti-Grizon, C. Gaudin-Audrain, E. Goyenvalle, and D. Chappard, “ β -TCP granules mixed with reticulated hyaluronic acid induce an increase in bone apposition,” *Biomedical Materials*, vol. 9, no. 1, Article ID 015001, 2014.
- [27] J. Necas, L. Bartosikova, P. Brauner, and J. Kolar, “Hyaluronic acid (hyaluronan): a review,” *Veterinarni Medicina*, vol. 53, no. 8, pp. 397–411, 2008.
- [28] N. Zhao, X. Wang, L. Qin, Z. Guo, and D. Li, “Effect of molecular weight and concentration of hyaluronan on cell proliferation and osteogenic differentiation in vitro,” *Biochemical and Biophysical Research Communications*, vol. 465, no. 3, pp. 569–574, 2015.
- [29] K. Park, “Injectable hyaluronic acid hydrogel for bone augmentation,” *Journal of Controlled Release*, vol. 152, no. 2, pp. 207–208, 2011.
- [30] H. Tan, H. Li, J. P. Rubin, and K. G. Marra, “Controlled gelation and degradation rates of injectable hyaluronic acid-based hydrogels through a double crosslinking strategy,” *Journal of Tissue Engineering and Regenerative Medicine*, vol. 5, no. 10, pp. 790–797, 2011.
- [31] K. Edsman, L. I. Nord, Å. Öhrlund, H. Lärkner, and A. H. Kenne, “Gel properties of hyaluronic acid dermal fillers,” *Dermatologic Surgery*, vol. 38, no. 7, pp. 1170–1179, 2012.

Research Article

Cytotoxicity of Titanate-Calcium Complexes to MC3T3 Osteoblast-Like Cells

Yen-Wei Chen,¹ Jeanie L. Drury,¹ Joelle Moussi,¹ Kathryn M. L. Taylor-Pashow,² David T. Hobbs,² and John C. Wataha¹

¹Department of Restorative Dentistry, University of Washington School of Dentistry, Seattle, WA 98195-7456, USA

²Savannah River National Laboratory, Aiken, SC 29808, USA

Correspondence should be addressed to Yen-Wei Chen; ywchen@uw.edu

Received 6 October 2016; Revised 6 November 2016; Accepted 9 November 2016

Academic Editor: Wei-Jen Chang

Copyright © 2016 Yen-Wei Chen et al. This is an open access article distributed under the Creative Commons Attribution License, which permits unrestricted use, distribution, and reproduction in any medium, provided the original work is properly cited.

Monosodium titanates (MST) are a relatively novel form of particulate titanium dioxide that have been proposed for biological use as metal sorbents or delivery agents, most recently calcium (II). In these roles, the toxicity of the titanate or its metal complex is crucial to its biological utility. The aim of this study was to determine the cytotoxicity of MST and MST-calcium complexes with MC3T3 osteoblast-like cells; MST-Ca(II) complexes could be useful to promote bone formation in various hard tissue applications. MC3T3 cells were exposed to native MST or MST-Ca(II) complexes for 24–72 h. A CellTiter-Blue[®] assay was employed to assess the metabolic activity of the cells. The results showed that MST and MST-Ca(II) suppressed MC3T3 metabolic activity significantly in a dose-, time-, and cell-density-dependent fashion. MST-Ca(II) suppressed MC3T3 metabolism in a statistically identical manner as native MST at all concentrations. We concluded that MST and MST-Ca(II) are significantly cytotoxic to MC3T3 cells through a mechanism yet unknown; this is a potential problem to the biological utility of these complexes.

1. Introduction

Titanium-based materials have been widely explored for use in biological applications. Titanium-oxygen alloys, crystalline titanium dioxide (TiO₂, anatase), and monosodium titanates (MST) have been the three most widely employed forms of titanium-based materials. Of these, the monosodium titanate particles are the least investigated. Titanium-oxygen alloys have been successfully used for orthopedic hip replacements and dental implants because of their superior physical and biological properties. To enhance bone-bonding bioactivity, titanium alloys have been subjected to alkaline or heat treatments to form a calcium-TiO₂ layer on their surfaces [1]. The calcium is fixed to the alloy surface and therefore not labile.

Monosodium titanate (MST), one type of titanate, is an inorganic compound of titanium oxide with an amorphous core and crystalline surface that has been modified to create Ti-O-Na groups that have exchangeable sodium [2]. Both

MST and crystalline titanium dioxide (anatase) are oxides of titanium but have notable differences in their particle sizes and crystalline surfaces. The well-defined crystalline surface and surface hydroxide groups of the larger (1–20 μm) MST tend to be an ion exchanger rather than smaller (10–25 nm) anatase, which tends to behave as a surface interactor [3]. MST-Ca(II) complex may therefore have utility as a source of Ca(II) in biological systems, sequestered in place by its relatively large particle size.

MST exhibits high affinity for a variety of metal ions at high pH, including strontium ions, which has made it an attractive adsorbent for separating radioactive elements from highly alkaline wastes produced during reprocessing of nuclear fuels [4]. More recently, several groups have explored the possibility of exploiting MST-metal ion affinity in biological applications [2, 4]. Metals such as Au(I), Au(III), and Pt(II) have appeal as candidates for novel drugs because of their unique binding and redox properties [5–10]. However, the systemic toxicity of metals has historically

limited their applicability as therapeutic agents [11]. Insoluble monosodium titanate MST particles bound to multivalent metal ions such as Au(III) and Pt(II) could facilitate local delivery by sequestering, via the relatively large particle size of the titanate, metal ions at the site of delivery, thereby reducing systemic toxicity risks. A few studies have reported that titanate-metal compounds amplify antibacterial and anti-inflammatory therapeutic outcomes and reduce the risk of the systemic toxicity of metals [12–15].

Among the titanium-based materials, the biological properties of the titanates are the least studied. The toxicity of native titanates (without metal ions) is important to any use of these materials as therapeutic agents, and the toxicity of MST has been reported [4, 12]. Native MST suppresses mammalian cell metabolism to some extent in several cell types, and some metal ions complexed to MST further suppress cellular metabolism [2, 12, 13, 15]. However, from information available thus far, at lower concentrations, MST toxicity would not preclude its use to locally deliver metal ions in therapeutic applications.

In dentistry, calcium-releasing materials have been used for decades as therapeutic agents to stimulate dentinal repair and bone integration. Calcium hydroxide and mineral trioxide aggregate (MTA) are two such compounds used routinely to encourage reparative dentin formation [16, 17]. Despite proven favorable therapeutic outcomes with these materials, calcium hydroxide and MTA have limitations such as high solubility, weak mechanical properties, high costs, or prolonged setting time [18, 19]. The recent discovery that MST binds and releases Ca(II) makes possible the use of MST to locally deliver calcium ions in dental applications. Titanium alloys have been used for dental endosseous implants because of their superior biocompatibility and mechanical strength [20]. Initially, to enhance the ability of bone to bond to the titanium surface, implants were plasma-sprayed with calcium phosphate [21, 22]. However, debonding of the apatite layer and the inability of these coatings to release calcium from the titanium alloy remain problematic [1]. Subsequently, numerous techniques have been developed to incorporate calcium into titanium surfaces by thermal and chemical treatments, but the calcium in these strategies is not generally releasable [23–25]. Transforming the surface from titanium alloy into an active titanate at least theoretically provides an exchangeable source of calcium on the implant surface. Such a source could be advantageous clinically to osseointegration.

The biological effects on mammalian cells of native titanates and titanates combined with a variety of metal ions (Au(III), Hg(II), Pd(II), Pt(IV), and cisplatin) have been investigated [13]. However, the toxicity of MST-Ca(II) complexes is unknown, particularly to osteoblast-like cells that would be key players in any therapeutic application of calcium-titanate complexes. For this reason, we specifically investigated the cytotoxicity of MST and MST-Ca(II) complexes to osteoblast-like cells *in vitro*. Our goal was to determine the cytotoxicity of MST and MST-calcium complexes using MC3T3 cells, an osteoblast-like cell commonly used to screen for *in vitro* cytotoxicity. Knowing the cytotoxic profile of MST-Ca(II) is a necessary first step in any development of a calcium-releasing dental therapeutic agent.

2. Materials and Methods

2.1. MST and MST-Ca(II) Loading. MST was obtained from commercial sources (Optima Chemical Group, LLC Douglas, GA). MST was mixed with Ca(II) at a ratio of 6.61 : 1, resulting in a final MST-Ca(II) material with 77 mg of dry Ca(II) per gram of MST. MST-Ca(II) materials were prepared to maximize the loading of calcium onto the MST particulates. MST-Ca(II) was then stored in airtight conical tubes as a 29.67 wt% paste until dilution. For experiments, MST and MST-Ca(II) preparations were mixed with sterile water to obtain stock solutions (4000 mg/L) that were diluted to final concentrations (0–200 mg/L) for experiments.

2.2. MC3T3 Cell Culture. MC3T3 osteoblast-like cells (ATCC CRL-2593) were selected because they are a well-characterized osteoblastic cell line with reproducible properties in culture. These cells were cultured in alpha-MEM, supplemented with 10% of FBS, 100 units/mL of penicillin, and 100 μ g/mL of streptomycin (all reagents from Life Technologies, Grand Island, NY). Stock cultures of cells were maintained at 37°C, 5% CO₂, and 100% relative humidity.

MC3T3 cells were plated (5,000 or 30,000 cells/cm²) in 96-well format ($n = 8$, flat bottom) in 0.2 mL of culture media per well. The plated cells were incubated for 24 h to allow for adherence before addition of MST or MST-Ca(II) suspensions. MST or MST-Ca(II) complexes were diluted from the stock suspensions and added to each well (0.01 mL into 0.2 mL media) to obtain a final MST concentrations of 0, 0.5, 1, 10, 25, 50, 100, and 200 mg/L. Treated MC3T3 cell cultures were incubated for 24 or 72 h before measuring cellular mitochondrial activity. MC3T3 cells without MST or MST-Ca(II) treatment were used as controls.

2.3. Measurement of Cellular Mitochondrial Activity. Cellular mitochondrial activity was estimated using a commercially available CellTiter-Blue® reagent (CTB; Promega, Madison, WI). The CTB assay was selected specifically because our previous work established that, unlike other spectrophotometric assays that rely on optical density (transmittance), the particulate nature of the titanates did not interfere with this fluorescence-based assay [2]. The assay was completed according to the manufacturer's protocol, with an optimized incubation time of 60 min for MC3T3 cells. CTB fluorescence (FL: 560EX/590EM) was measured with a SpectraMax M2 plate reader (Molecular Devices, Sunnyvale, CA). Data were normalized to untreated controls. Statistically significant differences in metabolic activity among controls, MST, and MST-Ca(II) were identified using one-way ANOVA with Tukey *post hoc* analyses ($\alpha = 0.05$).

3. Results

3.1. Effect of Cell Plating Density and MST Exposure Time. MST suppressed MC3T3 cell metabolic activity at concentrations as low as 5 mg/L (Figure 1). Suppression was dose-dependent regardless of the cell plating density and was influenced by the length of MST exposure to the cells. At

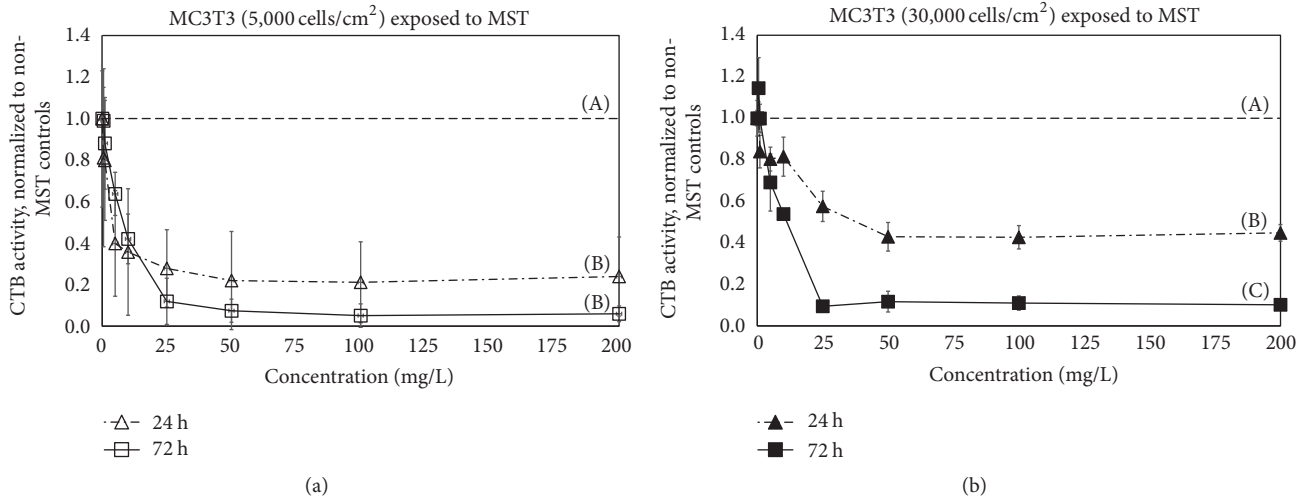


FIGURE 1: MC3T3 osteoblast metabolic activity (measured by CellTiter-Blue® (CTB)) after *in vitro* exposure to monosodium titanates (MST) at (a) 5,000 cells/cm² or (b) 30,000 cells/cm² for 24 or 72 h. Metabolic activity was normalized to controls without MST (denoted by horizontal dashed line). Lower cell plating densities and increased time of exposure led to depressed cell activity. Uppercase letters (A, B, and C) indicate statistical differences (Tukey pairwise comparisons, $\alpha = 0.05$, and $n = 8$).

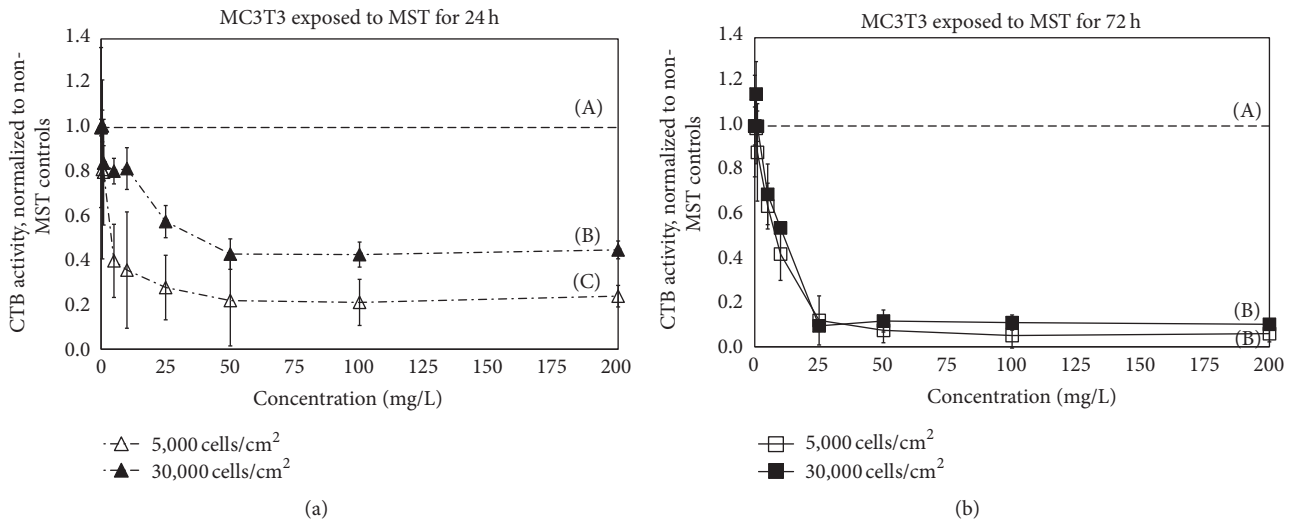


FIGURE 2: MC3T3 osteoblast metabolic activity (measured by CellTiter-Blue® (CTB)) after *in vitro* exposure to monosodium titanates (MST) for (a) 24 h or (b) 72 h with a 5,000 or 30,000 cells/cm² plating density. Metabolic activity was normalized to controls without MST (denoted by horizontal dashed line). Uppercase letters (A, B, and C) indicate statistical differences (Tukey pairwise comparisons, $\alpha = 0.05$, and $n = 8$).

5000 cell/cm² (Figure 1(a)), MST-treated cultures reached a plateau of 78% suppression (over untreated controls) after 24 h (50 mg/L). This suppression was statistically significant at doses as low as 5 mg/L ($p < 0.05$, $n = 8$). After 72 h of exposure to MST, MC3T3 cell metabolism dropped even more, 93% relative to controls at 50 mg/L of MST ($p < 0.05$, $n = 8$) and 15% more than suppression at 24 h (Figure 1(a)).

At 30,000 cell/cm² (Figure 1(b)), MST-treated cultures reached a suppression plateau of 57% (versus untreated controls) after 24 h (50 mg/L). After 72 h, the metabolic activity of MC3T3 cells was further and significantly suppressed by MST

reaching a plateau of 88% suppression at 50 mg/L ($p < 0.05$, $n = 8$). Thus, the cytotoxic effects of the titanates were less pronounced at the higher plating density.

Time of MST exposure also played a role in how MC3T3 osteoblasts responded to MST (Figures 2(a) and 2(b)). After 24 h (Figure 2(a)) MC3T3 metabolic activity was dependent on cell plating density, but after 72 h (Figure 2(b)) cells were largely independent of initial cell plating density. After 24 h exposure, MST suppressed MC3T3 metabolism 76% at 5000 cell/cm² compared to 56% suppression at 30,000 cell/cm² (Figure 2(a)). This difference was statistically

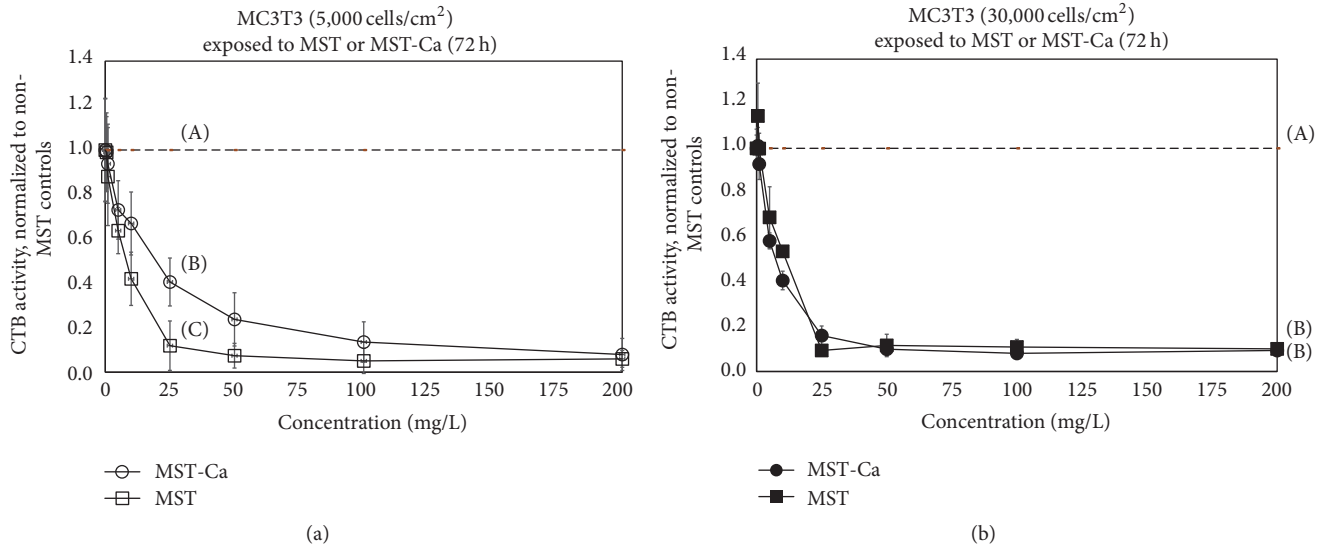


FIGURE 3: MC3T3 osteoblast metabolic activity (measured by CellTiter-Blue® (CTB)) after *in vitro* exposure to monosodium titanate-calcium compounds (MST-Ca(II)) with (a) 5,000 or (b) 30,000 cells/cm² plating density after 72 h exposures. Metabolic activity was normalized to controls without MST (denoted by horizontal dashed line). Uppercase letters (A, B, and C) indicate statistically different results (Tukey pairwise comparisons, $\alpha = 0.05$, and $n = 8$).

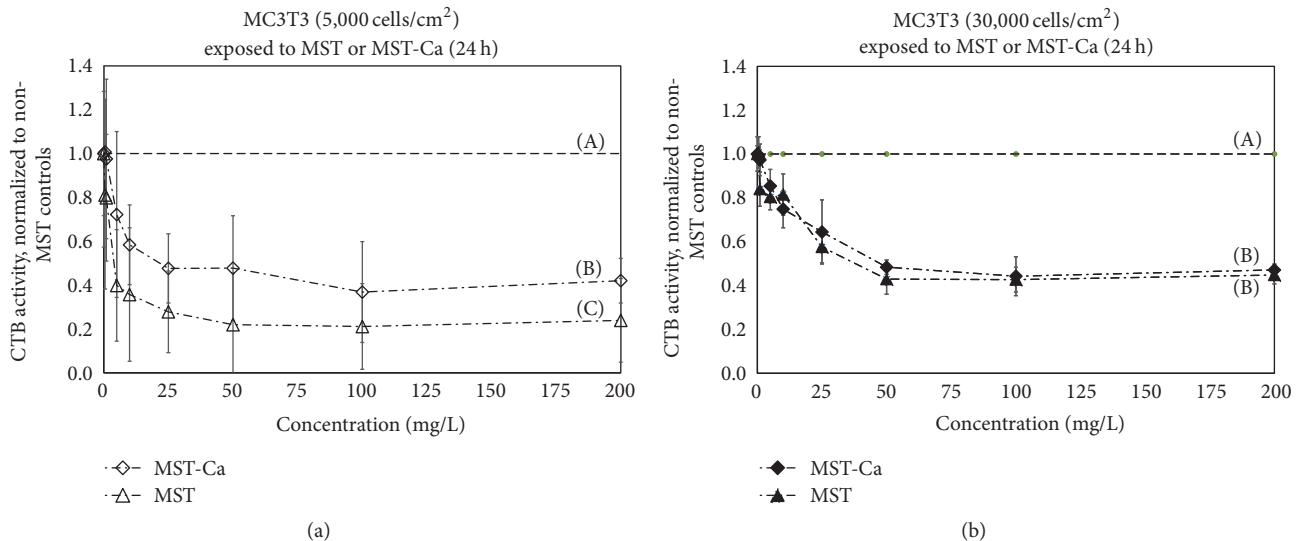


FIGURE 4: MC3T3 osteoblast metabolic activity (measured by CellTiter-Blue® (CTB)) after *in vitro* exposure to monosodium titanate-calcium compounds (MST-Ca(II)) with (a) 5,000 or (b) 30,000 cells/cm² plating density after 24 h exposures. Metabolic activity was normalized to controls without MST (denoted by horizontal dashed line). Uppercase letters (A and B) indicate statistically different results (Tukey pairwise comparisons, $\alpha = 0.05$, and $n = 8$).

significant ($p < 0.05$, $n = 8$). When the MST exposure period was extended to 72 h (Figure 2(b)), MST suppressed MC3T3 metabolism ~90% regardless of initial cell density.

3.2. Effect of MST-Ca(II) Compounds. Complexing Ca(II) with MST significantly mitigated native MST suppression of MC3T3 cell metabolic activity at low cell seeding densities ($p < 0.05$, $n = 8$). At 5000 cell/cm² and 72 h incubation (Figure 3(a)), MST-Ca(II) suppressed MC3T3 metabolism nearly 20% less than MST alone. Mitigation of suppression was

observed for an intermediate range of titanate concentrations, with no differences between MST and MST-Ca(II) at concentrations below 5 mg/L or greater than 100 mg/L. Results were even more pronounced at 24 h exposure (Figure 4(a)). At 5000 cell/cm² and 24 h incubation, the addition of Ca(II) to MST reduced suppression of MC3T3 cell metabolism by nearly 50% across all concentrations ($p < 0.05$, $n = 8$).

At 30,000 cells/cm², the addition of Ca(II) to the MST did not alter the overall suppression of MC3T3 metabolic activity versus native MST at any concentration (Figure 3(b)).

In this case, both MST and MST-Ca(II) suppressed MC3T3 metabolic activity by ~90%. Similar results were observed at 5000 cell/cm² and 24 h incubation (Figure 4(b)), except that suppression was approximately 50% versus untreated controls.

4. Discussion

Titanate-metal complexes have been reported to enhance delivery of metal ions to mammalian cells and suppress mammalian cell metabolism to different extents in different cell types [4, 12, 15]. Yet, the cytotoxic profile of native (uncomplexed) titanates is only partly defined. In particular, the potential toxicological effects of titanates and titanate-calcium complexes to MC3T3 cells, a preosteoblastic cell, are underexplored. The osteoblastic cell response is central to the success of many biomedical devices that are implanted into bone or exist juxtaposed to bone or other mineralized tissue such as dentin. Previous studies have reported that calcium ions can be complexed with MST and that calcium ions are released from MST-Ca(II) complexes over time. These reports have led us to propose that MST-Ca(II) complexes may be optimized to enhance Ca(II) release and mineralization of juxtaposed bone or dental pulpal tissues. The first step in testing this hypothesis was to assess the cytotoxicity of MST-Ca(II) complexes, which we have reported in the current study.

Previous studies reported that native MST exhibited relatively low toxicity to mammalian monocytic cells (THP1) and murine L929 fibroblasts [4, 12, 13]. In contrast, others reported that native MST significantly suppressed the mitochondrial activity of rapidly dividing oral squamous-cell carcinoma cells (OSC2) [15]. The OSC2 report hypothesized that native titanates caused greater cytotoxicity to rapidly dividing OSC2 cells than more slowly dividing human THP1 monocytes and murine L929 fibroblasts. Collectively these studies suggested a positive correlation between short population doubling times (PDT) and cytotoxicity [2]. In the current study, native MST suppressed the mitochondrial activity of MC3T3 cells, despite their long PDT (38 h) relative to OSC2 cells (12–15 h) [26]. Suppression was observed in a dose-dependent fashion at both low and high cell seeding densities (Figures 1 and 2). These findings coincide with a previous study which indicated that the cytotoxicity of MST was not restrained to rapidly growing cells but also to slower growing WI-38 fibroblast cells [2]. Based on the current results, PDT does not appear to be an important factor in predicting MST toxicity. It seems reasonable to hypothesize that native titanates have quite different toxicological profiles to different types of mammalian cells. The reasons for these different cellular reactions are not known but may involve the assays used for measuring the cytotoxic effects, the affinity of the titanates for a particular cell type, or the ability of the particles to gain access to the cells once attached.

Initial assays for measuring the effects of MST or MST-metal ion complexes relied on optical density (OD) measurements, particularly the MTT assay [12, 13]. Optical density interference in the MTT assay has been demonstrated due

to the particulate nature of titanates, even with attempts to remove particles with centrifugation [2, 3]. The interfering nature of the titanate particulates may underestimate the effects of titanates on cells because the OD results from particulate interference rather than true spectrophotometric absorption. Cell Titer-Blue®, the fluorescence-based assay, was used at this study because previous reports showed that the measurement of mitochondrial function was unaffected by MST particulates. Finally, we note that, in terms of overall assay sensitivity, we have observed no substantial difference between the two methods. Our current results therefore support the utility of this assay for the MST system; the near zero OD of some time points could not have been observed if particulate interference was present (e.g., Figure 2(b)).

Although we cannot provide quantifiable measures, we observed that the MST particles (which refract light substantially in phase contrast view) were always associated with the MC3T3 cells and that washing the cell layer did not remove these particles. Although speculative at this point, the profound suppression of MC3T3 cell metabolism by MST suggests that MST might have better adherence to MC3T3 cells than other cells previously studied. The small size of MST (5–10 μm) particles could make it more accessible to the relatively large MC3T3 cell [4, 27]. The increased contact of the particle-cell interface might intensify the cytotoxic effects of the MST on MC3T3 metabolic activity; this is clearly a direction for further investigation.

The physical disruption of cellular attachment to cell-culture plates could be another mechanism causing high MST cytotoxicity to MC3T3 cells. MST is a heavy particle which settles easily on the bottom of culture wells and has seemingly tenacious adhesion to cell-culture plates. A high density of MST particles occupying sites of adhesion on a cell-culture plate might “compete” for the adherent sites required by the MC3T3 cells for survival or proliferation. In particular, MST-plate attachment might prevent cells from reattaching to the plate postmitosis [2]. Adhesion of particles affecting cell attachment is not without precedent; it has been reported that titanium dioxide particles can disturb fibronectin-mediated adhesion of preosteoblasts [28, 29]. Furthermore, the MST inhibiting effect was more pronounced at the lower initial cell plating density, where the titanates would have had the most access to the plate surface (e.g., Figure 1(a)). Such an effect was not reported with THP1 monocytes, which do not require adhesion for survival and proliferation (anchorage independent) [4, 12]. Future studies should help reach a more complete understanding of the mechanism of titanate cytotoxicity to different mammalian cell types.

In the current study, complexing Ca(II) with MST mitigated MST suppression of MC3T3 mitochondrial activity at low cell seeding densities (Figures 3 and 4). This finding was unexpected and suggested that Ca(II) may interfere with the binding of MST to the MC3T3 cells in some manner. Other studies have reported that MST-Ca(II) complexes release Ca(II) over time. The released calcium ions might interfere with the binding capacity of MST by occupying a limited number of the sites able to attach to cells and trigger toxicity. At high seeding densities, the mitigating effect was not observed and would not have been expected because

the effect of the Ca(II) would have been less critical with a more favorable cell-to-titanate ratio. Further experiments will be needed to investigate the affinity of the receptors of the native titanates and the metal-titanates complexes to different mammalian cells.

5. Conclusion

The current results show that MST suppressed MC3T3 cell metabolic activity in dose-dependent fashion regardless of the initial cell density. The difference in suppression of MC3T3 cell metabolic activity between different seeding densities was less significant with a longer incubation time. MST-Ca(II) mitigated the suppression of MC3T3 cell metabolic activity at low cell seeding densities and intermediate MST concentrations but not at the high cell seeding densities. In general, MST and MST-Ca(II) are significantly cytotoxic to MC3T3 cells through a mechanism yet unknown.

Competing Interests

The authors declare that there is no conflict of interests regarding the publication of this paper.

Acknowledgments

The authors thank the following for support of this research: Department of Restorative Dentistry at the University of Washington (Spencer fund to John C. Wataha) and the United States Department of Energy (Grant no. AC717130 to David T. Hobbs with subcontract to John C. Wataha).

References

- [1] T. Kizuki, H. Takadama, T. Matsushita, T. Nakamura, and T. Kokubo, "Preparation of bioactive Ti metal surface enriched with calcium ions by chemical treatment," *Acta Biomaterialia*, vol. 6, no. 7, pp. 2836–2842, 2010.
- [2] J. L. Drury, Y. Jang, K. M. L. Taylor-Pashow, M. Elvington, D. T. Hobbs, and J. C. Wataha, "In vitro biological response of micro- and nano-sized monosodium titanates and titanate-metal compounds," *Journal of Biomedical Materials Research Part B: Applied Biomaterials*, vol. 103, no. 2, pp. 254–260, 2015.
- [3] A. G. Thomas and K. L. Syres, "Adsorption of organic molecules on rutile TiO₂ and anatase TiO₂ single crystal surfaces," *Chemical Society Reviews*, vol. 41, no. 11, pp. 4207–4217, 2012.
- [4] D. T. Hobbs, R. L. W. Messer, J. B. Lewis, D. R. Click, P. E. Lockwood, and J. C. Wataha, "Adsorption of biomaterials to monosodium titanate in biological environments," *Journal of Biomedical Materials Research Part B: Applied Biomaterials*, vol. 78, no. 2, pp. 296–301, 2006.
- [5] T. W. Hambley, "Developing new metal-based therapeutics: challenges and opportunities," *Dalton Transactions*, vol. 43, pp. 4929–4937, 2007.
- [6] P. C. Brujininx and P. J. Sadler, "New trends for metal complexes with anticancer activity," *Current Opinion in Chemical Biology*, vol. 12, no. 2, pp. 197–206, 2008.
- [7] W. F. Kean and I. R. L. Kean, "Clinical pharmacology of gold," *Inflammopharmacology*, vol. 16, no. 3, pp. 112–125, 2008.
- [8] J. A. Lemire, J. J. Harrison, and R. J. Turner, "Antimicrobial activity of metals: mechanisms, molecular targets and applications," *Nature Reviews Microbiology*, vol. 11, no. 6, pp. 371–384, 2013.
- [9] R. J. McQuitty, "Metal-based drugs," *Science Progress*, vol. 97, no. 1, pp. 1–19, 2014.
- [10] J. Sengupta, S. Ghosh, P. Datta, A. Gomes, and A. Gomes, "Physiologically important metal nanoparticles and their toxicity," *Journal of Nanoscience and Nanotechnology*, vol. 14, no. 1, pp. 990–1006, 2014.
- [11] R. A. Goyer, "Toxic effects of metals," *Toxicology*, vol. 3, pp. 582–635, 1986.
- [12] R. R. Davis, P. E. Lockwood, D. T. Hobbs et al., "In vitro biological effects of sodium titanate materials," *Journal of Biomedical Materials Research—Part B Applied Biomaterials*, vol. 83, no. 2, pp. 505–511, 2007.
- [13] R. R. Davis, D. T. Hobbs, R. Khashaba et al., "Titanate particles as agents to deliver gold compounds to fibroblasts and monocytes," *Journal of Biomedical Materials Research Part A*, vol. 93, no. 3, pp. 864–869, 2010.
- [14] W. O. Chung, J. C. Wataha, D. T. Hobbs et al., "Peroxititanate- and monosodium metal-titanate compounds as inhibitors of bacterial growth," *Journal of Biomedical Materials Research Part A*, vol. 97, no. 3, pp. 348–354, 2011.
- [15] J. L. Drury, Y.-W. Chen, J. J. Wong et al., "Titanates deliver metal compounds to suppress cell metabolism," *Journal of Experimental and Clinical Medicine*, vol. 6, no. 1, pp. 21–27, 2014.
- [16] M. Torabinejad, C. U. Hong, F. McDonald, and T. R. Pitt Ford, "Physical and chemical properties of a new root-end filling material," *Journal of Endodontics*, vol. 21, no. 7, pp. 349–353, 1995.
- [17] D. Tziafas, O. Pantelidou, A. Alvanou, G. Belibasakis, and S. Papadimitriou, "The dentinogenic effect of mineral trioxide aggregate (MTA) in short-term capping experiments," *International Endodontic Journal*, vol. 35, no. 3, pp. 245–254, 2002.
- [18] Š. Hatibović-Kofman, L. Raimundo, L. Zheng, L. Chong, M. Friedman, and J. O. Andreasen, "Fracture resistance and histological findings of immature teeth treated with mineral trioxide aggregate," *Dental Traumatology*, vol. 24, no. 3, pp. 272–276, 2008.
- [19] L. K. Bakland and J. O. Andreasen, "Will mineral trioxide aggregate replace calcium hydroxide in treating pulpal and periodontal healing complications subsequent to dental trauma? A review," *Dental Traumatology*, vol. 28, no. 1, pp. 25–32, 2012.
- [20] B. E. Pjetursson, M. Zwahlen, and N. P. Lang, "Quality of reporting of clinical studies to assess and compare performance of implant-supported restorations," *Journal of Clinical Periodontology*, vol. 39, no. 12, pp. 139–159, 2012.
- [21] I. Baltag, K. Watanabe, H. Kusakari et al., "Long-term changes of hydroxyapatite-coated dental implants," *Journal of Biomedical Materials Research*, vol. 53, no. 1, pp. 76–85, 2000.
- [22] T. T. Hägi, L. Enggist, D. Michel, S. J. Ferguson, Y. Liu, and E. B. Hunziker, "Mechanical insertion properties of calcium-phosphate implant coatings," *Clinical Oral Implants Research*, vol. 21, no. 11, pp. 1214–1222, 2010.
- [23] V. Fröjd, V. Franke-Stenport, L. Meirelles, and A. Wennerberg, "Increased bone contact to a calcium-incorporated oxidized commercially pure titanium implant: an in-vivo study in rabbits," *The International Journal of Oral and Maxillofacial Surgery*, vol. 37, no. 6, pp. 561–566, 2008.
- [24] Y.-T. Sul, B.-S. Kang, C. Johansson, H.-S. Um, C.-J. Park, and T. Albrektsson, "The roles of surface chemistry and topography in

- the strength and rate of osseointegration of titanium implants in bone,” *Journal of Biomedical Materials Research—Part A*, vol. 89, no. 4, pp. 942–950, 2009.
- [25] B.-S. Kang, Y.-T. Sul, C. B. Johansson, S.-J. Oh, H.-J. Lee, and T. Albrektsson, “The effect of calcium ion concentration on the bone response to oxidized titanium implants,” *Clinical Oral Implants Research*, vol. 23, no. 6, pp. 690–697, 2012.
- [26] I. Prasertsung, S. Kanokpanont, R. Mongkolnavin, C. S. Wong, J. Panpranot, and S. Damrongsakkul, “Comparison of the behavior of fibroblast and bone marrow-derived mesenchymal stem cell on nitrogen plasma-treated gelatin films,” *Materials Science and Engineering: C*, vol. 33, no. 7, pp. 4475–4479, 2013.
- [27] Y. Li, Q. Hu, G. Miao et al., “Size-dependent mechanism of intracellular localization and cytotoxicity of mono-disperse spherical mesoporous nano- and micron-bioactive glass particles,” *Journal of Biomedical Nanotechnology*, vol. 12, no. 5, pp. 863–877, 2016.
- [28] M.-C. Bernier, M. Besse, M. Vayssade, S. Morandat, and K. El Kirat, “Titanium dioxide nanoparticles disturb the fibronectin-mediated adhesion and spreading of pre-osteoblastic cells,” *Langmuir*, vol. 28, no. 38, pp. 13660–13667, 2012.
- [29] Y. Zhang, W. Yu, X. Jiang, K. Lv, S. Sun, and F. Zhang, “Analysis of the cytotoxicity of differentially sized titanium dioxide nanoparticles in murine MC3T3-E1 preosteoblasts,” *Journal of Materials Science: Materials in Medicine*, vol. 22, no. 8, pp. 1933–1945, 2011.